UNIVERSITY OF JYVÄSKYLÄ

MASTER'S THESIS
DEPARTMENT OF PHYSICS

Design and characterization of a plastic scintillation detector system for Beta tagging

by

Xin Li

December 2019

Author: Xin Li

Supervisors: Dr. Jan Sarén

Dr. Panu Ruotsalainen

Evaluators: Dr. Panu Ruotsalainen

Dr. Mikael Reponen

Preface

First of all, I would like to thank Professor Rauno Julin for introducing me to the Nuclear Spectroscopy Group to pursue my MSc thesis, and for his great inspirations and guidance with a professor's broad-mindedness and wisdom, which has toughly sustained my journey of self-worth fulfillment.

I have been sincerely grateful to Professor Paul Greenlees for offering me this precious opportunity to experience the challenge and achievements in this project, through which not only my mind has been brought to a new dimension, also my personality has got refined. This will benefit my life all the way ahead.

I would like to thank my supervisors, Dr. Jan Sarén and Dr. Panu Ruotsalainen, for their great efforts devoted to this project, and for bringing me into the world of experimental physics full of wonders, with their academic excellence.

I have to say to Dr. Juha Uusitalo that, the composition of this thesis cannot be completed without his lightening instructions. I would like to thank him for his excellence both as an experimentalist and as an education expert.

The birth of this project took place when Mr. Einari Periäinen machined the plastics into the desired scintillator shapes with his expertise in the Mechanical Workshop. In this sense, he is the Godfather of this project.

I must say "Kiitos paljon!" to my friend, Raimo Saunanen for his reception for me to the Carpentry workshop Uusiotuote, whenever wood is the only key to me to open a door. Every companion at Uusiotuote deserves a warm embrace.

Every soul at the Department of Physics has more or less been a comrade-like companion to me and will maintain a distinct picture in my memory wherever I am.

To my wife Yao Zhang, neither of us ever verbalized, being a companion and taking care of each other could make seemingly impossible things not that impossible. Thank you for being good companion and taking care of my daily life all-around, and for pulling me back from logical diviations from time to time with your profoundness. Without your contribution, the first draft of this thesis could not be completed within three months.

Xin Li
Jyväskylä, 2019

Abstract

Xin Li
Design and characterization of a plastic scintillation detector system for Beta tagging
MSc. Thesis
Department of Physics, University of Jyväskylä, 2019, 152 pages.

The aim of this work is to test the detection performance of the PVT-based plastic scintillation detector system for detection of β particles in future recoil-β tagging studies at JYFL. Characterization of the detector was performed with α, β, and γ radiations using silicon photomultiplier as the photodetector of the scintillation light. Characteristics of the detector were analysed using a data acquisition system and an analysis programme. The detection efficiency was extracted from the measured geometrical, absolute, and intrinsic efficiencies. Effect of external reflector was tested to give the light collection an enhancement by a factor of ~ 3. With a thin layer of ZnS(Ag) covering the frontal face of the scintillator, pulse shape discrimination properties were studied. Signals produced by α particles and γ rays were efficiently separated by means of the slow scintillation property of ZnS(Ag) in response to hadrons and α particles. The timing properties in slow and fast signal reconstructions were extracted by analysis of the pulse shapes. In order to stop β particles having energies up to 10MeV within the scintillator, the scintillator array was planned to have eight frontal pieces with dimensions of 128×6×10 mm^3 in horizontal direction and thirteen pieces with dimensions of 48×24×10 mm^3, in vertical direction. The aim is to replace the planar Ge detector used previously in correlation techniques with the position sensitive DSSD. This will improve the overall detection efficiency of β particles and γ rays at the MARA focal plane. A simulation of the correlation techniques used in recoil-beta tagging was carried out by using cosmic muons. Coincidence events were effectively identified with the relation between electron range and energy deposited in the scintillator. A research training report was included in Chapter 6 of this thesis.

A systematic attempt was made aiming at exploring a method for evaluation and optimization of the photon detection efficiency associated with light guide geometry. The angular response of the SiPM to incident light was examined with my design of an optical pulse generator. A series of optical analyses was performed to extract the angular distribution of the light output emerging from different types of light guide geometries. Based on these experimental and analytical results, a mathematical formalism was developed as a practical method for evaluation and optimization of photon detection efficiency in applications of light guide coupled to a photodetector more than qualitatively.

Keywords: Scintillator, SiPM, energy spectrum, pulse shape discrimination, timing property, efficiency, relative PDE, optimization.

Contents

1. Introduction

Applications of scintillation materials that produce a flash of luminescence light termed *scintillation* when struck by an incident charged particle or ionizing radiation, in radiation detection and measurements, have shown remarkable importance in nuclear and particle physics over a century. Perhaps the earliest application of a scintillator for particle detection was the device invented in 1903 by Sir William Crooks, known as a *spinthariscope*. As illustrated in Figure 1, the device employed a ZnS screen as a scintillator producing weak scintillation light when struck by α particles. The light was then visually discerned by a microscope in a darkened room with naked eyes, by means of the slow scintillation property of ZnS [1].

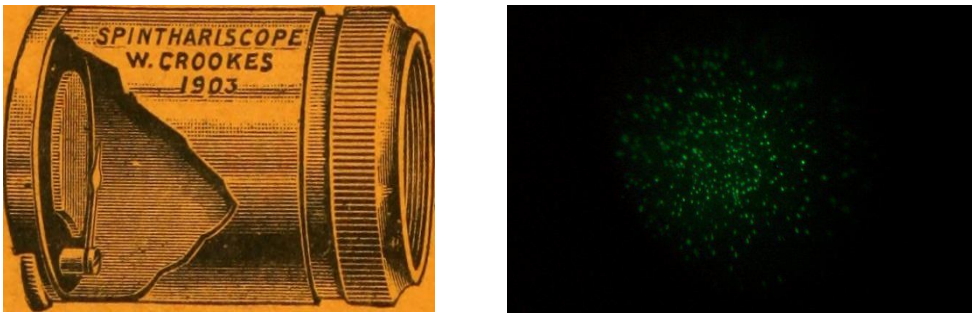

Figure 1.1: Spinthariscope and its observation of α particle induced scintillation on the ZnS screen [2].

However, due to the monotonous use, scintillators have not been popularly used in particle detection until the new detection system utilizing a photomultiplier tube (PMT) was developed by Curran and Baker in 1944. This innovation realized efficient counting of the scintillations and was followed by rapid developments and improvements until the mid-1950's. As being one of the most efficient and reliable detection techniques, the modern electronic scintillation detectors are efficient in converting scintillation lights generated by radiation into electrical pulses for analysis. Nowadays scintillation detectors designed with specific properties according to various purposes have shown a number of successful applications in nuclear and particle physics, especially in the selective study of high-/low-energy processes. For example, in the development of Recoil-Beta Tagging (RBT) methodology, a setup

called *Phoswich detector* was designed for high-energy β particle selection, as illustrated in Figure 2.

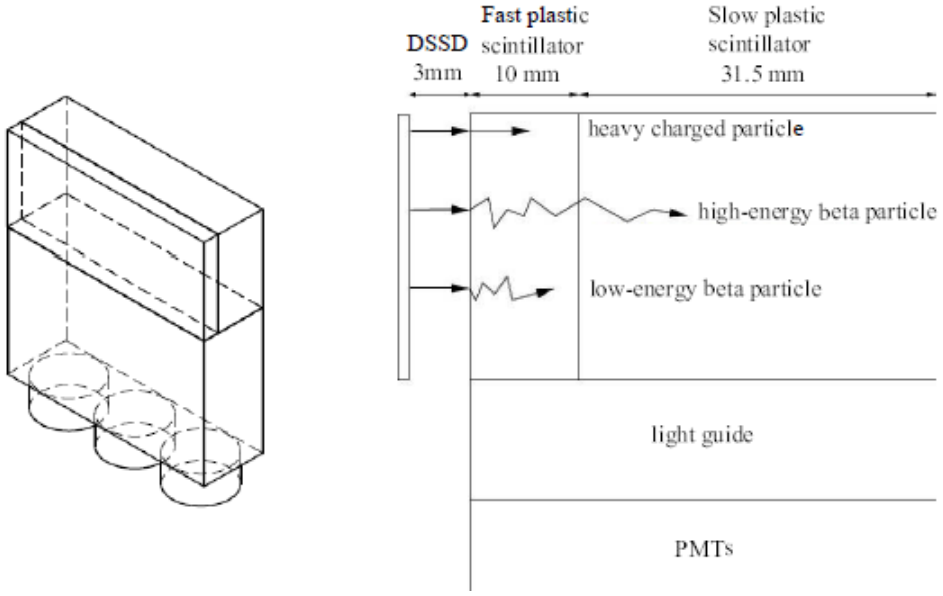

Figure 1.2: A schematic of the Phoswich detector and its responses with different types of ionizing radiation [3].

In the setup shown in Figure 1.2, a 10 mm fast-response plastic scintillator and a 31.5 mm slow-response plastic scintillator behind it were coupled to a lightguide, which collects the scintillation light to be detected by the PMTs. Heavy charged particles and low-energy β particles are stopped inside the fast scintillator while high-energy β particles are stopped within the slow scintillator after travelling through the fast scintillator. This enables identification of the interaction depth inside the detector via analysis of pulse shapes.

1.1 Background

The Mass Analysing Recoil Apparatus (MARA) was constructed at the JYFL accelerator laboratory and has been successful in studies of the exotic nuclei, for example, around the proton drip line and around the N~Z region. Certain nuclei of interests can be studied utilizing their superallowed Fermi β decay properties which give rise to high β-decay endpoint energies and short half-lives.

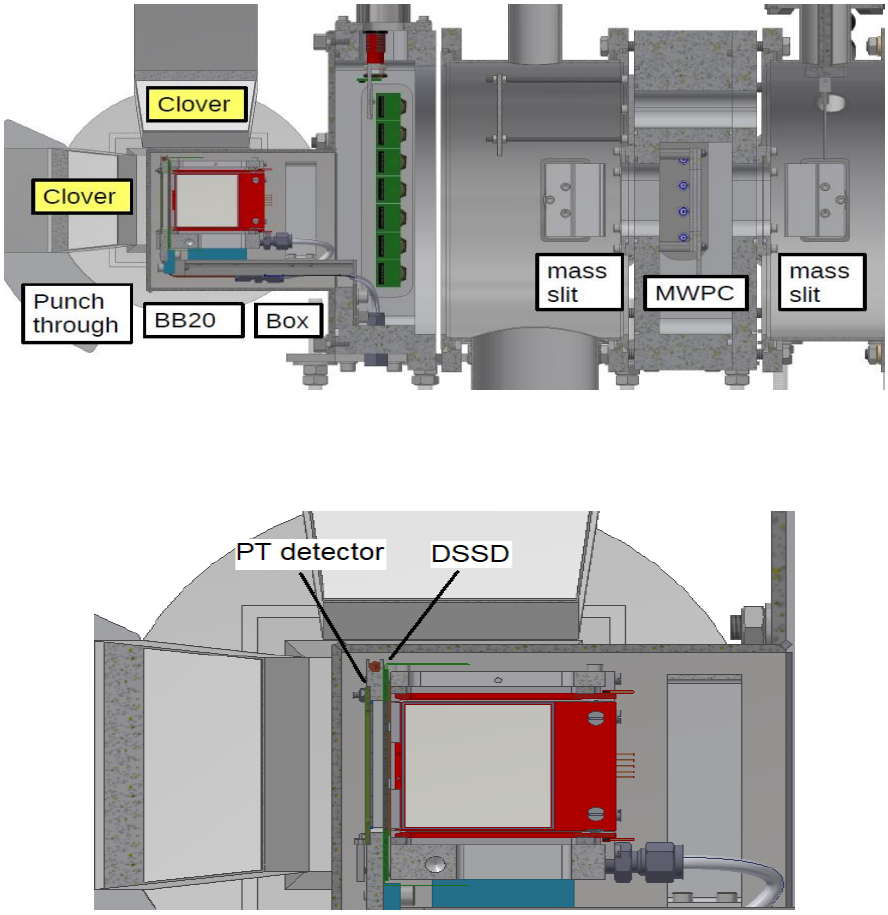

Figure 1.3: An illustration of the MARA focal plane detector setup.

As can be seen from Figure 1.3, MARA focal plane consists of Multi-Wire-Proportional-Counter (MWPC), a Double-Sided Silicon Detector (DSSD), a punch through detector (PT), planar Ge-detector, which are all housed within the focal plane vacuum chamber. Outside the vacuum chamber there is an array of Clover Ge detectors. Behind the DSSD there are two adjacent silicon detectors for punch through events detection. In addition, there is a silicon detector array in box configuration surrounding the DSSD for detection of escaping charged particles [4]. The Planar Ge detector, which has been used in recoil-beta tagging studies, requires usage of a large volume MARA focal plane vacuum chamber end cap. This increases the distance between the Ge detectors (located outside of the vacuum chamber) and DSSD causing reduction in geometrical γ ray detection efficiency. In addition, the Planar Ge detector attenuates low-energy γ rays more significantly than a plastic scintillator.

However, MARA focal plane was built with highly modifiable design allowing necessary upgrading, for example, in our case, by replacement of the planar Ge-detector with scintillator of low Z_{eff} plastic material [3] [5].

1.2 Motivation and objectives

In order to improve the overall detection efficiency of both β particles and γ rays in future recoil-beta tagging studies, we have planned to replace the planar Ge detector and PT at the MARA focal plane with an array of plastic scintillators read out by silicon photomultiplier (SiPM). The advantages of the SiPM in comparison to the traditional PMT are that, the typical range of HV required to operate a SiPM is considerably lower than that required by a traditional PMT, with considerably lower power consumption [6]. For SensL sensors, the bias voltage (V_{bia}) is typically designed < 30V, in contrast to some SiPM sensors which require a V_{bia} from 50V up to around 100V. A low-V_{bia} SiPM has the benefit that complies to the extra low voltage directive [6]. The pulse shape of a SiPM is not affected by external magnetic field, in contrast to PMTs. Besides these advantages, SiPMs still have drawbacks like optical crosstalk and after pulsing leading to excess noise. However, these limiting factors can be eliminated by electronic circuit modification with bias filters [7].

The major benefits of this plan are that, the γ detection efficiency would be practically improved by using scintillators, which will be treated by coatings of reflecting material, so that light collection would be greatly enhanced. In addition, the geometrical efficiency for β particle detection will be improved by this new design. Financially, the plastic scintillator is inexpensive in comparison to the Ge-detector.

In this thesis work, the EJ-248 plastic scintillator produced by Eljen Technology was fabricated to three different sizes, 10 x 10 mm^2, 10 x 20 mm^2, and 10 x 30 mm^2. Each scintillator was designed with 45^o and 60^o rectangular frustum-shaped lightguides on the opposite ends respectively, so that scintillation light from the scintillators would be collected to the 6 x 6 mm^2 active area of the

SiPMs. The objective of this project is to test these detector setups for the detection performance in presence of different types of ionizing radiation by analysing the light readout, signal characteristics, and energy spectra measured with the data acquisition and analysis system. By these, necessary characterization information can be obtained for the design of the geometry and optimization of the performance of the future detector.

2. Basics of radioactive decay

Radiation resulting from atomic or nuclear processes fall into four general categories:

- Charged-particle radiation $\begin{cases} Fast\ electrons \\ Heavy\ charged\ particles \end{cases}$

- Uncharged radiation $\begin{cases} Electromagnetic\ radiation \\ Neutrons \end{cases}$

Fast electrons include electrons and positrons emitted in radioactive β decay and energetic electrons emitted in internal conversion process. A heavy charged particle is defined to have a nucleon number $A \geqslant 1$, such as protons, α particles, etc. The electromagnetic radiation covers X-rays and γ -rays. Neutrons generated in various processes are divided into fast neuron and slow neutron categories [8]. Charged particles carrying sufficient amount of energy (usually at speed greater than 1% of the speed of light), and electromagnetic waves falling into the high-energy end of the electromagnetic spectrum tend to detach electrons from atoms or molecules when incident on typical materials, and hence cause ionization of the materials.

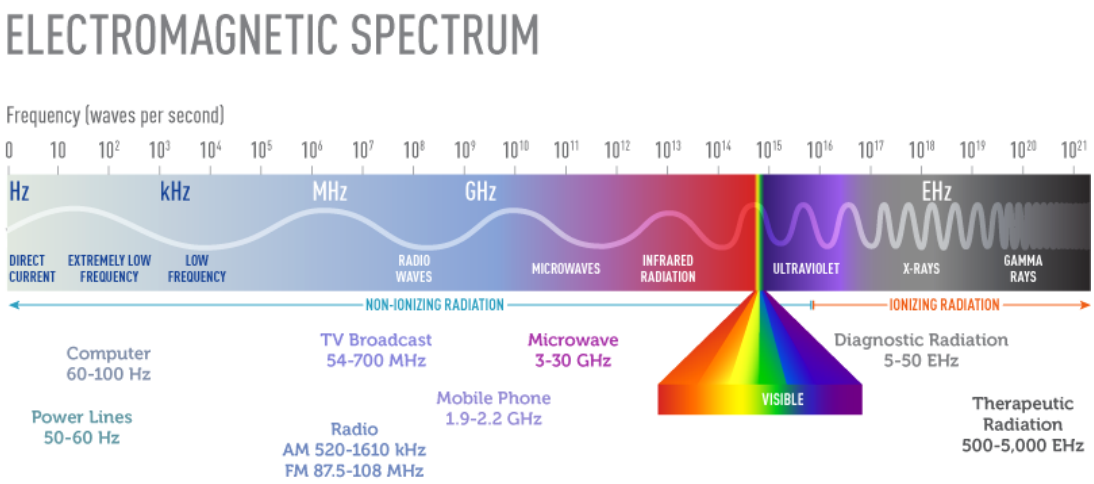

Figure 2.1: Classification of ionizing and non-ionizing electromagnetic radiation in the electromagnetic spectrum [9].

As illustrated in Figure 2.1, the boundary between ionizing and non-ionizing electromagnetic radiation lying in the ultraviolet regime is not clearly defined since the ionization energy varies amongst different atoms and molecules. The boundary is conventionally defined at a photon energy between 10 eV and 33 eV [10]. In our project the ionizing radiation was produced by radioactive decays of certain radioisotopes. Almost all radioactive decay products are ionizing since their energies are typically far greater than that required for ionization [11]. The decay processes involved in the measurements of this work are α decay, β decay, γ decay and internal conversion.

2.1 Radioactivity

Radioactive decay is defined as the process by which an unstable atomic nucleus spontaneously disintegrates to a different nucleus or to a lower energy state of the decaying nucleus with the emission of radiation. According to the quantum theory, radioactive decay is a random process at the level of single atoms. It is impossible to predict the decay of a particular atom. However, for a collection of atoms, the decay is statistically governed by the radioactive decay law that predicts the transition probability per unit time by measured decay constants λ or half-lives $t_{1/2}$ [12]. For a given radioactive isotope, its decay constant is a characteristic property and defined as:

$$\lambda = \frac{\ln 2}{t_{1/2}} \tag{2.1}$$

For a certain radioisotope, with initial number of atoms N_o at $t = 0$, the number of the atoms remaining in the sample at time *t* is given by:

$$N(t) = N_o e^{-\lambda t} \tag{2.2}$$

The decay rate, i.e. *Activity* (number of decays per unit time), is defined as:

$$A = -\frac{dN}{dt} = \lambda N \tag{2.3}$$

The activity at a given time t can be calculated from a reference value A_o corresponding to an earlier time t_o:

$$A(t) = A_o e^{-\lambda(t-t_o)} \tag{2.4}$$

The SI unit of activity is *Becquerel* (Bq), defined as one decay per second [8].

2.2 Alpha decay

Many heavy nuclei, especially those of the naturally occurring radioactive series, decay through emission of an α particle (nucleus of ^4He atom). The spontaneous emission of such a nucleus rather than the emission of individual nucleons is more advantageous for the particularly high binding energy and tightly bound structure of the α particle [12]. The decay process can be represented by:

$$^A_Z X \rightarrow {}^{A-4}_{Z-2}Y + \alpha$$

2.2.1 Kinematics of alpha decay

Assuming the decaying nucleus $^A_Z X$ to be at rest, we have the energy balance of this process as Eq. (2.5):

$$m_X c^2 = m_Y c^2 + T_Y + m_\alpha c^2 + T_\alpha \tag{2.5}$$

The net energy release in the decay is given by the Q value:

$$Q = (m_X - m_Y - m_\alpha)c^2 = T_Y + T_\alpha \tag{2.6}$$

where T_α and T_Y are the kinetic energies of the α-particle and the daughter nucleus, respectively. T_α is expressed as

$$T_\alpha = Q(1 - 4/A) \tag{2.7}$$

The key characteristic of α decay kinematics is that the α particles emitted by a particular α emitter are monoenergetic, or several groups of monoenergetic α particles carrying a set of discrete energies. Such α emissions are usually

accompanied by emission of γ quanta of different discrete energies accordingly [13]. The α decay of ^{227}Th is taken as an example, as presented in Figure 2.2.

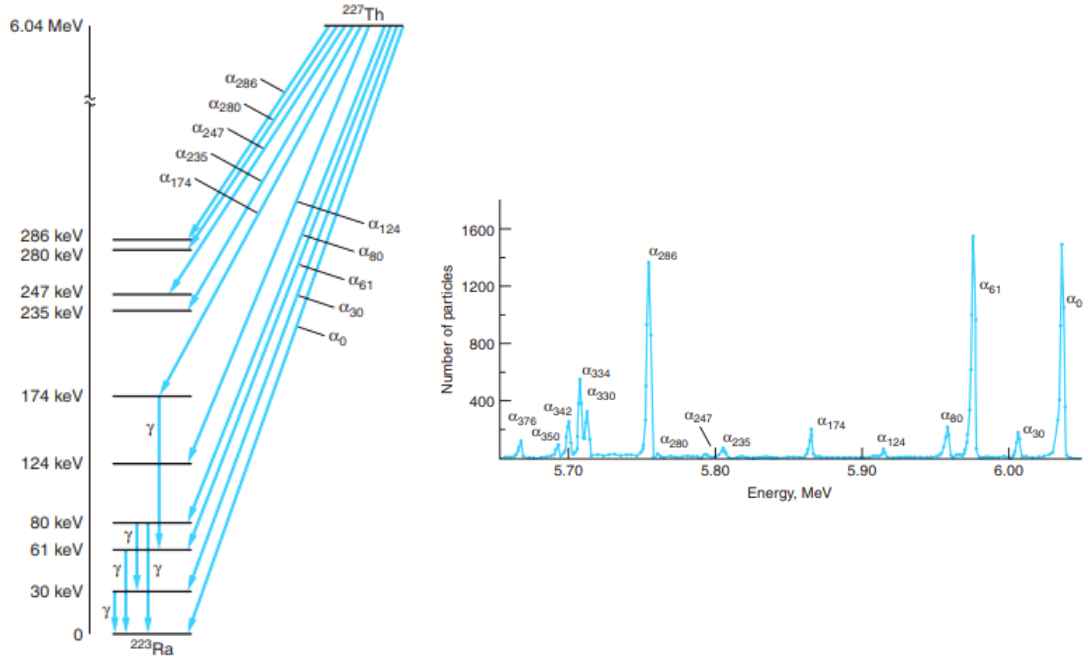

Figure 2.2: The lowest-lying energy levels of ^{223}Ra fed by ^{227}Th α decay (left) and the α particle energy spectrum of ^{227}Th (right) [14].

In the spectrum illustrated in Figure 2.2, α particles with the highest energy correspond to the decay to the ground state of ^{223}Ra with an energy of $Q = 6.04$ MeV. The next highest energy α particle α_{30}, with an energy of $Q = 6.01$ MeV, result from decay to the first excited state of ^{223}Ra at 30 keV above the ground state. And then, the ^{223}Ra nuclei de-excite to its ground state by γ emission of $E_\gamma = 30$ keV. Similarly, several groups of α particles with different energies are produced in decays to the other excited states of ^{223}Ra with γ emissions of different energies. Such de-excitation of the daughter nuclei occurs very fast, typically in time scale of the order of $10^{-13} - 10^{-15}$ seconds [14].

2.2.2 Mechanism of alpha emission

The emission of α particles could not be understood by classic theory of nucleus since from the classical point of view, in which an α particle considered

as trapped in a "potential well" created by the ensemble of nucleons does not have sufficient energy to escape the nucleus. However, the mechanism is well-explained by a quantum mechanical theory called "Quantum tunnelling". In this theory, the α particle is assumed to be preformed inside the parent nucleus and move in a spherical region determined by the daughter nucleus [12], despite that in reality the shape of the potential can be arbitrary. The plot in Figure 2.2 illustrates the potential energy between the centers of the daughter nucleus and the α particle separated at various distances.

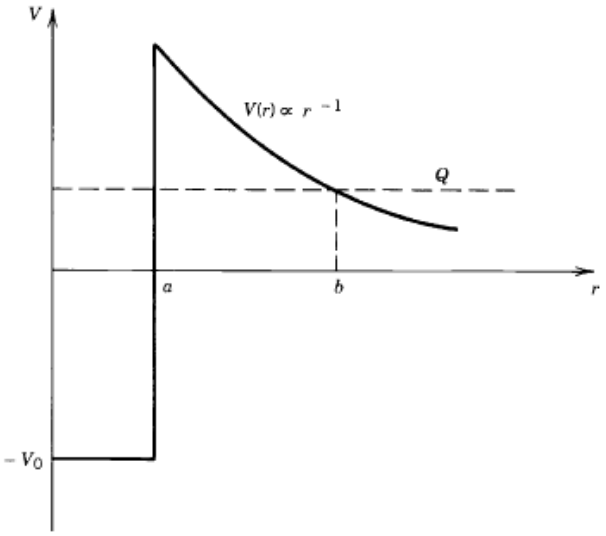

Figure 2.3: Potential energy of α particle and daughter nucleus system as a function of their separation: a is at nuclear surface, b is the tunnelling point [12].

In the spherical region $r < a$, there is a potential well of depth $-V_0$ inside the nucleus. The potential barrier extended in the annular-shell region $a \leq r < b$ is named Coulomb barrier, which can be modelled by Eq. (2.8):

$$V(r) = \begin{cases} \dfrac{Z_1 Z_2 e^2}{4\pi\varepsilon_0 r}, & r \geq a \\ -V_0, & r < a \end{cases} \tag{2.8}$$

where $Z_1 = 2$ is the proton number of α particle, Z_2 is the proton number of the daughter nucleus, e is electron charge, and r the separation. The constant $e^2/4\pi\varepsilon_o$= 1.440 MeV · fm. With the mass numbers of the daughter nucleus and the α particle, the nuclear radius a can be approximated as:

$$a = 1.25\text{fm} \cdot \left(A_D^{1/3} + A_\alpha^{1/3}\right) \tag{2.9}$$

The Coulomb barrier at $r = a$ has height

$$B = \frac{1}{4\pi\varepsilon_0}\frac{Z_1 Z_2 e^2}{a} \tag{2.10}$$

The radius b at which the α particle penetrates the potential barrier and escapes from the nucleus can be determined by Eq. (2.11).

$$b = \frac{1}{4\pi\varepsilon_0}\frac{Z_1 Z_2 e^2}{Q} \tag{2.11}$$

The decay constant of an α emitter is given by

$$\lambda = fP \tag{2.12}$$

where f is the knocking frequency at the barrier and P is the transmission probability through the barrier expressed by

$$P = e^{-2G} \tag{2.13}$$

The exponent G in Eq. (2.13) is called *Gamow factor*, defined as the probability factor for two nuclear particles to overcome the Coulomb barrier in nuclear reactions, as described by Eq. (2.14):

$$G = \sqrt{\frac{2m_\alpha}{\hbar^2 Q_\alpha}}\frac{2Z_D e^2}{4\pi\varepsilon_0}\left[\arccos\sqrt{\frac{Q_\alpha}{B}} - \sqrt{\frac{Q_\alpha}{B}\left(1 - \frac{Q_\alpha}{B}\right)}\right] \tag{2.14}$$

Gamow factor plays an important role in estimating the branching ratio and half-lives of different decay channels of a particular nuclide using Eq. (2.1), (2.12), and (2.13) as the branching ratio of a specific decay channel is given by

$$b_i = \frac{\lambda_i}{\lambda_{tot}} \tag{2.15}$$

Since the Coulomb barrier height B is radius-dependent, the Gamow factor is also useful in predicting the trend of half-lives with varying nuclear radii [12]. For example, changing the radius by 4% will result in a factor of 5 in half-life. This sometimes brings advantage in practice for identifying the spectral peaks of competing decay modes by their relative intensities.

2.3 Beta decay

Fast energetic electrons and positrons, referred to as β particles, are emitted in the decays of neutron rich and proton rich nuclei correspondingly. The former result from β^- decay and the latter result from electron capture (EC), or β^+ decay which has specific energy requirements. As illustrated in Figure 2.3, both neutron rich and proton rich nuclei tend to transmute to new elements located closer to the line of stability with more stable N/Z ratio. In the process of β decay both Z and N are changed by one unit: $Z \rightarrow Z \pm 1, N \rightarrow N \mp 1$, so that $A = Z + N$ remains constant. Stable nuclei are featured with a N/Z ratio at which the binding energy is at, or close to a local minimum. This effect can be explained by the nuclear binding energy defined by [15]:

$$B(A,Z) = a_V A - a_s A^{2/3} - a_C \frac{Z^2}{A^{1/3}} - a_A \frac{(A-2Z)^2}{A} \pm \delta(A,Z) \qquad (2.16)$$

where B is the total binding energy, expressed as the sum of volume energy, surface correction, Coulomb energy, symmetry term, and pairing term. The coefficients a_V, a_s, a_C, a_A, and δ are constants obtained by fitting the formula to experimentally determined values [15]. By ignoring the contribution of the pairing term $\pm\delta(A,Z)$ and minimizing $B(A,Z)$ with respect to Z in Eq. (2.16), the neutron-proton ration of the most stable nuclide for a given A can be obtained:

$$\frac{N}{Z} \approx 1 + \frac{a_C}{2a_A} A^{2/3} \qquad (2.17)$$

This relation shows that, for a nuclide to be stable, the value of N is larger than Z by a factor that scales as $A^{2/3}$. This is also indicated by the line of stability consisting of nuclides labelled by black dots in Figure 2.3.

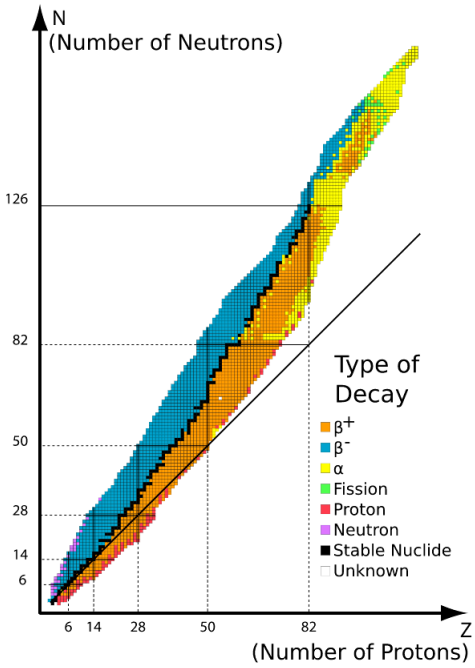

Figure 2.3: Valley of stability showing the various types of nuclear instability of radioisotopes and their decay modes towards the line of stability [16].

There are some special cases called *Magic number*. It has been experimentally observed that nuclei with either or both of the proton number and neutron number equalling to one of the numbers 2, 8, 20, 50, 82, and 126 are exceptionally stable when compared to the neighbouring nuclei. Those nuclei having both Z and N magic numbers are called *Doubly magic nuclei* and are particularly tightly bound and stable. For example, ${}_{2}^{2}He^{4}$, ${}_{8}^{8}O^{16}$, ${}_{20}^{20}Ca^{40}$, etc. [17].

2.3.1 Beta decay mechanism

The type of force that is responsible for β decay is the weak interaction. The β decay processes can be viewed in three perspectives:

- Nucleus perspective:
$$\begin{cases} \beta^-: {}_{Z}^{A}X \rightarrow {}_{Z+1}^{A}X' + e^- + \bar{\nu}_e \\ \beta^+: {}_{Z}^{A}X \rightarrow {}_{Z-1}^{A}X' + e^+ + \nu_e \\ EC: {}_{Z}^{A}X + e^- \rightarrow {}_{Z-1}^{A}X' + \nu_e \end{cases} \quad (2.18)$$

- Nucleon perspective:
$$\begin{cases} \beta^-: n \rightarrow p + e^- + \bar{\nu}_e \\ \beta^+: p \rightarrow n + e^+ + \nu_e \\ EC: p + e^- \rightarrow n + \nu_e \end{cases} \quad (2.19)$$

- Quark perspective:
$$\begin{cases} \beta^-: d \rightarrow u + e^- + \bar{\nu}_e \\ \beta^+: u \rightarrow d + e^+ + \nu_e \\ EC: u + e^- \rightarrow d + \nu_e \end{cases} \quad (2.20)$$

These three decay processes can be viewed with more microscopic details with the aid of Feynman diagrams in Figure 2.4:

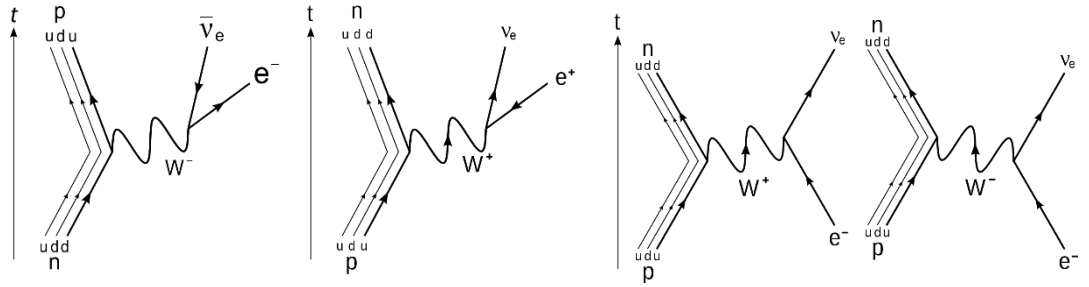

(a) (b) (c)

Figure 2.4: Feynman diagrams of (a). β^- decay, (b). β^+ decay, and (c). EC [16].

where a constituent down quark negatively charged by $\left(-\frac{1}{3}e\right)$ of a neutron converts to the up quark charged by $\left(+\frac{2}{3}e\right)$ forming a proton by emission of a W^- boson in β^-decay. The W^- boson subsequently decays into an electron and an electron antineutrino. However, β^+ decay only occurs when the daughter nucleus has a greater binding energy than the mother nucleus due to the neutron mass being greater than the proton mass and the fact that the Q value is always positive for any decay process to be energetically possible. Thus, in β^+ decay the weak interaction converts a proton into a neutron by converting a constituent up quark of a proton into a down quark. In contrast to β^-decay, this conversion is accompanied by the emission of a W^+ or the absorption of a W^- boson, which results in the emission of a positron and an electron neutrino. In EC decay mode, an electron interacts with a constituent *up* quark of a proton via either a W^+ or a W^- boson to create a down quark and an electron neutrino.

2.3.2 Beta decay energetics

In the case of free neutron decay, the energy released is expressed as Eq. (2.21):

$$Q = \left(m_n - m_p - m_e - m_{\bar{\nu}}\right)c^2 \tag{2.21}$$

For decays of neutrons at rest,

$$Q = T_p + T_e + T_{\bar{\nu}} \tag{2.22}$$

in which the proton recoil energy T_p amounts to only 0.3 keV and can be neglected. This leads to a continuous spectrum of the electron energy for the total decay energy being divided between the electron and the antineutrino.

$$Q = T_e + T_{\bar{\nu}} \tag{2.23}$$

The maximum electron energy in the case of a free neutron decay has been experimentally measured to be $(T_e)^{\max} = 0.782 \pm 0.013\ \text{MeV}$, in agreement with the value calculated using Eq. (2.21) with the measured neutron, proton, and electron masses:

$$\begin{aligned} Q &= \left(m_n - m_p - m_e - m_{\bar{\nu}}\right)c^2 \\ &= 939.573\ \text{MeV} - 938.280\ \text{MeV} - 0.511\ \text{MeV} - m_{\bar{\nu}}c^2 \\ &= 0.782\ \text{MeV} - m_{\bar{\nu}}c^2 \end{aligned}$$

Thus, the antineutrino and similarly the electron neutrino can be regarded as massless to within the precision of the measured maximum energy (about 13 keV) [12].

For a typical β^- decay in a nucleus, its energy released can be determined with the masses involved, as follows:

$$\begin{gathered} {}^{A}_{Z}X_N \rightarrow {}_{Z+1}{}^{A}X'_{N-1} + e^- + \bar{\nu} \\ Q_{\beta^-} = [m_N({}^{A}_{Z}X) - m_N({}_{Z+1}{}^{A}X') - m_e]c^2 \end{gathered} \tag{2.24}$$

where m_N represents nuclear masses, which can be converted into the tabulated neutral atomic masses denoted by $m(^AX)$. Since the atomic mass of nucleus ^AX equals

$$m(^AX)c^2 = m_N(^AX)c^2 + Zm_ec^2 - \sum_{i=1}^{Z} B_i \tag{2.25}$$

The binding energy of all i^{th} electron B_i is summed up in Eq. (2.25), then the Q value is expressed in terms of atomic masses.

$$Q_{\beta^-} = \{[m(^AX) - Zm_e] - [m(^AX') - (Z+1)m_e] - m_e\}c^2 + \left\{\sum_{i=1}^{Z} B_i - \sum_{i=1}^{Z+1} B_i\right\} \tag{2.26}$$

The electron masses cancel out here and the differences in electron binding energy can be neglected. Then the decay energy becomes

$$Q_{\beta^-} = [m(^AX) - m(^AX')]c^2 \tag{2.27}$$

And again, the β^-decay energy is divided between the electron and neutrino:

$$Q_{\beta^-} = T_e + E_{\bar{\nu}} \tag{2.28}$$

From this relation a distribution of the electron energy can be obtained from zero to an upper limit, as shown in Figure 2.5, the maximum electron energy, which is called the *endpoint energy* corresponds to minimum energy of the antineutrino.

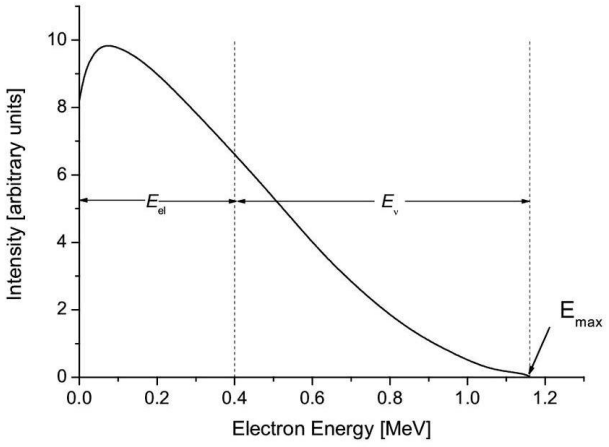

Figure 2.5: β decay spectrum of ^{210}Bi with endpoint energy 1.16 MeV [15].

In nuclear spectroscopy, the measured value of Q_{β^-} can be used to study some nuclear masses using Eq. (2.27). For example, with the measured Q_{β^-}, the mass of ^{210}Po as the β^-decay product can be determined from the mass of ^{210}Bi.

For a typical β^+decay process, the decay energy can be obtained similarly as with the β^-decay. However, the terms of electron masses do not cancel in this case and yield

$$ {}^{A}_{Z}X_N \rightarrow {}_{Z-1}{}^{A}X'_{N+1} + e^+ + \nu $$

$$ Q_{\beta^+} = [m({}^{A}X) - m({}^{A}X') - 2m_e]c^2 \tag{2.29} $$

For an electron capture process in a typical form of

$$ {}^{A}_{Z}X_N + e^- \rightarrow {}_{Z-1}{}^{A}X'_{N+1} + \nu $$

the atom X' immediately after the capture could be in an atomic excited state followed by transitions to lower states by emission of characteristic X-rays. This occurs when the capture takes place from an inner shell of the atom leaving an electronic vacancy in that shell. Such vacancy is quickly filled by downward transitions of electrons orbiting in higher shells. In this process, whether one X-ray is emitted or multiple, the total X-ray energy equals the binding energy B_n of the captured n-shell electron (n = K, L, etc). The atomic mass of X' immediately after the capture is greater than that in its atomic ground state by B_n. As a result, the Q value is then determined by

$$ Q_\varepsilon = [m({}^{A}X) - m({}^{A}X')]c^2 - B_n \tag{2.30} $$

All the above expressions refer to ground state to ground state decays. However, if the final nuclear state X' of the recoil is an excited state, the Q value must be accordingly decreased by the excitation energy of the state:

$$ Q_{ex} = Q_{G.S.} - E_{ex} \tag{2.31} $$

Beta plus decay and electron capture processes both originate from the initial proton-rich nucleus ${}^{A}_{Z}X_N$ to the final nucleus ${}_{Z-1}{}^{A}X'_{N+1}$. However, due to the

high energy requirement of β^+decay, when β^+decay is energetically possible for certain nuclei, electron capture may also take place. On the other hand, the reverse is not always true. It can be possible that $Q > 0$ for electron capture while $Q < 0$ for β^+decay. It is shown by Eq. (2.29) that, for a β^+decay to be energetically possible, the atomic mass difference between the mother nucleus and the daughter nucleus consequently must be at least $2m_e c^2 = 1.022$ MeV [12]. A typical Q value is around 1 MeV but can range from a few keV to tens of MeV.

It is stated by Fermi Theory of β decay that, the shape of the β energy spectrum is defined as a function of the momentum of the β particles.

$$N(p) = \frac{C}{c^2} p^2 \left[Q - \sqrt{p^2 c^2 + {m_e}^2 c^4} + m_e c^2 \right]^2 \tag{2.32}$$

where $N(p)$ is the number of electrons with momentum p, C is a constant, which can be determined experimentally. This facilitates obtaining a theoretical probability that the β particles are observed inside the energy gate $T_e \rightarrow dT_e$. According to Fermi's theory, the shape of the spectrum can be also expressed as a function of electron kinetic energy:

$$N(T_e) = \frac{C}{c^5} \left({T_e}^2 + 2T_e m_e c^2 \right)^{1/2} (Q - T_e)^2 (T_e + m_e c^2) \tag{2.33}$$

A graphical illustration of the momentum and energy distribution is plotted below:

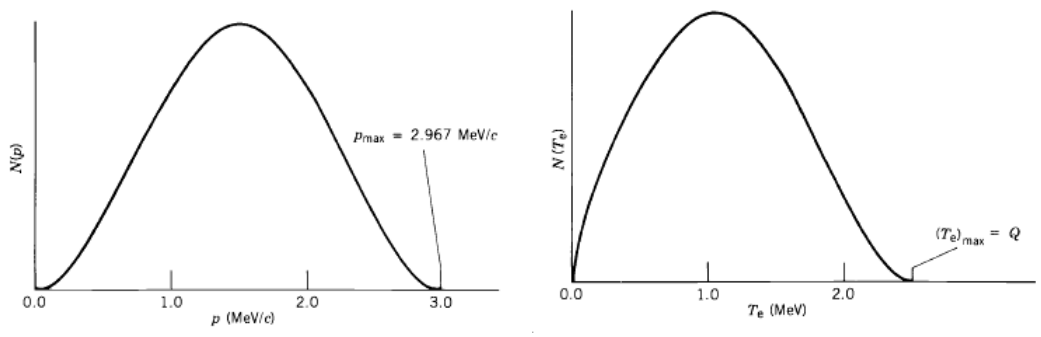

Figure 2.6: Expected electron energy (right) and momentum (left) distribution for $Q = 2.5$ MeV [12].

The number of electrons with kinetic energy between T_e and dT_e can be obtained by integrating Eq. (31) over the range in question. For example, the number of electrons with T_e between a MeV and b MeV is obtained by

$$N_{a\to b} = \int_a^b \frac{C}{c^5}\left({T_e}^2 + 2T_e m_e c^2\right)^{1/2}(Q - T_e)^2(T_e + m_e c^2)dT_e \qquad (2.34)$$

The total counts of $0 < T_e \leq Q$ can be obtained by the area covered by the entire curve:

$$N_{tot} = \int_0^Q \frac{C}{c^5}\left({T_e}^2 + 2T_e m_e c^2\right)^{1/2}(Q - T_e)^2(T_e + m_e c^2)dT_e \qquad (2.35)$$

And then, the probability of detecting β particles with energy $a < T_e \leq b$ can be determined by using Eq. (2.36). This practically give a rough estimate of the tagging efficiency along a specific energy gate set in β-tagging.

$$\mathcal{P}_{a\to b} = \frac{N_{a\to b}}{N_{tot}} \cdot 100\%$$

$$= \frac{\int_a^b \frac{C}{c^5}\left({T_e}^2 + 2T_e m_e c^2\right)^{1/2}(Q - T_e)^2(T_e + m_e c^2)dT_e}{\int_0^Q \frac{C}{c^5}\left({T_e}^2 + 2T_e m_e c^2\right)^{1/2}(Q - T_e)^2(T_e + m_e c^2)dT_e} \cdot 100\% \qquad (2.36)$$

2.3.3 Classification of transitions in beta decay

If the β decay process is assumed to take place at the origin ($r = 0$), where the electron and neutrino have been created, the orbital angular momentum carried by the emitted particles are zero. The change in angular momentum of the nucleus results from the spins of the electrons and neutrinos, each with $s = \frac{1}{2}$. Their spins can be either parallel with total $S = 1$, or antiparallel with total $S = 0$. If the electron and neutrino carry no orbital angular momentum ($l = 0$), then initial and final states must have identical parities since the parity is associated with orbital angular momentum by $\pi = (-1)^l$. In this context,

transitions in allowed β decay is classified by the angular momentum and parity selection rules:

$$\Delta I = 0,1 \qquad \Delta\pi = \text{no}$$

Fermi transition: when ev spins anti-align, $S = 0$.

Gamow-Teller transition: when ev spins align in parallel, $S = 1$.

In some allowed β decay processes there exists "mixed" $F + GT$ transition, in which both the Fermi (F) and Gamow-Teller (GT) selection rules are satisfied. Here are some examples of the three types of transition below:

$$^{14}Cl \rightarrow {}^{34}S\text{:}\ \ 0^+ \rightarrow 0^+ \qquad Pure\ Fermi\ transition$$

$$^{6}He \rightarrow {}^{6}Li\text{:}\ \ 0^+ \rightarrow 1^+ \qquad Pure\ Gamow-Teller\ transition$$

$$n \rightarrow p\text{:}\ \ \frac{1}{2}^+ \rightarrow \frac{1}{2}^+ \qquad F + GT\ mixed\ transition$$

In such kind of $F + GT$ mixed transition, the ration of the Fermi and Gamow-Teller amplitude can be determined by

$$y = \frac{g_F M_F}{g_{GT} M_{GT}} \tag{2.37}$$

where M_F and M_{GT} are the Fermi and Gamow-Teller nuclear matrix elements, g_F and g_{GT} are the strength constants, respectively. Some examples are listed in Table 2.1:

Table 2.1: Ratio of Fermi to Gamow-Teller Matrix Elements [12].

	Decay	$y = g_F M_F / g_{GT} M_{GT}$	%F	%GT
Mirror decays	$n \rightarrow p$	0.467 ± 0.003	18	82
	$^{3}H \rightarrow {}^{3}He$	0.479 ± 0.001	19	81
	$^{13}N \rightarrow {}^{13}C$	1.779 ± 0.006	76	24
	$^{21}Na \rightarrow {}^{21}Ne$	1.416 ± 0.012	67	33
	$^{41}Sc \rightarrow {}^{41}Ca$	0.949 ± 0.003	47	53
Nonmirror decays	$^{24}Na \rightarrow {}^{24}Mg$	-0.021 ± 0.007	0.044	99.956
	$^{41}Ar \rightarrow {}^{41}K$	$+0.027 \pm 0.011$	0.073	99.927
	$^{46}Sc \rightarrow {}^{46}Ti$	-0.023 ± 0.005	0.053	99.947
	$^{52}Mn \rightarrow {}^{52}Cr$	-0.144 ± 0.006	2	98
	$^{65}Ni \rightarrow {}^{65}Cu$	-0.002 ± 0.019	< 0.04	> 99.96

In contrary to allowed transitions, some decays being less probable with generally longer half-lives are called "*Forbidden decays*". However, if the allowed matrix elements happen to vanish in some cases, then the forbidden decays are the only possible transitions to occur. Forbidden decays are characterized by

$$\Delta I = 0,1,2 \qquad \Delta\pi = yes$$

The total decay rate is measured by *comparative half-life*, also known as the ft value given by Eq. (2.38), which gives an estimate of the β decay probabilities among different nuclei. The ft value can be quite large; therefore, it can be more conveniently presented by the "$\log ft$" value instead.

$$ft_{1/2} = 0.693 \frac{2\pi^3 \hbar^7}{g^2 {m_e}^5 c^4 \left|M_{fi}\right|^2} \tag{2.38}$$

A practical approach to obtain the $\log ft$ value is done using the relation $\log_{10} ft = \log_{10} f + \log_{10} t_{1/2}$ with the aid of a set of reference curves:

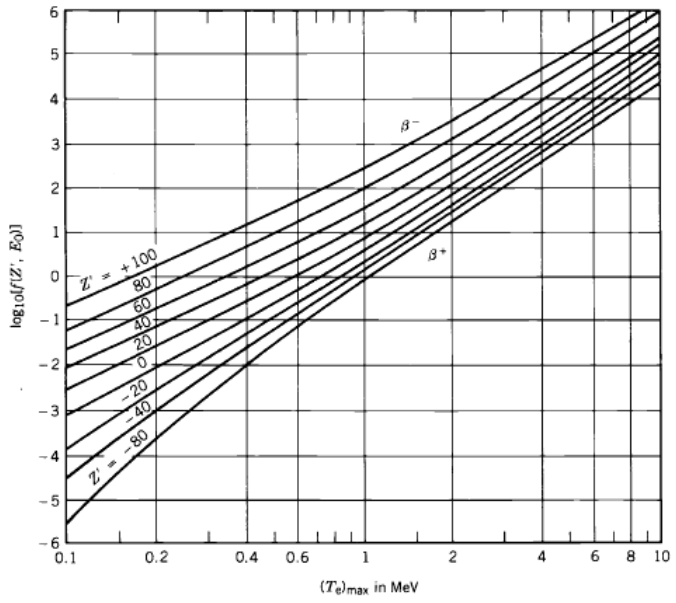

Figure 2.7: The Fermi integral for $\log_{10} f$ values. The atomic number Z' refers to the daughter nucleus; the curves for positive Z' are for β^-decay, while negative Z' is for β^+decay [12].

Transitions in β decay are further classified by *Forbiddenness*, as shown in Table 2.2:

Table 2.2: Classification of β decay transitions by forbiddenness [12].

Type of Transition	Selection Rules	L_{ev}	$\Delta\pi$	ft
Superallowed	$\Delta I = 0, \pm 1$	0	No	$1 \times 10^3 - 1 \times 10^4$
Allowed	$\Delta I = 0, \pm 1$	0	No	$2 \times 10^3 - 10^6$
1st forbidden	$\Delta I = 0, \pm 1$	1	Yes	$10^6 - 10^8$
Unique 1st forbidden	$\Delta I = \pm 2$	1	Yes	$10^8 - 10^9$
2nd forbidden	$\Delta I = \pm 1, \pm 2$	2	No	$2 \times 10^{10} - 2 \times 10^{13}$
Unique 2nd forbidden	$\Delta I = \pm 3$	2	No	10^{12}
3rd forbidden	$\Delta I = \pm 2, \pm 3$	3	Yes	10^{18}
Unique 3rd forbidden	$\Delta I = \pm 4$	3	Yes	4×10^{15}
4th forbidden	$\Delta I = \pm 3, \pm 4$	4	No	10^{23}
Unique 4th forbidden	$\Delta I = \pm 5$	4	No	10^{19}

2.3.4 Special cases in beta decay

- Double β decay

The double β decay occurs when single β decay final state is less accessible, this can be well-explained by an example of the decay of ^{48}Ca. The Q value for β^-decay to ^{48}Sc is 0.281 MeV, but the only possible states of ^{48}Sc in this decay would be the 4^+, 5^+, and 6^+ states, which would correspond to either fourth- or sixth-forbidden decays. Regarding this decay channel, the half-live is estimated from the log ft value to be $t_{1/2}$~$10^{25}s$ (about 10^{18} years. Thus, ^{48}Ca could be regarded as "stable". The decay scheme of ^{48}Ca is illustrated in Figure 2.8:

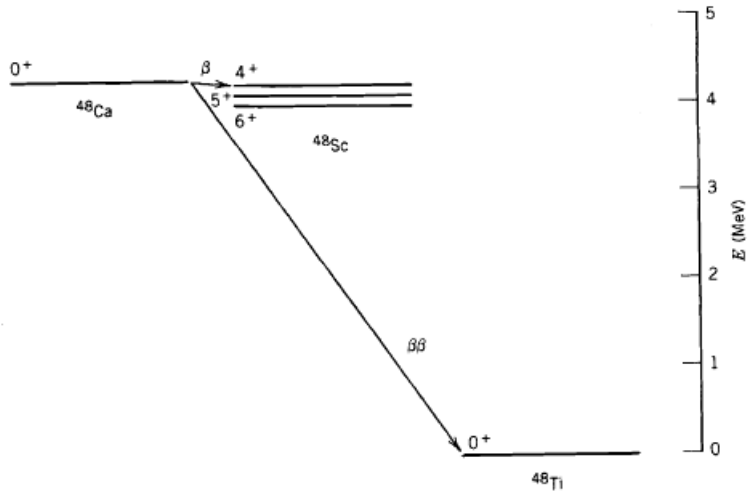

Figure 2.8: Superallowed double β decay of ^{48}Ca to ^{48}Ti as an alternative channel to the fourth-forbidden single β decay to ^{48}Sc [12].

The direct process of this decay $^{48}Ca \rightarrow {}^{48}Ti + 2e^- + 2\bar{\nu}$ takes advantage of the nature $0^+ \rightarrow 0^+$ bringing this transition in the Superallowed, rather than the fourth-forbidden category.

- Inverse β decay

The process closely involved in β decay that, capture of a neutrino or an antineutrino by a nucleon is referred to as *inverse β decay:*

$$\bar{\nu} + p \rightarrow n + e^+$$

$$\nu + n \rightarrow p + e^-$$

These processes are governed by the law of lepton conservation that states, the total number of leptons minus antileptons on each side of a decay or reaction process must remain unchanged. This makes the process $\bar{\nu} + p \rightarrow n + e^-$ impossible to occur because the lepton number is not conserved when an antilepton $\bar{\nu}$ is converted into a lepton e^-. However, what makes the study of these reactions quite difficult is the cross section, of the order of 10^{-19} barns, which is extremely small when compared to typical nuclear reaction cross sections, of the order of 1 barn (10^{-24}cm^2) [18].

2.4 Gamma decay

Gamma ray is high energy photons with extremely short wavelength emitted during γ decay that normally occurs in conjunction with other nuclear processes. The daughter nucleus after some α or β decays, and most nuclear reactions, is formed in an excited state followed by rapid decay to the ground state via the emission of one or several γ rays [12]. Moreover, γ emission occurs in many processes of particle physics as well. For example, in the electron-positron annihilation there are two γ photons emitted, each with an energy of 511 keV. The typical energy of γ decay ranges from a few keV up to about 10 MeV, with wavelength typically ranging from about 20 to 2000 fm. However, γ rays with extremely high energy ranging from 100 to 1000 TeV have been observed in nuclear astrophysics [19].

Photons carry no mass and charge, and thus, γ radiation is referred to electromagnetic radiation, which is the most penetrating radiation among the three major types of radioactive decay. As depicted in Figure 2.9, γ radiation requires more effective shielding than α or β particles.

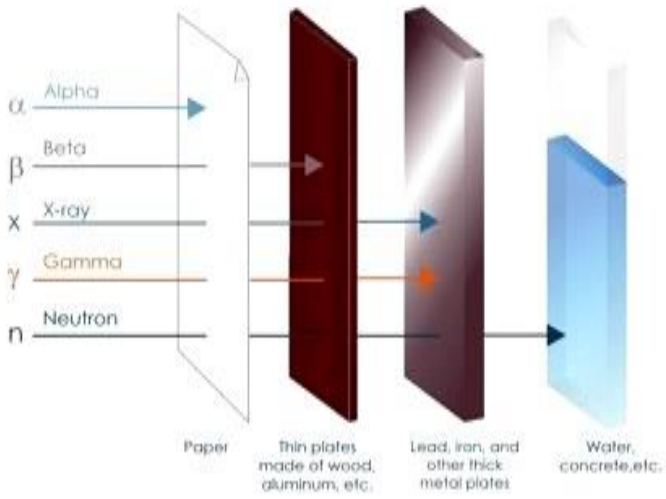

Figure 2.9: Penetrating power of various radiation types and corresponding shielding requirements [9].

2.4.1 Gamma decay energetics

For a nucleus of mass M at rest decaying from an initial excited state E_i to a final state E_f, linear momentum is conserved, resulting in the final recoil nucleus with a recoil momentum P_r and correspondingly kinetic energy T_r, which is supposed to be nonrelativistic $\left(T_r = {P_r}^2/2M\right)$.

$$ {}^{A}_{Z}X^{*}_{N} \rightarrow {}^{A}_{Z}{X'}_{N} + \gamma $$

Total energy and momentum are conserved,

$$ E_i = E_f + E_\gamma + T_r \tag{2.39} $$

$$ 0 = \vec{p}_r + \vec{p}_\gamma \tag{2.40} $$

The decay energy takes the form

$$Q = \Delta E = E_i - E_f = E_\gamma + T_r \tag{2.41}$$

For low-energy γ decays, the recoil energy counts for less than 1eV, in high energy γ decays, such as the neutron capture emitting 5 – 10 MeV γ rays, energy gained by the recoils ranges up to 100 eV. Therefore, in either case the recoil energy can be regarded as $T_r \approx 0$ and the approximation $\Delta E \cong E_\gamma$ is reasonable. As a rough estimate, the energy differences ΔE are usually of the order of a few MeV or less, while the rest mass energies Mc^2 are of the order of $A \times 10^3$ MeV [12]. Since $\Delta E \ll Mc^2$, with the relativistic relationship $E_\gamma = cp_r$ the expression of decay energy becomes

$$Q = \Delta E = E_i - E_f = E_\gamma + \frac{{E_\gamma}^2}{2Mc^2} \tag{2.42}$$

Solving Eq. (2.42) gives

$$E_\gamma = Mc^2 \left[-1 \pm \left(1 + 2\frac{\Delta E}{Mc^2} \right)^{1/2} \right] \tag{2.43}$$

which can be simplified to a precision of the order of about 10^{-5} by adopting the first three terms in the expansion of the square root:

$$E_\gamma \cong \Delta E - \frac{(\Delta E)^2}{2Mc^2} \tag{2.44}$$

2.4.2 Multipolarity and parity selection rules

The conservation of angular momentum plays a dominant role in the γ decay process as it has provided an enormous range of information on the structure of nuclei. In the γ decay of a stationary nucleus in a definite quantum mechanical state, both the initial and final states will have a definite angular momentum and parity. Parity and momentum must be conserved by the emitted photon connecting the two states [18]. With the spins of initial and final states known as I_i and I_f respectively, the angular momentum L carried by the emitted photon must lie within the range between $|I_i - I_f|$ and $I_i + I_f$, where

$L = 0$ is forbidden for the emission of a single photon. The parities of electric and magnetic multipoles differ as

$$\begin{aligned} \pi(ML) &= (-1)^{L+1} \\ \pi(EL) &= (-1)^{L} \end{aligned} \tag{2.45}$$

Therefore, the multipolarity of an electromagnetic transition is determined by the following angular momentum and parity selection rules, which are summarized in Table 2.3 [12]:

$$\begin{aligned} &\left|I_i - I_f\right| \leq L \leq I_i + I_f \quad (L = 0 \text{ is forbidden}) \\ &\Delta\pi = no: \quad \textit{even electric}, \ \text{odd magnetic} \\ &\Delta\pi = yes: \quad \textit{odd electric}, \ \text{even magnetic} \end{aligned} \tag{2.46}$$

Table 2.3: Gamma ray selection rules and multipolarities [18].

Radiation Type	Name	$l = \Delta I$	$\Delta\pi$
E1	Electric dipole	1	Yes
M1	Magnetic dipole	1	No
E2	Electric quadrupole	2	No
M2	Magnetic quadrupole	2	Yes
E3	Electric octupole	3	Yes
M3	Magnetic octupole	3	No
E4	Electric hexadecapole	4	No
M4	Magnetic hexadecapole	4	Yes

In most cases the spins I_i and I_f have such values that the selection rules permit several multipoles to be emitted, in which the transition type with smallest possible L is most likely to dominate. A general prediction of the transition probability of some lower multipole orders can be obtained by the Weisskopf estimates of transition rate:

Table 2.4: Weisskopf estimates of single-photon transition rates [18].

Multipole	E	M
l	$\lambda\,(s^{-1})$	$\lambda\,(s^{-1})$
1	$1.03 \times 10^{14}\ A^{2/3}E_\gamma^3$	$3.15 \times 10^{13}\ E_\gamma^3$
2	$7.28 \times 10^{7}\ A^{4/3}E_\gamma^5$	$2.24 \times 10^{7}\ A^{4/3}E_\gamma^5$
3	$3.39 \times 10^{1}\ A^{2}E_\gamma^7$	$1.04 \times 10^{1}\ A^{4/3}E_\gamma^7$
4	$1.07 \times 10^{-5}\ A^{8/3}E_\gamma^9$	$3.27 \times 10^{-6}\ A^{2}E_\gamma^9$
5	$2.40 \times 10^{-12}\ A^{10/3}E_\gamma^{11}$	$7.36 \times 10^{-13}\ A^{8/3}E_\gamma^{11}$

where E_γ is in MeV. These estimates provide reasonable prediction of the ratio of transition rates, rather than precise theoretical prediction.

2.4.3 Internal conversion

Internal conversion (IC) is an electromagnetic process competing with γ decay when the electromagnetic multipole fields of the excited nucleus interact with an atomic orbital electron and eject it from the atom. Both γ decay and internal conversion are due to the action of the electromagnetic force. However, in some cases the transitions cannot occur through single γ-ray emission [15]. Generally, internal conversion is dominant more significantly for high Z elements, higher multipolarities and low transition energies [20]. In some cases, the transitions via single photon emission is also forbidden due to angular momentum conservation principle. For instance, in the $0^+ \rightarrow 0^+$ transition, there is neither transfer of angular momentum nor change in parity. Since photon's intrinsic spin is $s = 1$, emission of a single γ photon by which conservation of angular momentum would be violated, is not allowed [20].

For a specific nuclear level, the total decay probability consists of two components arising from γ emission and internal conversion, respectively:

$$\lambda_{tot} = \lambda_\gamma + \lambda_e \tag{2.47}$$

The probability of conversion electron emission relative to γ emission is evaluated by internal conversion coefficient α.

$$\alpha = \frac{\lambda_e}{\lambda_\gamma} \tag{2.48}$$

α is defined as the total internal conversion coefficient, which sums up all partial conversion coefficients:

$$\alpha = \alpha_K + \alpha_L + \alpha_M + \cdots \tag{2.49}$$

Then the total decay probability becomes

$$\begin{aligned}\lambda_{tot} &= \lambda_\gamma(1+\alpha) \\ &= \lambda_\gamma + \lambda_{e.\ K} + \lambda_{e.\ L} + \lambda_{e.\ M} + \cdots \\ &= \lambda_\gamma(1+\alpha_K+\alpha_L+\alpha_M+\cdots\end{aligned} \tag{2.50}$$

The conversion coefficients for electric (E) and magnetic (M) multipoles are given by

$$\begin{aligned}\alpha(EL) &\cong \frac{Z^3}{n^3}\left(\frac{L}{L+1}\right)\left(\frac{e^2}{4\pi\epsilon_0\hbar c}\right)^4\left(\frac{2m_ec^2}{E_\gamma}\right)^{L+5/2} \\ \alpha(ML) &\cong \frac{Z^3}{n^3}\left(\frac{e^2}{4\pi\epsilon_0\hbar c}\right)^4\left(\frac{2m_ec^2}{E_\gamma}\right)^{L+3/2}\end{aligned} \tag{2.51}$$

where the index $L = 1, 2, 3, 4, \ldots$ corresponds to dipole, quadrupole, octupole, hexadecapole, and so on [8].

In the IC process the nuclear excitation energy is transferred to the ejected electron through a radiationless process. The energy of the IC electron is given by

$$T_e = \Delta E - B_e \tag{2.52}$$

where ΔE presents the transition energy between the initial and final states, B_e is the electron binding energy that varies with the atomic orbital, resulting in IC electrons emitted with differing energies. It is suggested by Eq. (2.52) that the internal conversion process has a threshold energy equal to the electron binding energy in a particular shell [12]. Determination of conversion electron energies can be illustrated with an example of the ^{203}Hg → ^{203}Ti β decay:

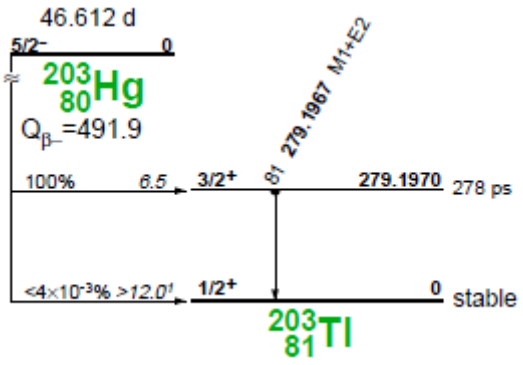

Figure 2.10: $^{203}_{80}Hg_{123} \longrightarrow {}^{203}_{81}Tl_{122}$ transition scheme [21].

The ^{203}Hg $5/2-$ state decays to ^{203}Tl and produces a continuous β energy spectrum with maximum energy 213 keV, as depicted in Figure 2.11 (a). Figure 2.10 shows that the $3/2+$ excited state in ^{203}Tl de-excites with $t_{1/2} \approx 280$ ps to the ground state with $Q \cong 279.190$ keV. With the electron binding energies provided in the Table of Isotopes, the kinetic energies of the conversion electrons can be calculated, as tabulated in Table 2.5.

Table 2.5: B_e and T_e associated with the $^{203}_{80}Hg_{123}$ IC transition [12].

X-ray notation	spectroscopic notation	B (keV)	T_e (keV)
K	$1s_{1/2}$	85.529	193.661
L_I	$2s_{1/2}$	15.347	263.843
L_{II}	$2p_{1/2}$	14.698	264.492
L_{III}	$2p_{3/2}$	12.657	266.533
M_I	$3s_{1/2}$	3.704	275.486

Unlike the continuous electron energies in the case of β decay, the conversion electrons are monoenergetic. This carries an advantage in certain applications, for instance, in energy calibration of a β detector [8]. As illustrated in the ^{203}Hg conversion electron spectrum shown in Figure 2.11, the peaks corresponding to the conversion electrons ejected from different shells are clearly visible as individual peaks.

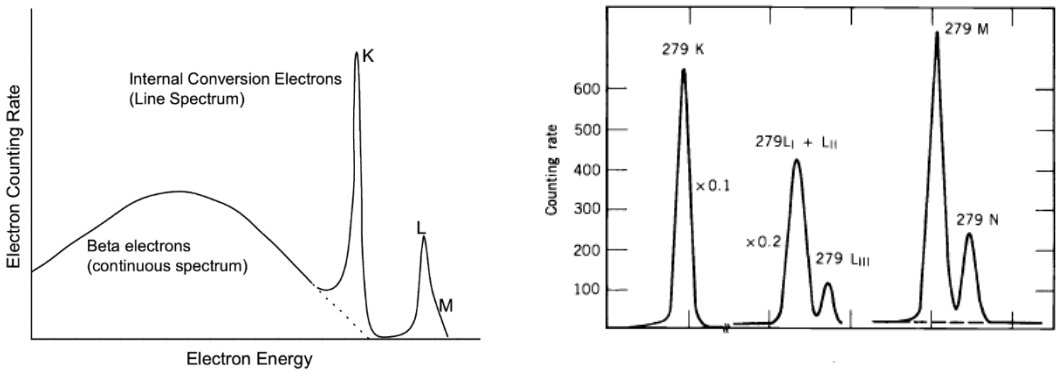

(a) (b)

Figure 2.11: Electron spectrum from the ^{203}Hg decay. (a). Continuous β spectrum along with the K, L, and M conversion electrons. (b). More detailed spectra can be defined at higher resolution [8].

3. Plastic scintillator

The term *scintillator* is defined as such kind of material that converts the energy carried by ionizing radiation into light through the process of scintillation when struck and excited by the radiation. Different types of organic and inorganic scintillators have been successfully used in nuclear and particle physics as a radiation detection tool when coupled with appropriate light readout devices, such as silicon photomultiplier (SiPM) [1]. In this thesis project the EJ-248 PVT-based plastic scintillators produced by Eljen Technology were used in the design and tests. The material was designed on a polyvinyl toluene (PVT) base, doped with fluors that minimizes attenuation of scintillation photons and improves tolerance against elevated temperatures [22].

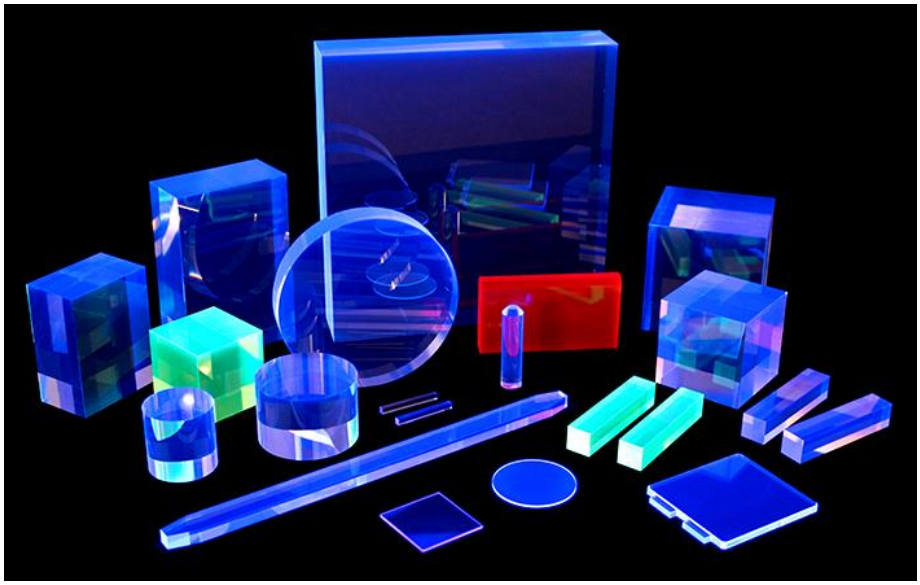

Figure 3.1: Plastic scintillators machined into different shapes [22].

Plastic scintillators have been proven to possess high performance in β particle spectroscopy for the fast response and efficient stopping power against the passage of β particles. Another major advantage of plastic scintillators is the mechanical robustness when being machined into optimal geometrical shapes. Furthermore, plastic scintillators are sensitive to γ rays. Despite that the interaction probability of a plastic scintillator with γ rays is lower than that of

a Ge detector, the γ ray attenuation can be reduced by using a plastic scintillator. Ideal scintillators should have the following properties:

1. High efficiency when converting radiation energy into detectable light.
2. Behaves linearly when converting the deposited energy to light yield.
3. Transparent to the wavelength of its own emission of light.
4. Short enough decay time of induced luminescence to generate fast signals.
5. Index of refraction ~ 1.5 for efficient coupling with the photosensor.

However, in practice no material simultaneously meets all the above criteria. The degree to which a particular material meets these criteria is a measure of its suitability for use as a scintillator [8].

3.1 Scintillation mechanism

PVT scintillators are made up of long chain of vinyl toluene molecules. The molecular structure of toluene consists of a benzene ring (C_6H_6) bonded to a methyl (CH_3) and a vinyl group ($CH_2 - C\mathrm{H} -$) [23]. A common feature of most organic scintillators is the benzene ring, characterized by delocalization of three π-bonds. As a result, a cloud of electrons is created above and below the molecular plane, respectively, as depicted in Figure 3.2. The PVT molecules orienting in the same direction are held together by Van Der Waals force rather than bonded through covalent bonds within an arranged crystal lattice [24].

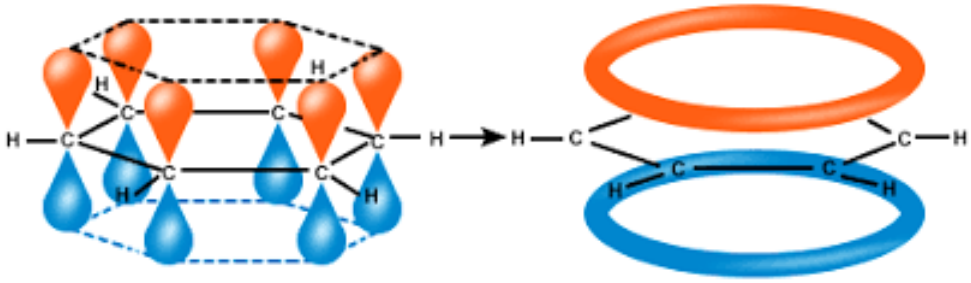

Figure 3.2: Delocalization of the π-bond electrons of benzene ring [25].

The scintillation phenomenon begins with exciting the π-electron configuration of the molecule into the excited states. A series of singlet states (spin 0) labelled as S_0, S_1, S_2, ... and a similar set of triplet (spin 1) electronic levels labelled as T_0, T_1, T_2, ... are drawn to illustrate the energy levels of the PVT molecule, as depicted in Figure 3.3, where S_0 and T_0 are the ground states. For the PVT molecules in question, the energy spacing typically ranges around 3~4 eV between the S_0 and S_1 states, while spacing between higher-lying states is somewhat smaller. Each of these electronic configurations is further partitioned to vibrational levels, which have finer spacing, typically of the order of 0.15 eV. Nearly all molecules at room temperature are in the S_{00} state since the spacing between vibrational states is relatively large compared to the average thermal energies (0.025 eV).

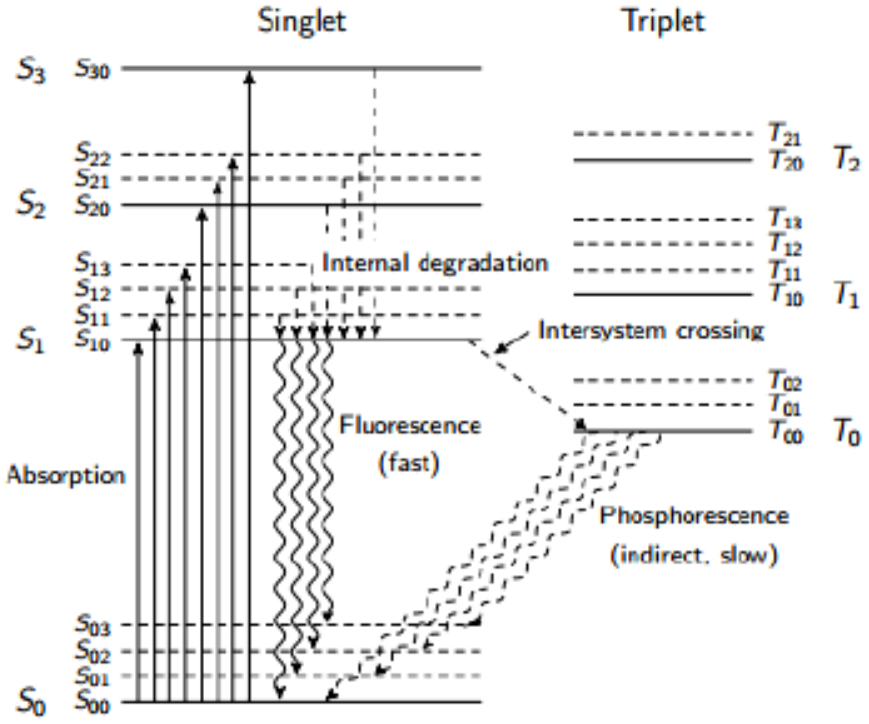

Figure 3.3: Energy transitions of PVT molecule with π-electron structure [26].

The luminescence process of an organic scintillator consists of three stages, fluorescence, phosphorescence, and delayed fluorescence.

- ***Fluorescence*:**

When the energy of the ionizing radiation is absorbed by the molecule, π-electrons are excited to any of a number of the higher singlet energy states in time scale of $\sim 10^{-12}$s. The energy of the excited π-electron states is then rapidly ($\sim 10^{-10}$s) dropped by de-excitation to any of the vibrational states S_{1n} through non-radiative internal conversion. Then, the vibrational states of S_1 lose the vibrational energy within $\sim 10^{-12}$s by de-excitation and become in thermal equilibrium with the neighbouring states resulting in, after a negligibly short time, a population of the S_{10} state. The prompt scintillation light is emitted within $10^{-8}$to $10^{-9}s$ and fluorescence spectrum is created when these S_{10} states de-excite and end up into any vibrational S_0 state [26]. The decay of the fluorescence intensity is described as a function of time by Eq. (3.1):

$$I = I_0 e^{-t/\tau} \tag{3.1}$$

where I_0 and I denote the initial intensity and intensity at time t following excitation, respectively, τ is the fluorescence decay time for the S_{10} level, which is typically of the order of $\sim 10^{-9}$s for most organic scintillators [8].

- ***Phosphorescence***

Besides the $S_1 \longrightarrow S_0$ de-excitation, as can be seen from Fig. 3.3, there also exists inter-system crossing $S_1 \longrightarrow T_1$, through which some excited singlet states feed into the triplet T_1 states. And then, the T_1 states de-excite with lifetime of $\sim 10^{-3}$s to S_0 by a delayed light emission characterized as phosphorescence. According to Figure 3.3, T_{1n} states lie higher in energy level than S_{1n} states and the de-excitation of the excited triplet state is strongly forbidden, such phosphorescence spectrum is characterized with longer wavelength than that of the fluorescence [8]. The phosphorescence emission follows similar exponential decay as fluorescence, but with a longer decay time of the order of $\sim 10^{-4}$s.

- *Delayed fluorescence*

Some molecules in the T_1 state get thermally excited back to the S_1 state instead of direct decay, via combination with another T_1 state and subsequently decay through normal fluorescence [1].

$$T_1 + T_1 \longrightarrow S_1 + S_0 + phonons \tag{3.2}$$

As shown in Fig. 3.3, the upward arrows corresponding to the photon energies absorbed in the material, are longer than the downward arrows representing the fluorescence transitions (with exception of $S_{10} \longrightarrow S_{00}$). The fluorescence transitions generally occur with less energies than the minimum required for excitation, with very little overlap between the optical absorption and emission spectra. For this reason, the organic scintillators are transparent to their own fluorescent emission with insignificant self-absorption of the fluorescence. This is known as the Stokes shift.

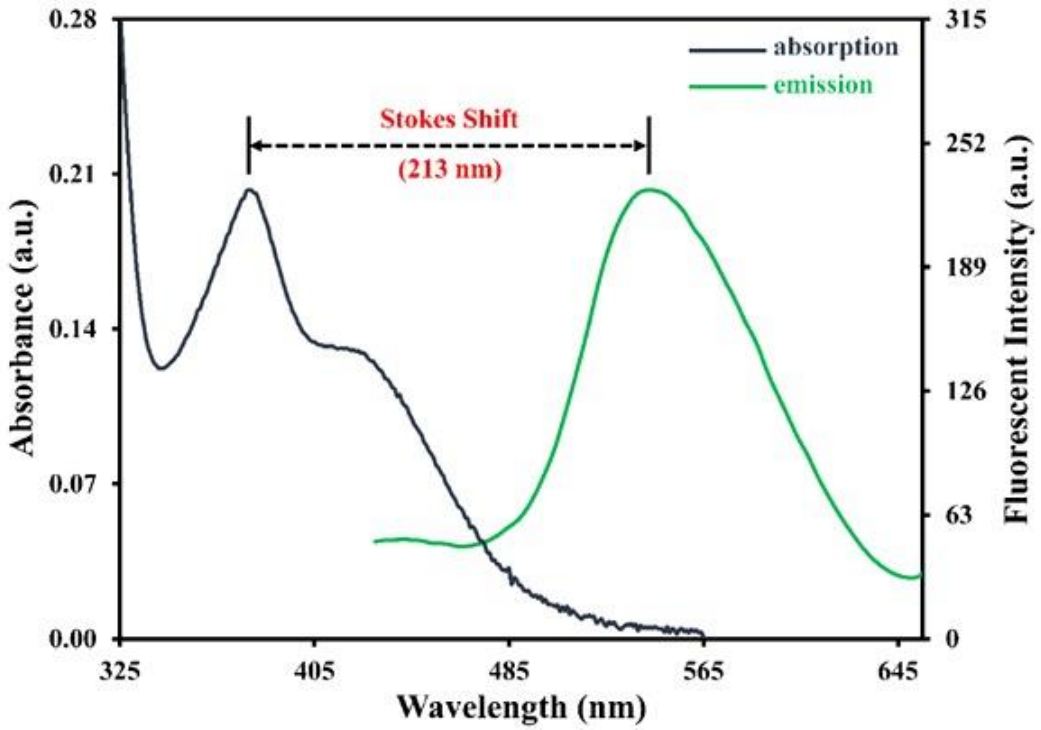

Figure 3.4: Absorption and fluorescence emission spectral profiles governed by Stokes shift [27].

The performance of organic scintillators is commonly weakened by temperature increase caused by heat deposition during measurements. For example, the light output of all organic scintillators is inversely dependent on temperature. Sometimes the scintillator can be seriously damaged, if irradiated e.g. by high-energy gammas for a long time. However, the physical properties of plastic scintillators have been greatly improved by modern technology and with chemical modifications. The detailed technical specification of EJ-248 scintillator is available in Appendix A.

3.2 Interaction with heavy charged particles

Heavy charged particles (HCP), such as protons and α particles, immediately interact with many atomic electrons when incident on the detector material. Incident HCPs may also interact with nuclei, e.g. in Rutherford scattering or α-particle-induced reactions. Such interactions are rare and insignificant in the response of radiation detectors [8]. The interactions are caused by the Coulomb force interacting between the positively charged incident heavy particle and negatively charged atomic electron. Along with its passage through the detector material, the incident particle continuously interacts with many electrons and loses its kinetic energy until the particle is stopped. Such energy transfer results in excitation of the detector material atom by exciting the bond electron to a higher-lying shell or ionization of the atom by pure scattering, so that the atomic electron is liberated from the atom [8]. The maximum transferable energy to an electron depends on the mass m_0 and momentum of the incident particle [28]. Given the relativistic momentum of the incident particle

$$p = \gamma m_0 \beta c \tag{3.3}$$

where m_0 is the rest mass, $\beta c = v$ the velocity, and γ the Lorentz factor defined by [14] [28]:

$$\gamma = \frac{1}{\sqrt{1 - \frac{v^2}{c^2}}} = \frac{1}{\sqrt{1 - \beta^2}} = \frac{E}{m_0 c^2} \tag{3.4}$$

For a single collision, the maximum energy that can be transferred from a heavy charged particle of mass m_0 with kinetic energy E_{kin} to an electron of mass m_{e} is given by [28]:

$$E_{\mathrm{kin}}^{\max} = \frac{2m_e p^2}{m_0^2 + m_e^2 + 2m_e E_{\mathrm{tot}}/c^2} \tag{3.5}$$

The kinetic energy is related to the total energy E_{tot} according to [28]:

$$E_{\mathrm{kin}} = E_{\mathrm{tot}} - m_0 c^2 = c\sqrt{p^2 + m_0^2 c^2} - m_0 c^2 \tag{3.6}$$

For low energy HCPs with $m_0 > m_e$, Eq. (3.5) can be approximated by [28]:

$$E_{\mathrm{kin}}^{\max} \approx 2m_e c^2 \beta^2 \gamma^2 \approx \frac{4E_{\mathrm{kin}} m_e}{m_0} \tag{3.7}$$

In the relativistic case, where $E_{\mathrm{tot}} \approx E_{\mathrm{kin}}$ and $pc \approx E_{\mathrm{tot}}$, the maximum energy that is transferable is then given by [28]:

$$E^{\max} = \frac{E_{\mathrm{tot}}^2}{E_{\mathrm{tot}} + m_0^2 c^2/2m_e} \tag{3.8}$$

The very high ionizing power of heavy ions greatly contribute to quenching effects in organic scintillators [1], in which the excitation is degraded mainly to heat and other non-radiative modes of de-excitation. As a result, only a fraction of the total amount of energy absorbed during excitation is converted into detectable scintillation light leading to a significantly reduced light output [8]. For example, a proton with equal energy to that of an electron will produce ~25% to 50% of the light yield of an electron, while for alphas the light yield is merely ~10% of that of electrons with the same energy [1]. Organic scintillators are not considered as an ideal detector for heavy ions due to the strong non-linearities in the detector response commonly found. For detection of heavy ions, a better light yield ($\sim 50\% - 70\%$) and linearity can be obtained with inorganic scintillators [1]. Thus, a thin layer of inorganic crystal is practically employed together with organic scintillators for the purpose of pulse shape

discrimination between fast signals produced by betas and gammas and slow components caused by alphas. The light yield per path length can be expressed as a linear function of the stopping power for a particle traversing a scintillator with low stopping power, at which quenching effects are assumed to be absent:

$$\frac{dL}{dx} = S\frac{dE}{dx} \tag{3.9}$$

where L is the light yield, S is the scintillation efficiency, dE/dx the stopping power. This relation is no longer linear at high stopping power due to recombination and quenching effects of the excited molecules. Therefore, the light yield can be described by the Birks' law that accounts for the probability of quenching [8]:

$$\frac{dL}{dx} = S\frac{\frac{dE}{dx}}{1 + k_B\frac{dE}{dx}} \tag{3.10}$$

where k_B is Birks' constant which varies depending on the material. For PVT-based scintillator, $k_B \sim 1.26 - 2.07 \cdot 10^{-2}$ g/(MeVcm^2) [29]. The linear stopping power (also termed the specific energy loss, in MeV/cm) S_{lin} (not to be confused with the scintillation efficiency S) of a charged particle traversing the absorber material, is defined as the differential energy loss divided by the corresponding differential path length [8]:

$$S_{lin} = -\frac{dE}{dx} \tag{3.11}$$

The specific energy loss is statistical since the details of the microscopic interactions undergone by any specific particle vary randomly [8]. However, for very heavy particles, such as α particle or heavier nuclei with charge Ze, moving at velocity v, the mean energy loss can be reasonably determined by Bohr's classical formula:

$$-\frac{dE}{dx} = \frac{4\pi Z^2 e^4}{m_e v^2} N_e \ln\frac{\gamma^2 m v^3}{Ze^2\bar{\nu}} \tag{3.12}$$

in which N_e is the electron number density of the absorber of atomic number Z, mass number A, and density ρ, which can be obtained by Eq. (3.13), $\bar{\nu}$ is the mean orbital frequency of the electrons bound to the atoms [1].

$$N_e = \frac{N_A Z \rho}{A m_u} \tag{3.13}$$

where N_A is the Avogadro number, m_u is the Molar mass constant. This classical calculation with Eq. (3.12) is no longer valid for lighter particles such as proton, due to quantum effects. The quantum-mechanically correct calculation of the energy loss rate of an HCP can be done with the Bethe-Bloch formula [28]:

$$-\frac{dE}{dx} = 4\pi N_A r_e^2 m_e c^2 z^2 \frac{Z}{A}\frac{1}{\beta^2}\left(\ln\frac{2m_e c^2\gamma^2\beta^2}{I} - \beta^2 - \frac{\delta}{2}\right) \tag{3.14}$$

The energy loss is sometimes of primary interests in nuclear and particle physics, i.e. for particle identification. Based on the particle mass dependence of the energy loss as a function of momentum $p = mc\beta\gamma$, by measuring the particle momentum from the deflection in a magnetic field and the energy loss, the mass of the particle, i.e. particle ID can be determined for certain energy range [30].

In Eq. (3.14), r_e is the classical electron radius ($r_e = \frac{1}{4\pi\varepsilon_0}\cdot\frac{e^2}{m_e c^2}$), I represents the mean excitation and ionization potential, characteristic of the absorber material, which can be approximated by

$$\begin{cases} I = 12Z + 7\ (\text{eV}), & \text{for } Z < 13 \\ I = 9.76Z + 58.8Z^{-1.19}\ (\text{eV}), & \text{for } Z \geq 13 \end{cases} \tag{3.15}$$

Frequently for substances containing mixtures and/or compounds, the atomic number cannot be precisely described by the sum of atomic numbers of all elements involved but is defined by the effective atomic number Z_{eff} [31].

$$Z_{\text{eff}} = \sqrt[2.94]{f_1 \cdot (Z_1)^{2.94} + f_2 \cdot (Z_2)^{2.94} + f_3 \cdot (Z_3)^{2.94} + \cdots} \tag{3.16}$$

where f_n is the fraction of the total number of electrons associated with each element, Z_n is the atomic number of each element. For PVT-based plastic scintillators, the molecular formula can be regarded as (C_9H_{10}). The total number of electrons is 64, of which 54 electrons come from carbon atoms and 10 from hydrogen. Then the effective atomic number for the scintillator in question is obtained by

$$Z_{\text{eff}} = \sqrt[2.94]{\frac{54}{64} \cdot 6^{2.94} + \frac{10}{64} \cdot 1^{2.94}} \approx 5.66$$

Therefore, the mean excitation potential for the plastic scintillator can be estimated according to Eq. (3.15):

$$I_{\text{sci}} = 12 \cdot 5.66 + 7\ (\text{eV}) = 74.92\ \text{eV}.$$

The term δ in Eq. (3.14) is the density correction to the Bethe-Bloch formula. The density effect arises from the phenomenon that the electric field of the particle tends to polarize the atoms along its passage. As a result, electrons distant from the path of the particle will be screened from the full electric field intensity. The contribution of collisions with these outer lying electrons to the total energy loss is therefore less than predicted by the Bethe-Bloch formula. This effect becomes more significant at higher incident particle energy. This effect also depends on the density of the material since the induced polarization will be stronger in denser materials than in lighter substances [1]. δ is a measure which describes how much the extended electric field of incident relativistic particles is shielded by the charge density of the atomic electrons [28].

The Bethe-Bloch formula implies a relation $-\frac{dE}{dx} \propto z^2$, which means that, for different charged particles of the same velocity, the stopping power increases

with the increase of charge. The trend of stopping power with respect to energy of different charged particles can be seen in Figure 3.5.

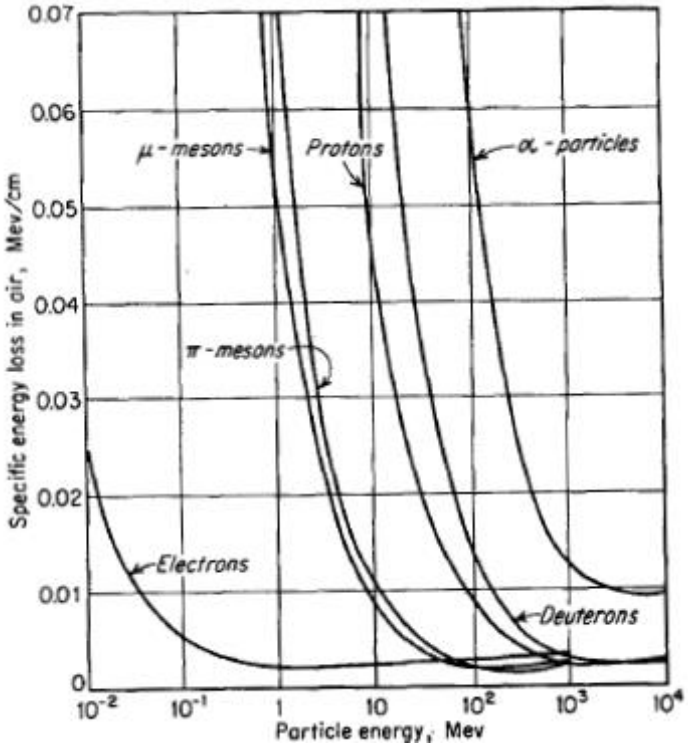

Figure 3.5: Variation of the stopping power in air versus energy of different charged particles [8].

The curve for each type of particle approaches a broad minima, where the value of dE/dx becomes nearly constant when the velocity of the particles approaches the velocity of light. For solid materials of low Z and ρ, this specific energy loss is around $\sim 1 - \frac{2\text{MeVg}}{\text{cm}^2}$, i.e. for a material with $\rho = 1\,\text{g/cm}^3$, $dE/dx = 1 - 2\,\text{MeV/cm}$. The charged particles that cause minimum ionization are termed minimum ionization particles (MIP), which are characterized by $\beta\gamma \cong 3.5$ over a wide range of absorbing mediums at the broad minima. This is adequately illustrated in Figure 3.6. Due to the different charge and mass, the dependencies of energy loss on the momentum are also shown for different types of particle. $p_\mu \sim 0.35\ \text{GeV}/c$, $p_\pi \sim 0.45\ \text{GeV}/c$, and $P_p \sim 3.5\ \text{GeV}/c$ correspond to minimum ionization [32].

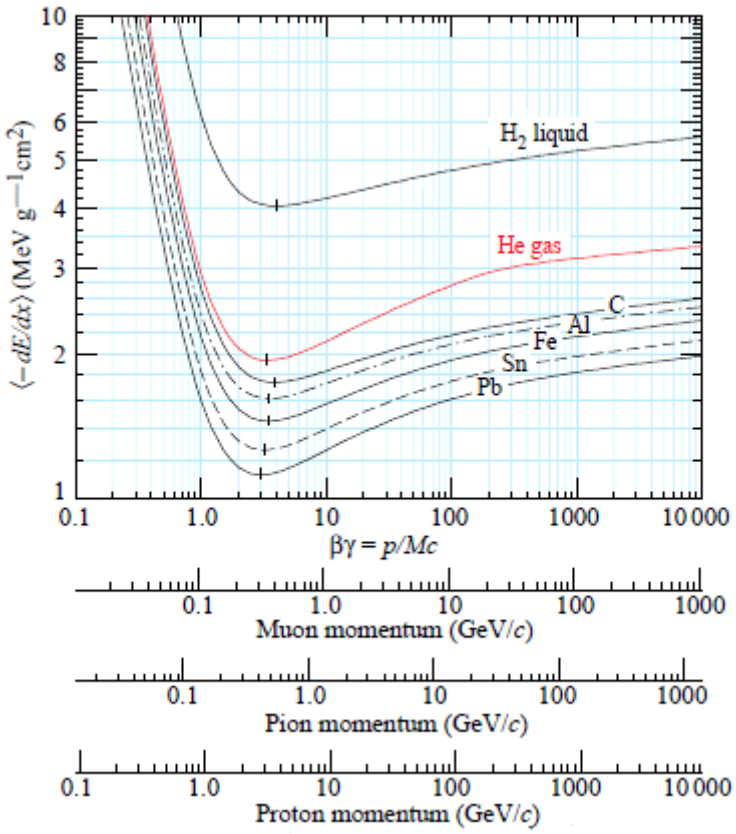

Figure 3.6: Mean energy loss rate in different mediums with corresponding momenta of muons, pions, and protons [32].

The specific energy loss is also path length dependent within the medium, the electric charge of the particle is reduced along its passage through the medium due to electron pickup, as described by the Bragg curve of an α particle in Figure 3.7.

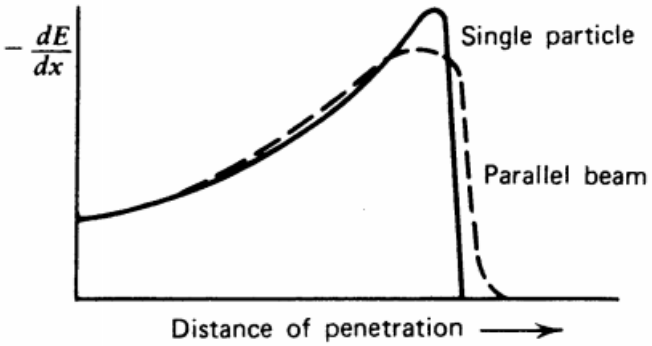

Figure 3.7: The Bragg curve of a 5.5 MeV α particle in air, with Bragg peak at path length ~3.8 cm [8].

The specific energy loss increases roughly as $1/E$ until a peak known as the Bragg peak arises, where the charged particle has greatest energy deposit in the material, then the curve suddenly drops. For a beam of particles, the Bragg peak is smoothened due to energy straggling. Due to this behaviour of the energy loss curve, charged particles are hence characterized by a definite range in a given absorber medium, which can be calculated from

$$R(T_0) = \int_0^{T_0} \left(\frac{dE}{dx}\right)^{-1} dE \tag{3.17}$$

As depicted in Figure 3.8, for the particles penetrating in silicon for example, the maximum range of the projectile particles shows a strong linearity with the energy in the log – log plot.

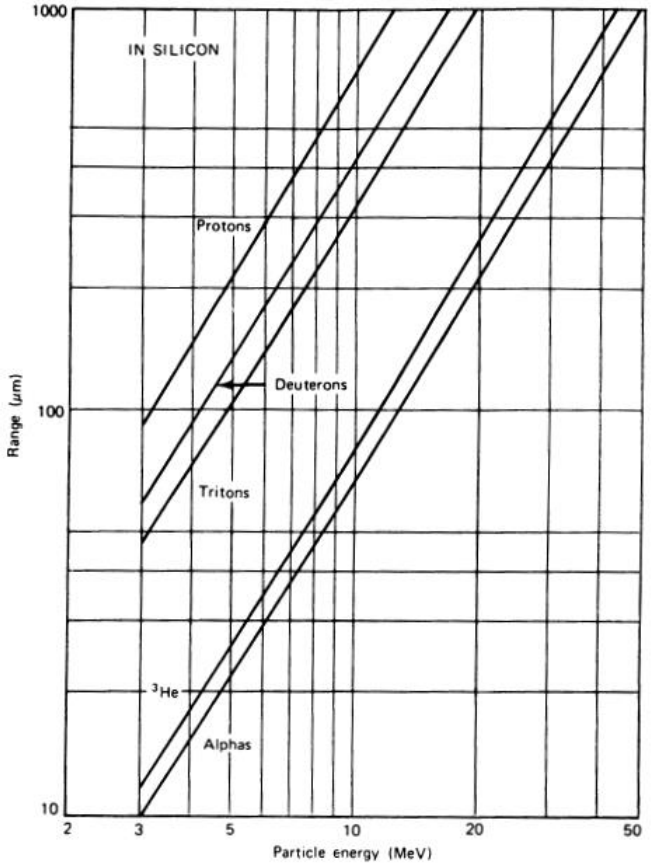

Figure 3.8: Range versus energy log-log plot for a few HCP over energy range 2 − 50 MeV, which suggests an empirical energy-range relation $R = aE^b$ [8].

The stopping time T, defined as the time required to stop a charged particle in an absorbing material, depends on the initial velocity v and range R. The initial velocity of non-relativistic particles can be deduced from its initial energy,

$$v = \sqrt{\frac{2E}{m}} = c\sqrt{\frac{2E}{mc^2}} = \left(3.00 \cdot 10^8 \frac{\mathrm{m}}{\mathrm{s}}\right)\sqrt{\frac{2E}{(931\mathrm{MeV/amu})m_A}} \tag{3.18}$$

where m_A is the particle mass in atomic mass units. With the assumption that the particle velocity can be averaged as $\langle v\rangle = Kv$, then T can be calculated as [8]

$$T = \frac{R}{\langle v\rangle} = \frac{R}{K(3.00 \cdot 10^8\ \mathrm{m/s})}\sqrt{\frac{m_A}{E}\cdot\frac{931\ \mathrm{MeV/amu}}{2}} \tag{3.19}$$

3.3 Interaction with beta particles

Differing from heavy charged particles, electrons may lose their energy by Coulomb interactions as well as radiative processes when passing through matter. Since the incident and target electrons have the same mass m_e, the scattering undergone by the incident β particles are more complicated, and the energies are deposited in the absorber at a lower rate compared to HCPs [1] [8]. Low-energy β particles interact with matter and lose the energy primarily by ionization. Ionization energy loss rates increase logarithmically with energy ($-\langle dE/dx\rangle_{Ionization} \propto \ln E$), whereas radiative energy losses rise nearly linearly ($-\langle dE/dx\rangle_{Bre} \propto E/m^2$) and dominate above the critical energy of a few tens of MeV in most materials. The radiative energy loss, known as Bremsstrahlung, is the emission of electromagnetic radiation arising from rapid acceleration or deceleration of the β particles in the electric field of a nucleus [32]. Therefore, the total linear stopping power of β particles is composed of two parts:

$$\left(\frac{dE}{dx}\right)_{tot} = \left(\frac{dE}{dx}\right)_c + \left(\frac{dE}{dx}\right)_r \tag{3.20}$$

Unlike the HCPs, the maximum transferable energy with β particles now becomes $E_{kin}^{\max} = E_{\mathrm{kin}}/2$. Due to the identical mass of the incident and target

electrons, the assumption that the incident particle remains undeflected during the collision process is no longer valid. The Bethe-Bloch formula is hence modified to describe the collisional energy loss of β particles [1]:

$$-\left(\frac{dE}{dx}\right)_c = 2\pi N_A r_e^2 m_e c^2 \rho \frac{Z}{A}\frac{1}{\beta^2}\left[\ln\frac{\tau^2(\tau+2)}{2(I/m_e c^2)^2} + F(\tau) - \delta - 2\frac{C}{Z}\right] \tag{3.21}$$

where τ is the kinetic energy of the particle in units of $m_e c^2$, and

$$F(\tau) = \begin{cases} 1-\beta^2 + \dfrac{\frac{\tau^2}{8} - (2r+1)\ln 2}{(\tau+1)^2}, & \text{for } e^- \\ 2\ln 2 - \dfrac{\beta^2}{12}\left(23 + \dfrac{14}{\tau+2} + \dfrac{10}{(\tau+2)^2} + \dfrac{4}{(\tau+2)^3}\right), & \text{for } e^+ \end{cases} \tag{3.22}$$

From classical theory, any charged particle must radiate energy in the form of electromagnetic radiation when accelerated or decelerated [8]. In the case of Bremsstrahlung, the linear energy loss rate through such radiative process is then given by [8]:

$$-\left(\frac{dE}{dx}\right)_r = \frac{NEZ(Z+1)e^4}{137 m_e^2 c^4}\left(4\ln\frac{2E}{m_e c^2} - \frac{4}{3}\right) \tag{3.23}$$

with N and Z representing the number density and atomic number of the absorber material, respectively. For the particle types and relevant energy ranges in this context, only fast electrons may have a significant yield of bremsstrahlung photons [8]. It is also described by Eq. (3.23) that, radiative losses are more likely for high electron energies and large Z absorber materials. For typical electron energies in practice, the average bremsstrahlung photon energy is quite low and is usually reabsorbed rather close to its point of origin. However, the escape of bremsstrahlung sometimes can affect the response of small detectors [1]. The ratio of the radiative specific energy loss to that from collisions can be approximated as [8]:

$$\frac{(dE/dx)_r}{(dE/dx)_c} \cong \frac{E \cdot Z}{700} \tag{3.24}$$

For a particular absorber material of atomic number Z, the critical energy E_c for $\left(\frac{dE}{dx}\right)_r = \left(\frac{dE}{dx}\right)_c$ can be obtained by equating the fraction in Eq. (3.24) to one and solving for E. For example, $Z_{\text{eff}} \approx 5.66$ for the scintillator in question, which gives $E_c \sim 120$ MeV.

Another parameter that describes the radiative energy loss is the radiation length, characteristic of a material, which is defined as the mean distance X_0, over which the electron energy is reduced by a factor of $1/e$ by bremsstrahlung. This becomes useful when dealing with detector thickness in the units of the radiation length [28]. The radiation length is normally approximated as

$$X_0 = \frac{716.4A}{Z(Z+1)\ln\left(287/\sqrt{Z}\right)} \ (\text{g/cm}^2) \tag{3.25}$$

Since electrons are highly susceptible to multiple scattering along the path through matter, the scattering undergone by electrons can be at large angles and sometimes backscattering is possible. There is a relatively larger variation in the electron range compared to that of HCPs, resulting in a statistical distribution of the electron range. However, the maximum range of a β particle travelling through a specific material can be approximated, for example, by the empirical formula reported by Katz and Penfold [33]:

$$R_{max}\ [\text{g/cm}^2] = \begin{cases} 0.412E_\beta^{1.265-0.0954\ln(E_\beta)}, & for\ 0.01 \le E_\beta \le 2.5\text{MeV} \\ 0.530E_\beta - 0.106, & for\ E_\beta > 2.5\text{MeV} \end{cases} \tag{3.26}$$

with the maximum β energy in MeV given by E_β. The tendency to stop betas depends primarily on the number of atomic electrons in the absorber, given as the number of electrons per cm^2. Therefore, the β range when expressed as a density thickness of the material in g/cm^2 provides a generic quantifier from which the maximum β range (in cm) in various materials can be calculated with the density ρ by

$$t = \frac{R_{\max}}{\rho} \tag{3.27}$$

Such energy-range relation shows the dependence of β range t on the β energy and material density, which is frequently of practical interest when estimating the thickness for required shielding and geometry of radiation detectors. For example, for a 5 MeV electron penetrating the EJ-248 scintillator which has a density of $\rho = 1.023\,\mathrm{g/cm^3}$, the maximum β range is calculated to be

$$R_{\max}\,[\mathrm{g/cm^2}] = 0.530 \times 5 - 0.106 = 2.544\,\mathrm{g/cm^2}$$

$$\Longrightarrow t = \frac{R_{\max}}{\rho} = \frac{2.544\,\mathrm{g/cm^2}}{1.023\,\mathrm{g/cm^3}} \approx 2.487\mathrm{cm}$$

The calculated maximum range is consistent with the graphical estimate obtained from the range-energy curves published by Eljen Technology, which allows extracting graphically the maximum range travelled by different particles through the plastic scintillator for comparison [34]:

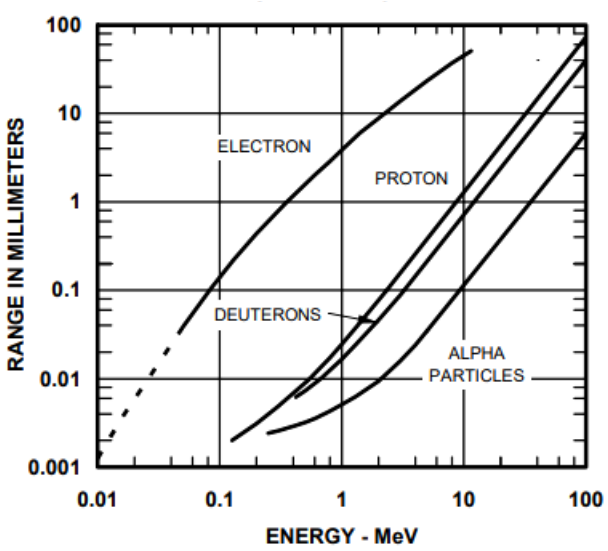

Figure 3.9: Particle ranges in plastic scintillator vs. particle energy [34].

This shows that, in order that the 5 MeV β particles are fully stopped, without penetrating through the scintillator, and the kinetic energy can be totally deposited in the scintillator, the scintillator must have a thickness no less than $\sim 2.5\mathrm{cm}$. Due to the small mass and interaction mechanism of β particles differing from that of HCPs, the light yield of β particles are much higher than that of HCPs of the same energy, as illustrated in Figure 3.10:

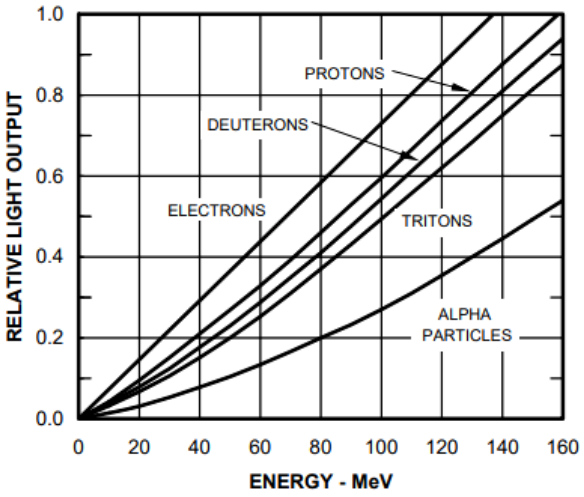

Figure 3.10: Response of a plastic scintillator material to atomic particles showing the light yields relative to each other [34].

Due to the continuous energy spectrum of β electrons, the absorption of β particles exhibits a behavior approximated by a near-exponential form, as expressed in Eq. (3.28). This effect is also described by the nearly linear curves plotted on a semi-logarithmic scale in Figure 3.11 [1] [8].

$$\frac{I}{I_0} = e^{-\mu t} \tag{3.28}$$

where I_0 is the counting rate without absorber, I is the counting rate with absorber, μ is β-absorption coefficient, and t is the absorber thickness in g/cm^2.

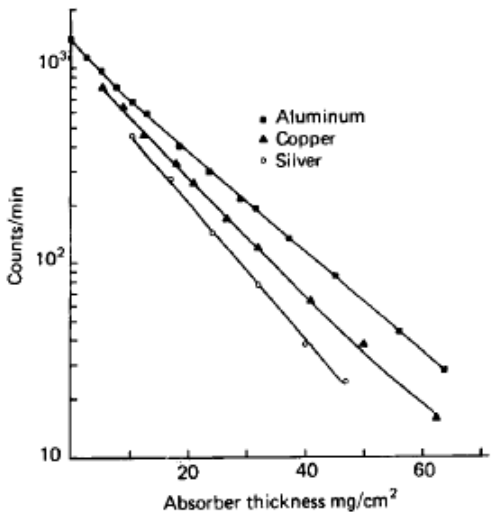

Figure 3.11: Absorption curves of different absorber materials for β decay electrons from ^{158}W with endpoint energy of 0.43 MeV [8].

The β detection efficiency is very high for most scintillators. However, due to the large angle scatterings and backscattering of the β electrons, there is always some probability that they escape from the detector, resulting in the kinetic energy partially deposited in the detector. Backscattering is most likely to occur with low-energy electrons and high Z absorbers [1]. Consequently, organic scintillators with a lower Z than inorganic crystals are most suitable for detection of low-energy (< 10 MeV) β particles. On the other hand, for high-energy electrons, due to the dominating bremsstrahlung at high energies, a higher-Z detector is more suitable for the detection of bremsstrahlung photon and other electromagnetic radiation induced.

3.4 Interaction with photons

Photons (X-rays and γ-rays) will traverse a certain distance undeflected until they interact with matter and deposit energy through any of the three major processes: Photoelectric absorption, Compton scattering, and Pair production. This is in clear contrast to the charged particles, which continuously undergo collisions and scatterings with the atomic electrons in the absorber and deposit energy along their path through matter.

3.4.1 Interaction probability

For a collimated beam of photons, the probability for an interaction to occur is defined as the fraction of photons undergoing any interaction after traversing a distance x:

$$f = 1 - e^{-\mu x} \tag{3.29}$$

with μ being the linear absorption coefficient expressed in cm^{-1}, which consists of the components of the three types of interactions, the linear photoelectric coefficient τ, Compton linear attenuation coefficient σ, and pair production attenuation coefficient χ, such that

$$\mu = \tau + \sigma + \chi \tag{3.30}$$

Each term in Eq. (3.30) varies with photon energy and is material dependent. The absorption can be parameterized more generally by the mass attenuation coefficient μ/ρ, expressed in cm^2/g, which is related to the total cross section by

$$\frac{\mu}{\rho} = \frac{N_A}{A}\sigma_{\mathrm{tot}} \tag{3.31}$$

with N_A being the Avogadro number and A is the atomic weight of a given molecule, σ_{tot} is the total atomic cross-section in $\mathrm{cm}^2 \cdot \mathrm{atom}^{-1}$ [26]. For a compound or mixture of elements with weight fractions w_i, the mass attenuation coefficient is calculated by summing up the weighted mass attenuation coefficients as in Eq. (3.32).

$$\frac{\mu}{\rho} = \sum_i w_i \left(\frac{\mu}{\rho}\right)_i \tag{3.32}$$

The γ rays are also characterized by the mean free path that describes the average distance of passage in the absorber before an interaction takes place. The mean free path can be obtained from

$$\lambda = \frac{\int_0^\infty x e^{-\mu x} dx}{\int_0^\infty e^{-\mu x} dx} = \frac{1}{\mu} \tag{3.33}$$

3.4.2 Photoelectric absorption

For low energies ($100\ \mathrm{keV} \geq E_\gamma \geq ionization\ energy$) the photoelectric effect dominates and continues to effect up to ~ 2 MeV [8]. For γ-ray energies over a few hundred keV, the majority of the initial photon energy is transferred to the photoelectron [28].

$$\gamma + atom \longrightarrow atom^+ + e^-$$

Photon is massless, for momentum conservation principle, the photoelectric absorption of a photon cannot occur with free electrons, but with the atom as a

whole instead. Emission of photoelectrons primarily originates from the γ interacting with the K shell electrons, with a smaller fraction with L and M shells. In the photoelectric absorption of a photon carrying an energy $E_\gamma = hv$, the photoelectron is ejected with an energy equal to the photon energy less the electron binding energy E_b.

$$E_{e^-} = hv - E_b \tag{3.34}$$

After ejecting a photoelectron the resulting ionized absorber atom is created with a vacancy in its bound shell, which is subsequently filled by an electron from a higher level shell and/or by capture of a free electron. This transition follows the energy conservation by emission of either a characteristic X-ray or an Auger electron. Although in most cases such X-rays are reabsorbed through interactions with the ambient atoms, there is still a chance that some X-rays occasionally escape from the detector [8]. Since the Auger electron typically has a very short range in matter, its energy is deposited in the material.

The absorption of a photon of energy E_γ in the K shell counts for about 80% of the total cross section. The total photoelectric cross section in the non-relativistic energy range $hv \ll m_e c^2$ can be obtained by the simplified Born approximation as

$$\sigma_{\text{pho}}^{K} = 4\pi r_e^2 Z^n \alpha^4 \cdot \frac{1}{\gamma} \tag{3.35}$$

where $\alpha = 1/137$ is the fine structure constant, $\gamma = E_\gamma / m_e c^2$ is the reduced photon energy in terms of the electron rest mass, n varies between 4 and 5 for the energy range $0.1\text{MeV} \leq E_\gamma \leq 5\text{MeV}$ [28]. It can be seen from Eq. (3.35) that, the photoelectric absorption is more likely to occur in higher Z materials. The partial mass attenuation coefficient (in cm^2/g) caused by photoelectric absorption is approximated as

$$\frac{\tau}{\rho} = \frac{N_A}{A E_\gamma^p} C Z^n \tag{3.36}$$

with E_γ being the photon energy with the exponent p decreasing between 3 and 1 with increasing E_γ. C is a correction factor. Again, the value of n varies between 4 to 5 depending on the photon energy [26]. It is also implied by this relation that, the attenuation of γ-rays caused by photoelectric absorption in materials with higher Z is generally stronger, and hence results in a greater stopping power.

3.4.3 Compton scattering

In the medium range of energies ($E_\gamma \approx 1$MeV) the Compton effect by which incident photons are scattered off quasi-free atomic electrons dominates with the largest cross section [28].

$$\gamma + e^- \longrightarrow \gamma + e^-$$

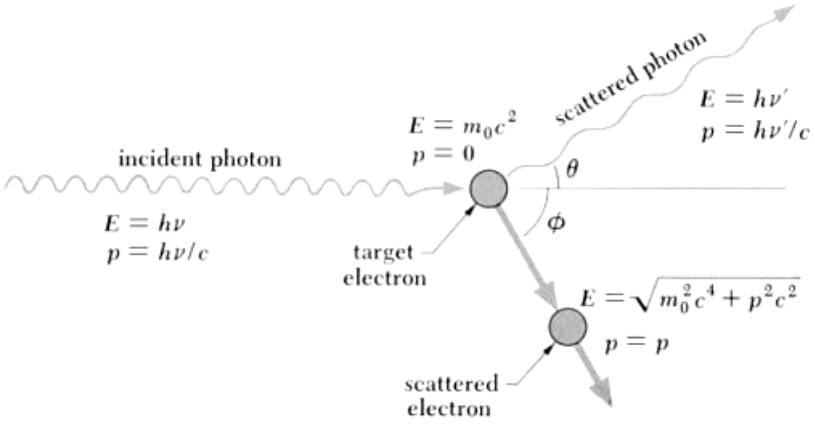

Figure 3.12: Kinematics of Compton scattering [35].

As illustrated in Figure 3.12, momentum and energy are conserved in the Compton scattering. The γ with initial energy $E_\gamma = h\nu$, after being Compton scattered at an angle θ, will have an energy E'_γ.

$$E'_\gamma = h\nu' = \frac{h\nu}{1 + \frac{h\nu}{m_e c^2}(1 - \cos\theta)} \tag{3.37}$$

where the electron rest mass $m_e c^2 \cong 0.511$MeV [8]. The energy of the scattered photon increases with decreasing θ. The kinetic energy transferred to the recoil electron is therefore

$$E_{e^-} = h\nu - h\nu' = h\nu\left(\frac{(h\nu/m_e c^2)(1-\cos\theta)}{1+(h\nu/m_e c^2)(1-\cos\theta)}\right) \tag{3.38}$$

As predicted by Eq. (3.37) and (3.38), there are two limiting cases of the energetics in Compton scattering. At an infinitesimal θ or $\theta \cong 0$, $h\nu' \cong h\nu$ and $E_{e^-} \cong 0$. On the other hand, for a head-on collision, in which $\theta = \pi$, the incident γ ray is backscattered to the direction opposite to its original path, whereas the electron recoils along the direction of incidence. In this case, the energy transferred to the electron in a single Compton interaction is maximized [8].

$$h\nu'\Big|_{\theta=\pi} = \frac{h\nu}{1+2\,h\nu/m_e c^2} \tag{3.39}$$

$$E_{e^-}\Big|_{\theta=\pi} = h\nu\left(\frac{2\,h\nu/m_e c^2}{1+2\,h\nu/m_e c^2}\right) \tag{3.40}$$

Normally, Compton scattering occurs at all angles in the detector giving rise to a continuum of electron energies called the Compton continuum, which ends at the Compton edge signifying the maximum energy of the electron Compton scattered at $\theta = \pi$.

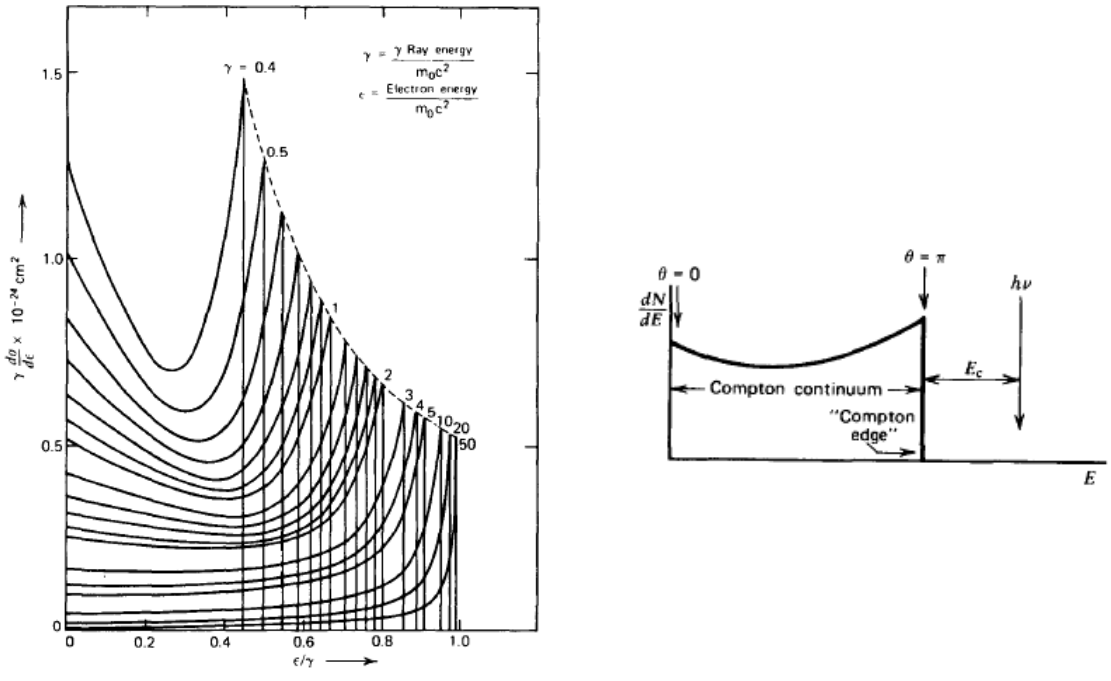

Figure 3.13: Compton continuum for different γ-ray energies [8].

However, the initial γ-ray energy is always partially transferred to the electron with a fraction of E_γ retained by the incident photon, even at $\theta = \pi$. This is well illustrated by the gap between the maximum recoil electron energy and the incident γ-ray energy in Figure 3.13. The energy difference is given by

$$E_C = hv - E_{e^-}\Big|_{\theta=\pi} = \frac{hv}{1 + 2\,hv/m_e c^2} \tag{3.41}$$

In the limiting condition that $hv \gg m_e c^2/2$, E_C tends to converge towards a constant value:

$$E_C\Big|_{E_\gamma \to \infty} \cong \frac{m_e c^2}{2} = 0.256\text{MeV} \tag{3.42}$$

The effect of the energy difference E_C in γ spectroscopy is a rounding off of the edge and a smooth bump instead of a sharp drop commonly observed in the measured spectrum.

The total cross section for a Compton scattering can be obtained by integrating the quantum electrodynamical expression of the Klein-Nishina formula in Eq. (3.43) over all angles to yield Eq. (3.44).

$$\frac{d\sigma_c}{d\Omega} = \frac{r_e^2}{2}\frac{1}{[1+\gamma(1-\cos\theta)]^2}\left(1 + cos^2\theta + \frac{\gamma^2(1-\cos\theta)^2}{1+\gamma(1-\cos\theta)}\right) \tag{3.43}$$

$$\sigma_c = 2\pi r_e^2\left\{\frac{1+\gamma}{\gamma^2}\left[\frac{2(1+\gamma)}{1+2\gamma} - \frac{1}{\gamma}\ln(1+2\gamma)\right] + \frac{1}{2\gamma}\ln(1+2\gamma) - \frac{1+3\gamma}{(1+2\gamma)^2}\right\} \tag{3.44}$$

Since the probability of a Compton scattering is related to the electron abundance in the absorber material, the contribution of Compton effect to the total mass attenuation coefficient can be deduced from Eq. (3.30) and (3.31).

$$\frac{\sigma}{\rho} = N_A\frac{Z}{A}\sigma_c \tag{3.45}$$

It is implied by this relation that, the influence on mass attenuation coefficient resulting from Compton effect does not depend on the material significantly as the ratio Z/A remains ~ 0.45 for all elements but hydrogen [24].

3.4.4 Pair production

Pair production is predominantly confined to high γ energies ($E_\gamma \gg 1\text{MeV}$). The γ ray carrying an energy beyond the threshold (1.02 MeV) is completely absorbed in the coulomb field of the nucleus and creates an electron-positron pair [8] [28].

$$\gamma + nucleus \longrightarrow e^+ + e^- + nucleus$$

The excess photon energy above the threshold is transferred into kinetic energy shared between the electron and positron.

$$E_\gamma = E_+ + m_e c^2 + E_- + m_e c^2 \tag{3.46}$$

with E_+ and E_- being the kinetic energies of the positron and electron, respectively.

When the nuclear charge is arbitrarily screened by atomic electrons, the pair production cross section for extreme relativistic energies is given by the Born approximation, based on which a general approximation of the pair production cross section can be obtained by an analytical integration of Eq. (3.47) [1].

$$d\sigma_{pair} = 4Z^2 r_e^2 \frac{1}{137}\frac{dE_+}{(h\nu)^3}\left\{(E_+^2 + E_-^2)\left[\frac{\phi_1(\xi)}{4} - \frac{1}{3}\ln Z - f(Z)\right]\right.$$

$$\left. + \frac{2}{3}E_+E_-\left[\frac{\phi_2(\xi)}{4} - \frac{1}{3}\ln Z - f(Z)\right]\right\} \tag{3.47}$$

where $\phi_1(\xi)$ and $\phi_2(\xi)$ are the screening functions depending on a screening-related parameter ξ and $f(Z)$ is a minor correction to the Born approximation, taking into account the interaction of the emitted electron in the Coulomb field of the nucleus. The calculation of pair production cross section simplifies in the limiting cases without screening and with complete screening. For low photon energies $1 \ll \gamma < 137/\sqrt[3]{Z}$, the photon must approach closely to the nucleus for

the pair production to occur without screening. In this case, the cross section can be obtained by

$$\sigma_{\text{pair}} = \frac{4}{137} Z^2 r_e^2 \left[\frac{7}{9} \left(\ln \frac{2hv}{m_e c^2} - f(Z) \right) - \frac{109}{54} \right] \tag{3.48}$$

In the case of complete screening of the nuclear charge, when $\gamma \gg 137/\sqrt[3]{Z}$,

$$\sigma_{\text{pair}} = \frac{4}{137} Z^2 r_e^2 \left[\frac{7}{9} \left(\ln \frac{183}{\sqrt[3]{Z}} - f(Z) \right) - \frac{1}{54} \right] \tag{3.49}$$

The component of mass attenuation coefficient χ/ρ originating from pair production is proportional to Z^2/A of the absorber medium [26]. For a specific material of Z^2/A and another material N of $(Z^2/A)_N$ and a known pair production mass attenuation coefficient $(\chi/\rho)_N$, the contribution of pair production to the total mass attenuation coefficient of the material in question is therefore obtained by

$$\frac{\chi}{\rho} = \left(\frac{\chi}{\rho} \right)_N \cdot \left(\frac{Z^2}{A} \right) \cdot \left(\frac{A}{Z^2} \right)_N \tag{3.50}$$

3.4.5 Gamma ray attenuation

The intensity (number of photons transmitted in unit time) of a γ ray of initial intensity I_0 after travelling through an absorber material of thickness t is attenuated by [8]:

$$\frac{I}{I_0} = e^{-\mu t} \tag{3.51}$$

where I is the intensity after the absorber, μ is the linear attenuation coefficient of the absorber material. And then, the thickness can be calculated by

$$t = \frac{\ln \frac{I}{I_0}}{-\mu} \tag{3.52}$$

This is frequently of practical interest when dealing with γ rays, in particular, with the thickness of shielding and the detector geometry. Generally, the linear

attenuation coefficient μ decreases as E_γ increases and increases with atomic number and density of the absorber. Due to the density dependence of μ, the mass attenuation coefficient is usually used for greater convenience [8].

3.5 Light collection and light guide

Two major types of loss of the scintillation light that may result in a degradation of the signal quality or pulse height are due to escape through the scintillator boundaries and through self-absorption by the scintillator material. The latter is more significant with large detectors, where the total path lengths travelled by the photons are comparable to the attenuation length l. The attenuation length is an intrinsic characteristic of the scintillator material defined as the path length of the photon after which the light intensity is reduced by a factor e^{-1}. The typical attenuation length for most scintillators is on the order of $\sim$ 1m [1]. The light intensity with initial value L_0 as a function of path length x is given by

$$L(x) = L_0 \exp\left(\frac{-x}{l}\right) \tag{3.53}$$

So far, the major loss of light is caused by transmission through the scintillator boundaries. Light emitted at a given point in the scintillator travels in all directions, besides a limited fraction that travels directly to the photosensor surface, most of the light photons will reach the scintillator boundaries at certain angle θ [8].

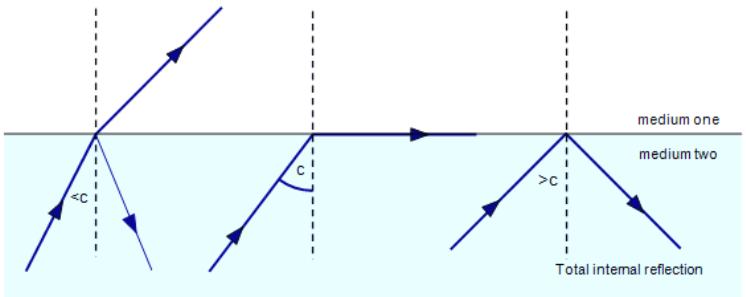

Figure 3.14: Schematic illustration of Fresnel reflection (left), critical angle of incidence (middle), and total internal reflection (right).

As illustrated in Figure 3.14, there is a critical angle θ_C of incidence, known as the Brewster angle. For light impinging at an angle less than θ_C, partial reflection called Fresnel reflection (See details in Section 7.1) and partial transmission through the boundary will occur. For $\theta > \theta_C$, total internal reflection (TIR) will occur [1]. The critical angle is defined by

$$\theta_C = \sin^{-1}\left(\frac{n_{\text{out}}}{n_{\text{scint}}}\right) \tag{3.54}$$

where n_{scint} and n_{out} are the refractive indices of the scintillator and the surrounding medium respectively. The efficiency and energy resolution of the detector can be significantly reduced by such transmissive loss. In addition, depending on the point of emission, different fractions of the total light output will be collected on the photocathode resulting in a non-uniformity in the pulse height response over the detector volume, in particular, with large detectors [1]. However, the efficiency of light collection can be improved by the usage of external reflective materials covering the scintillator. The light collection is demonstrated in Figure 3.15, for a simple detector setup in the cases with and without external reflectors.

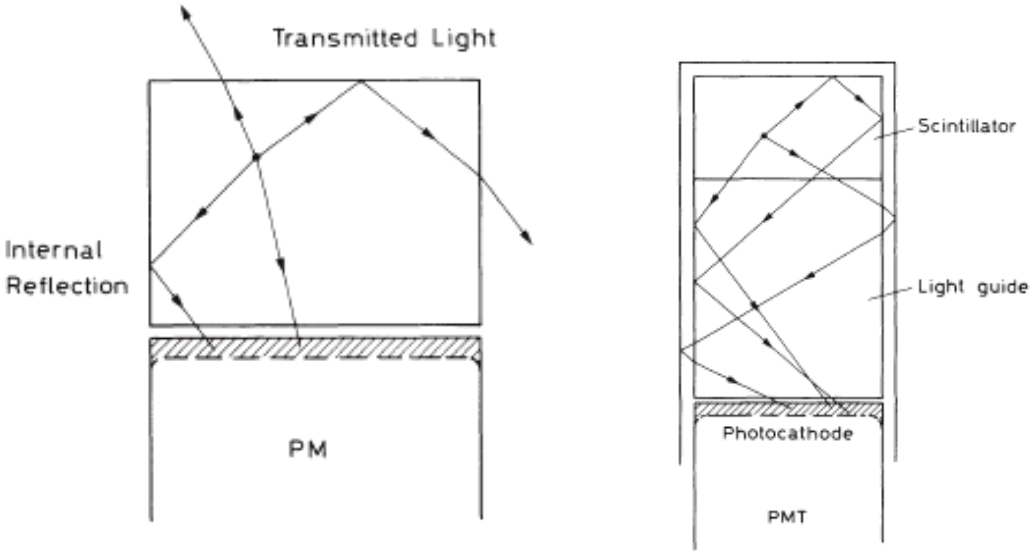

Figure 3.15: Example of light collection in a simple scintillator detector - scintillator without external reflector (left) and scintillator covered by reflector (right) [1].

As can be seen from Figure 3.15, without the reflective covering there is always a fraction of the scintillation light, which escapes the scintillator volume. On the other hand, escaping light is effectively redirected by the external reflection and conducted through a light guide onto the photosensor.

Some common issues in radiation detection such as space limitations, geometrical incompatibility between the scintillator and photosensor, etc., may make coupling the scintillator to the photosensor for light collection somewhat challenging. In such a situation, the scintillation light can be conducted through a light guide. For ease of discussion, the rectangular frustum light guide which is to be used in this project will be discussed as an example. A typical geometry of rectangular frustum light guide can be seen from Figure 6.1. When the input cross-sectional area is larger than the output ($A_i > A_o$), the light tends to be converged on the output plane. However, it has been proven by many studies, in particular, with phase space conservation that a given flux of light at the input can never be compressed into an output with smaller cross-sectional area due to reflections within the volume [1]. In practice, the fraction of light which is transmitted through a light guide is defined by

$$\frac{I_o}{I_i} \leq \frac{A_o}{A_i} \tag{3.55}$$

where I_i and I_o are the light intensities at the input and output, respectively. Therefore, the cross-sectional areas of the scintillator and light guide are of great concern when the light collection efficiency is taken into account. The optimal case in which $I_o/I_i = A_o/A_i$, is for a so-called *adiabatic* light guide which changes its shape gradually without sharp bends or kinks. An adiabatic light guide keeps the same cross-sectional area throughout and will conduct all the light down the guide [1]. The reflecting surface may be specular or diffuse. With a specular reflector, for example, aluminium foil, the reflections are mirror-like in the sense that the angle of reflection equals the angle of incidence. With a diffuse reflector which has a rougher surface than the specular reflector, such as TiO_2, the incident light is reflected in all direction. In some applications,

diffuse reflection in the scintillator change the light directions, contributing to reducing the light loss in the light guide, which consequently improve the transmission efficiency [36]. Diffuse reflections are essentially independent of the angle of incidence but follow Lambert's cosine law instead [1]:

$$\frac{dI}{d\theta} \propto \cos\theta \tag{3.56}$$

An investigation on the effects of different external reflectors and varying the lengths of light guide on the light collection of scintillators was provided by *Kilvington* et al. in 1970 and the data are summarized in Figure 3.15.

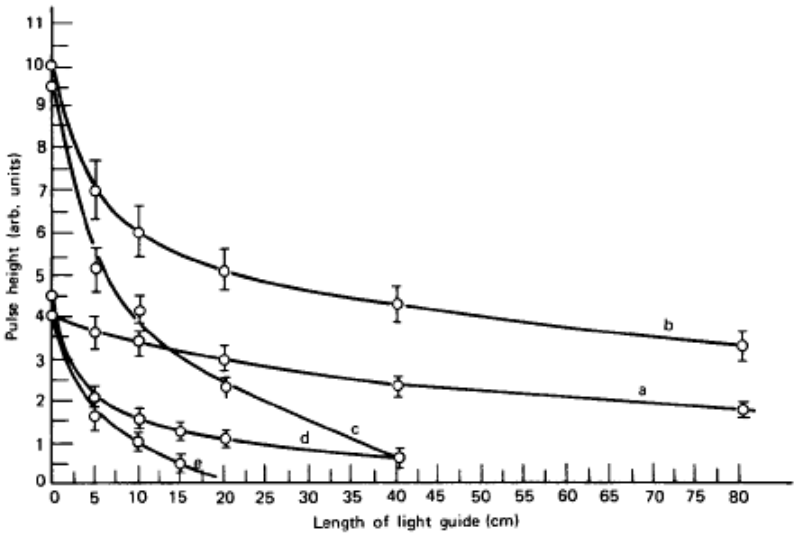

Figure 3.15: Effects of different reflection schemes and varying lengths of light guide on the light collection performance of a scintillation detector: (*a*). total internal reflection, without external reflector, (*b*). total internal reflection with external reflector, (*c*). light guide painted with diffuse reflector, (*d*). specular reflector without light guide, (*e*). diffuse reflector without light guide [1].

Obviously, the remarkable enhancement of light collection efficiency with the use of external reflector can be seen when comparing the pulse heights plotted in Curves (a) and (b). It also can be seen from Plots (c) and (e) that with the diffuse reflector, the pulse height is greatly enhanced by the usage of a light guide. A comparison of the effects caused by diffuse and specular reflectors on light collection can be extracted from comparing Plots (d) and (e). For small lengths (< 5 cm) of light guides, the difference is trivial, whereas specular

reflectors are more efficient in light collection with longer light guides. In addition, it is also described in Figure 3.15 that, for relatively short light guides (< 10 cm), light collection efficiency can be dramatically reduced by increasing lengths of light guide in any reflection schemes. However, this effect tends to vanish with longer light guides.

4. Silicon Photomultiplier

Silicon photomultiplier (SiPM) is a solid-state photodetector for detection of light in ultra-violet, visible, and infrared regions. SiPM is characterized by the excellent performance in sensing, timing, and quantifying low-intensity light signals with high single-photon detection sensitivity [37]. The device typically consists of a matrix of microcell (or pixel) of silicon p-n junction photodiode all connected in parallel, and a well-suited electronic circuit for signal output. The microcell density of a typical SiPM ranges between 100 and several 1000 per mm^2 [38]. Each microcell is a single-photon avalanche diode operating on a reverse-biasing voltage and coupled with a resistor for passive quenching [38]. The MICROFC-SMTPA-60035 SiPM produced by SensL, which has a sensor area of 6×6 mm^2 and microcell matrix of 60035: 18980 ($\approx$ 1.14 billion in total) was used in this project, as shown in Figure 4.1 [39].

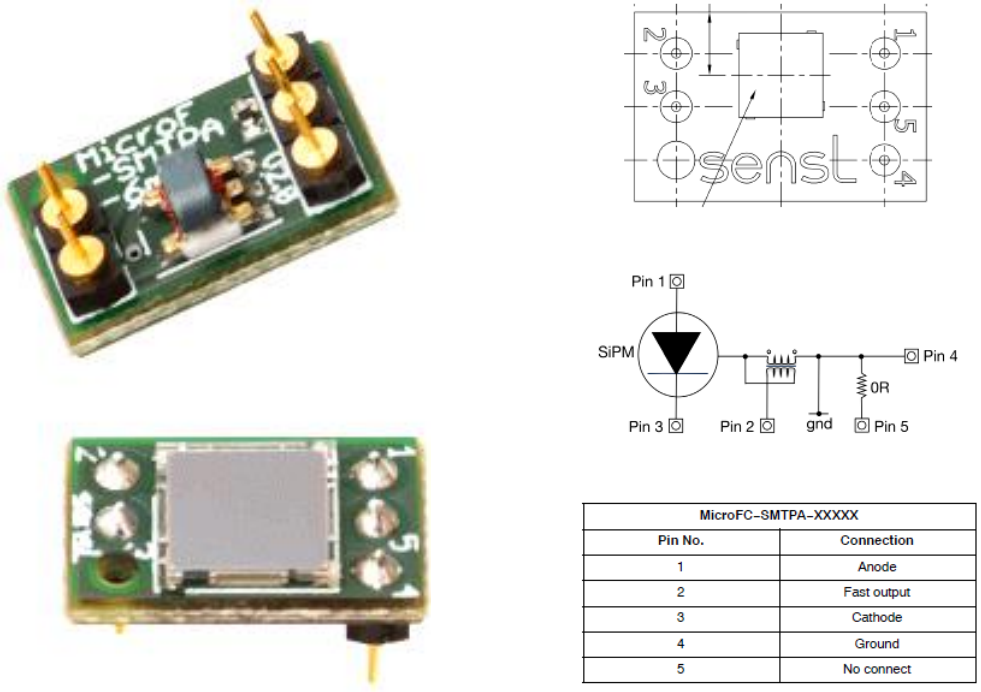

MicroFC-SMTPA-XXXXX	
Pin No.	Connection
1	Anode
2	Fast output
3	Cathode
4	Ground
5	No connect

Figure 4.1: The SensL MICROFC-SMTPA-60035 SiPM formed by a silicon substrate with photosensor active area 6mm × 6mm, the electronic circuit board with five pins (left); and the board circuit schematic with clarification of the labelling (right) [38].

4.1 The operation principles of SiPM

As a photodiode, the silicon p-n junction forms a depletion region, in which no mobile charge carriers are contained. Applying a reverse bias to the photodiode creates an electric field across the depletion region. When a photon is absorbed in silicon, the energy transferred in such absorption will move the electron from valence band into the conduction band, creating an electron-hole pair. The electric field across the depletion region will accelerate the electrons towards the cathode and the holes towards the anode, resulting in an induced photocurrent in a reverse-biased photodiode, as illustrated in Figure 4.2 [37].

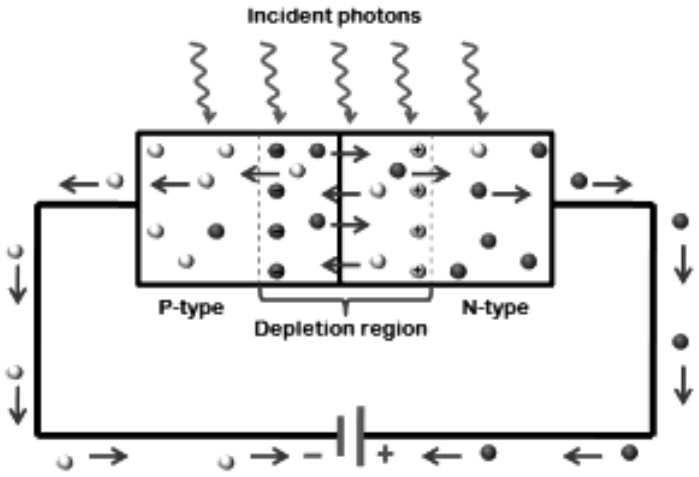

Figure 4.2: A schematic illustration of the photocurrent induced in the p-n junction photodiode [37].

Being dissimilar to metals, which have partially filled conduction bands or overlaps between the conduction and valance bands leading to relatively high conductivities, semiconductors are poor conductors under normal conditions. In semiconductors, the entirely filled valance band and the empty conduction band is separated by an energy gap E_g, which typically varies from 0.2 to a few eV depending on the material [40]. In order for the semiconductor photodiode to conduct electricity, sufficient energy must be supplied, such that the atomic electrons are excited from the valance band into the conduction band, either

thermally, or by exposure to energetic photons with energy $hv \geq E_g$. In order to convert the typical blue scintillation light with a wavelength of ~ 420 nm into an electric signal, sufficiently low band is required, which corresponds to a photon energy ~ 3 eV according to

$$E = \frac{hc}{\lambda} \tag{4.1}$$

Silicon with the band gap of 1.12 eV (~ 1110 nm equivalent) is particularly suited to detection of scintillation photons at room temperature. However, the band gap must not be too low in order to avoid high probability of thermally excited electrons, which would affect the single electron detection efficiency [42]. The number of electrons thermally excited from the valance band into the conduction band depends on the temperature, as shown in Eq. (4.2).

$$n_i = 2\left(\frac{2\pi m_e kT}{h^2}\right)^{3/2} \exp\left[\frac{E_g}{2kT}\right] \tag{4.2}$$

Silicon photodiodes cannot be used at room temperature for photons with $\lambda >$ 1110 nm. However, the band gap decreases as the temperature is increased and hence incident photons with longer wavelengths become detectable as well [40].

4.2 The Geiger mode behavior

The silicon photodiode is designated with recommended bias, such that a sufficiently high electric field ($> 5 \times 10^5$ V/cm) is generated within the depletion region. A charge carrier formed in between will be accelerated to a point where the sufficient kinetic energy carried by it will induce secondary charge pairs through a process called impact ionization. And therefore, a single absorbed photon can trigger a self-perpetuating ionization cascade spreading throughout the silicon volume subject to the electric field. Consequently, the silicon will break down and become conductive, with effective amplification of the original electron-hole pair into a macroscopic current flow with high gain. This process is known as Geiger discharge.

In the case of planar diode which has a finite thickness T as in SiPMs, under a bias voltage V that is not high enough, the diode slab is partially depleted to certain depth d [8]:

$$d = \left(\frac{2\epsilon V}{\rho}\right)^{1/2} \tag{4.3}$$

where ϵ is the dielectric constant of the medium, ρ is the charge density over the dielectric volume, which depends on the chemical doping of the silicon medium. For the diode to be ready to detect photons, full depletion requires a minimum applied voltage V_d (the *depletion voltage*) at which the depletion depth extends entirely across the slab thickness T [8]:

$$V_d = \frac{\rho T^2}{2\epsilon} \tag{4.4}$$

Typically, depending on the SiPM designs, the depletion voltage ranges from a few volts to several tens of volts below the breakdown voltage at which the silicon will break down and become conductive. As can be seen from the I-V characteristic curve of a typical diode illustrated in Figure 4.3, with the reverse bias voltage above a few volts and below the breakdown voltage, the diode stays fully depleted. The small current in the fully depleted diode is mainly dark current (See Section 4.3), which is a source of noise in SiPM operations. Above breakdown, the current increases by multiple orders of magnitude [41].

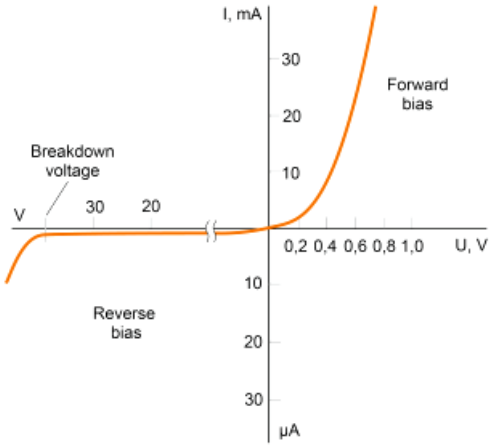

Figure 4.3: Current-voltage characteristic curve of a typical diode showing the current responses under forward and reverse biasing [41].

The breakdown voltage V_{br} is the minimum bias voltage that leads to Geiger discharge in the depletion region. An applied reverse bias above the nominal breakdown voltage will create the high-field gradients necessary across the junction. The induced current flow is then switched off by passive quenching, which can be achieved by using a series of quenching resistor R_Q. This instantly drops the reverse voltage to a value below the V_{br}, thus halting the avalanche. In this way, the diode recharges back to the bias voltage and is recovered for detection of subsequent photons. A simplified circuit schematic of the SensL SiPM is depicted in Figure 4.4 [37].

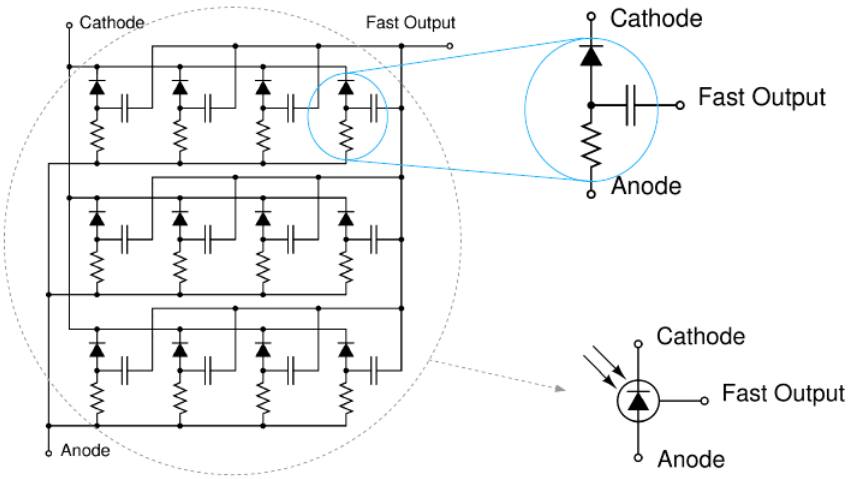

Figure 4.4: Simplified circuit schematic of the SensL SiPM showing an example of 12 microcells with schematic details of the components [37].

In addition, the Geiger mode has such behavior that, regardless of the number of photons absorbed within a diode simultaneously, the output signal produced is identical to that of a single photon. This effect consequently results in forbidden proportional information on the magnitude of an instantaneous photon flux. However, as illustrated in Figure 4.4, the SiPM is designed such that this limitation is offset by integrating a dense matrix of small independent Single Photon Avalanche Diodes (SPAD), with a quenching resistor coupled to each. And hence, proportionality in signal output is achieved by such microcells operating independently.

4.3 SiPM performance parameters

- ***Fill factor***

The fill factor F is defined as the percentage of the total surface area of the sensor that is sensitive to light. In view of the SiPM structure, each microcell is optically and electrically isolated from the neighbouring, leaving an inactive gap in between. In addition, some surface area needs to be reserved for the quenching resistor and signal tracks. All these result in an inactive space around each microcell. However, the separation between microcells and space required for the quenching resistor and signal tracking is somewhat constant, regardless of the dimension of the microcell. Consequently, larger microcells possess a higher percentage of the active surface area. Larger microcells with a higher fill factor result in greater photon detection efficiency (PDE) and gain, however, also in higher capacitances, longer recovery time, and lower dynamic range. On the contrary, smaller microcells with a lower fill factor result in lower PDE and gain, also in lower capacitances, shorter recovery time, and higher dynamic range [37].

- ***Breakdown voltage and overvoltage***

The bias voltage required for a typical SiPM is about $10\% - 25\%$ higher than the V_{br}. This excess voltage beyond the V_{br} is called the overvoltage.

$$V_{bia} = V_{br} + V_{ov} \tag{4.5}$$

In principle, the SiPM performance is improved by increasing the bias voltage within the recommended range. Increasing the voltage will enhance the electric field across the depletion region, and hence the photocurrent produced during the Geiger discharge. However, since the noise dramatically increases with V_{ov} and the detection efficiency tends to saturate with V_{ov}, the optimal bias voltage is governed by an upper limit. For the model used in this work, the V_{br} is designed to lie between 24.2 V and 24.7 V and the V_{ov} is recommended to be within $1.0\ \mathrm{V} - 5.0\ \mathrm{V}$ [37].

- ***Photon detection efficiency and responsivity***

The photon detection efficiency (PDE) is a measure of the detection sensitivity of a SiPM, defined as the statistical probability that an incident photon will be detected and generate a Geiger pulse from one of the microcells. The PDE is defined as the product of the SiPM characteristics and expressed as

$$PDE(\lambda, V) = Q_e(\lambda) \cdot \varepsilon(V) \cdot F \tag{4.6}$$

In Eq. (4.6), $Q_e(\lambda)$ is the quantum efficiency, which is defined as the probability of incident photons being absorbed and exciting an electron-hole pair, $\varepsilon(V)$ is the probability that an avalanche will be triggered by a charge carrier in the depletion region referred to as the avalanche initiation probability, and F is the fill factor [43].

The dependences of PDE on wavelength and bias voltage are well-illustrated in Figure 4.5 and 4.5, respectively.

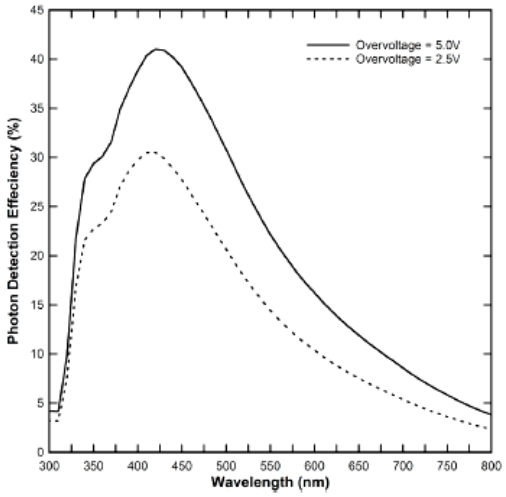

Figure 4.5: Wavelength dependence of PDE for V_{ov} of 2. 5 V and 5 V [37].

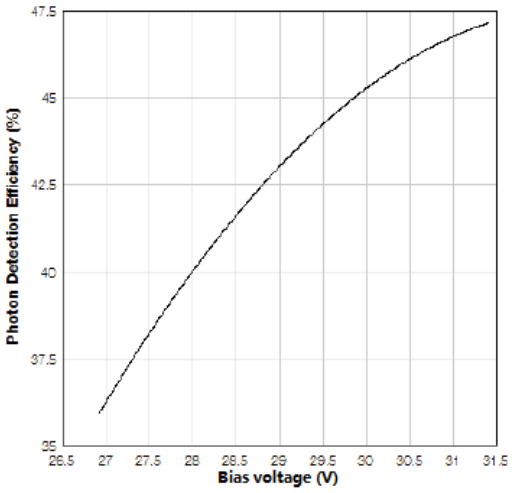

Figure 4.6: Voltage dependence of PDE at the peak wavelength [37].

It has been experimentally proven that, for most SiPM the maximum PDE is achieved at photon wavelength ~$420 - 450$ nm, as depicted in Figure 4.5. It can be seen from Figure 4.6, the PDE increases nearly linearly with bias voltage.

The slope of the curve drops smoothly as the PDE approaches saturation with increasing V_{ov}.

A factor that affects PDE is the responsivity, which is defined as the average photocurrent induced per unit optical power at a particular wavelength λ over the sensor area and is expressed in A/W by

$$R = \frac{I_p}{P_{op}} \tag{4.7}$$

The PDE can be determined with measured responsivity using the relation

$$PDE = \frac{R \cdot h \cdot c}{\lambda \cdot G \cdot e \cdot (1 + P_{AP}) \cdot (1 + P_{OC})} \cdot 100\% \tag{4.8}$$

where G is the gain, e is the elementary charge, P_{AP} and P_{OC} are afterpulsing and crosstalk probabilities respectively. Measurements of responsivity showed a similar wavelength dependence as that of PDE, as depicted in Figure 4.7.

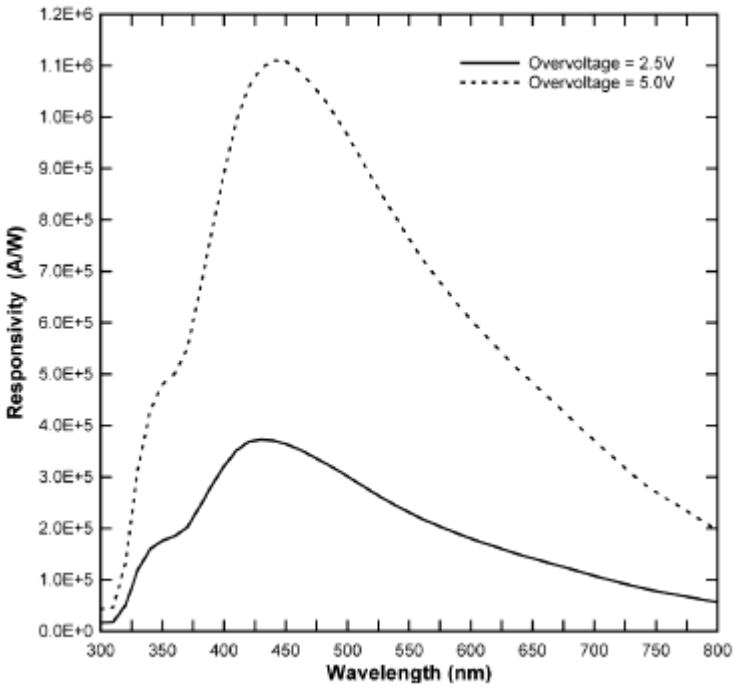

Figure 4.7: Wavelength dependence of R for a typical SiPM at overvoltages of 2.5 V and 5 V [37].

- ***Signal gain***

The gain of a SiPM is defined as the amount of charges created by each Geiger discharge caused by the detected photon, which depends on overvoltage and microcell dimensions. Each microcell in the sensor produces a highly uniform and quantized amount of charge when an avalanche is triggered by an absorbed photon in the active volume. The gain of a microcell and the resulting gain of the sensor is therefore defined as the ratio of the charge created in an activated microcell to the electron charge. The gain can be calculated from the overvoltage, the microcell capacitance C, and the electron charge q_e using the basic rule of electrodynamics:

$$G = \frac{C \cdot V_{ov}}{q_e} \tag{4.9}$$

- ***Noise mechanisms***

All operative electronic circuits are inevitably subject to noise. The noise in Geiger mode avalanche photodiode devices primarily results from the dark count rate (DCR) and other correlated noise sources, mainly comprised of optical crosstalk (OC) and afterpulsing (AP).

The dark count rate of a SiPM is an intrinsic limiting factor of the detector efficiency, defined as the counting rate of spurious output current pulses produced in absence of light. The origin of DCR is thermally generated charge carriers tunnelling into the high-field region and thus triggering Geiger discharge, which is thereby counted as signal [37]. Most SiPMs have a typical DCR of a few tens of kHz/mm^2 of the sensor area at room temperature. In practice, for continuous measurements implemented by current integration, it is frequently more convenient to consider this noise in the form of dark current, measured in μA. The dark current can be reported as a function of temperature, as described by Eq. (4.10):

$$I(T) = I(T_0)\frac{T^2}{T_0^2}\exp\left(-\frac{E_g}{2kT}\right)\Big/\exp\left(\frac{E_g}{2kT_0}\right) \tag{4.10}$$

with $E_g = 1.2$ eV being the band gap in silicon, k is the Boltzmann constant and T_0 is a reference temperature [44]. It can be predicted by Eq. (4.10) that the dark current doubles on a temperature raise of ~ 10℃, and therefore, the DCR can be halved by cooling the detector by 10℃. The temperature and bias voltage dependencies on dark current can be visualized in Figure 4.8. The magnitude of DCR scales according to the sensor area and increases as a function of V_{ov}. For a fixed sensor area, varying pixel size also affects to DCR as the smaller pixel size leads to a larger number of pixels to cover the sensor area, and hence forms a smaller active area (or fill factor), resulting in lower DCR.

Since the photon-induced and thermally-generated signals are identical, the false signal resulting from dark current causes the noise at the single photon level. However, this noise can be significantly filtered out by setting a threshold above the single photon level [37]. However, the fluctuating nature of the dark counts makes this noise indistinguishable from the measured signal. The effect of set threshold on DCR is illustrated in Figure 4.9.

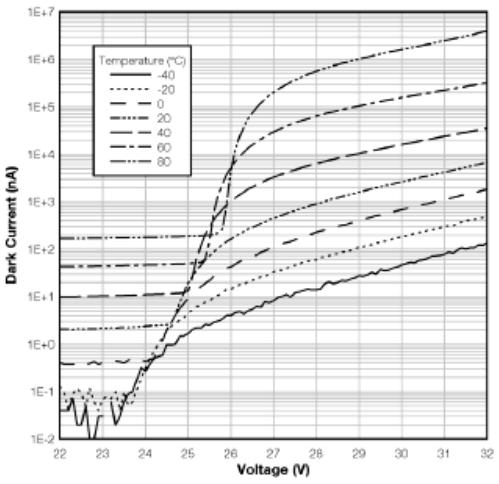

Figure 4.8: Temperature and voltage dependences of dark current [37].

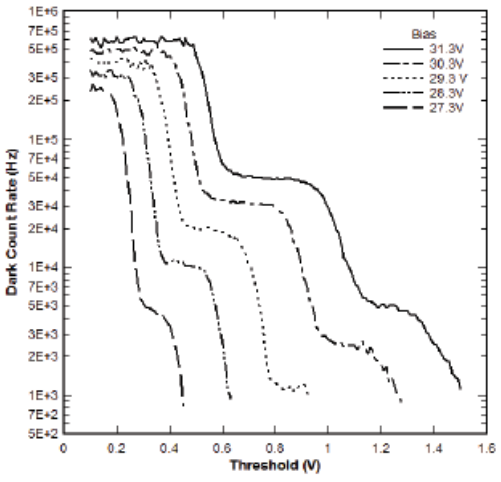

Figure 4.9: Effect of threshold on dark count rate at different V_{bia} values [37].

The phenomenon of optical crosstalk occasionally occurs when an energetic electron accelerated in the high-field region during an avalanche recombines with a hole and emit photons near infrared (NIR). This photon will travel to a

neighbouring microcell through either direct propagation or reflections from the boundary interfaces, and subsequently inducing a secondary avalanche therearound and thereby producing extra current signals. The crosstalk probability is defined as the probability that an avalanching microcell will induce a secondary avalanche in another microcell and is a function of SiPM overvoltage and the separation between neighbouring microcells. Typically, about 2×10^{-5} photons are emitted per electron crossing the junction [37].

Afterpulsing is a phenomenon in which a pulse generated in a microcell is swiftly followed by one another arising in absence of incident photon. The occurrence of AP has been attributed to the release of charge carriers being trapped in defects in silicon during the photon-induced avalanche, which potentially triggers another avalanche generating a delayed current pulse in the same microcell [37]. The number of afterpulse counts can be increased by a number of factors. An excessively long integration time will count a huge number of afterpulses. A greater density of traps can be caused by production defects. Larger pixel sizes will cover a larger volume of traps, resulting in increased number of counted afterpulses. The greater capacitance from larger pixels will result in more charge during each avalanche, which then fill more traps and cause more afterpulse events. The effective trap time constant is increased by colder temperatures, such that more afterpulsing will be recorded within a given time window. However, upon an integration time set on the order of the recharge time, afterpulsing may merely contribute to the low-energy background and typically with a rather low probability ($< 5\%$) [42].

Optical crosstalk and afterpulsing are classified as correlated noise, as the prompt crosstalk can subsequently produce an afterpulse or delayed crosstalk. These two components are undistinguishable at long delay time. However, afterpulses with delay times shorter than the pixel recovery time have lower amplitude. On the other hand, since crosstalk avalanches are not affected by the primary pixel recovery, they may have arbitrarily short delay time [45].

- *Dynamic range and linearity*

The dynamic range (DR) of a given SiPM sensor is defined as the optical signal range over which the sensor provides a useful signal output. In the limiting case that all the pixels are activated simultaneously, saturation of the output signal will occur, where no additional pixels are available to detect successive incident photons until some of the pixels recover to their initial states. Thus, the dynamic range is a function of the total number of pixels and the PDE. Since PDE is dependent on the overvoltage and wavelength of incident photon, the dynamic range of SiPM can be expressed as a function of the total number of pixels, the overvoltage, and wavelength:

$$N_{\text{act}}(M, V_{\text{ov}}, \lambda) = M\left[1 - \exp\left(-\frac{PDE(V_{\text{ov}}, \lambda) \cdot N_{\text{ph}}}{M}\right)\right] \tag{4.11}$$

where N_{act} is the number of activated pixels, M is total number of pixels, N_{ph} is the number of incident photons. For low photon fluxes relative to the number of pixels ($N_{\text{ph}} \ll M$), the SiPM has a linear response. As the number of incident photons increases, the response of the SiPM tends to saturate [37]. The SiPM response to incident power is depicted in Figure 4.10 and 4.10.

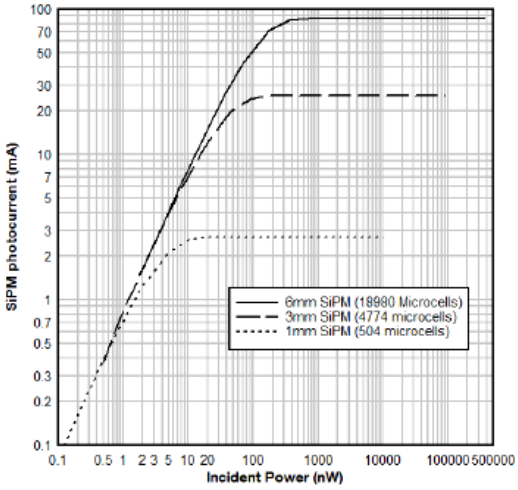

Figure 4.10: The SiPM photocurrent as a function of incident power on a log-log scale [37].

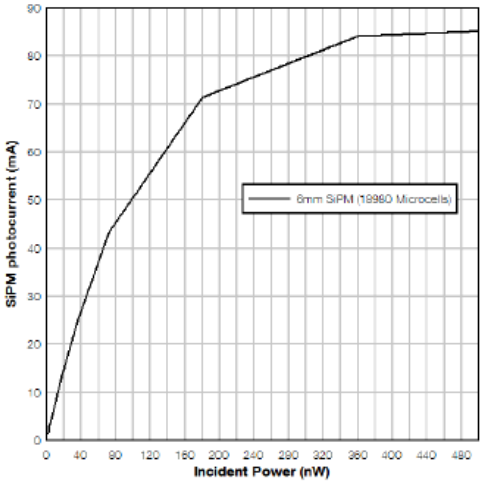

Figure 4.11: The SiPM photocurrent as a function of incident power on a linear scale [37].

As described by Figure 4.10, at low light signal level, a linearity is presented by the output photocurrent of SiPM increasing with incident light power. As the incident power increases, the output photocurrent starts to deviate from the linear response tendency and eventually approaches saturation due to the finite pixel number. Since a larger pixel number will result in a larger dynamic range, for a given sensor size, the dynamic range can be enhanced by smaller pixel sizes. It is a general rule of thumb to maintain a linearity in SiPM response by fitting the maximum expected power to ~70% of the SiPM range [37], as depicted in Figure 4.11. Detailed technical information of the MICROFC-SMTPA-60035 SiPM is available in Appendix B.

5. General detector characteristics

The performance of a radiation detection system is in general parameterized by several characteristics, which are usually of primary concerns in studies with nuclear spectroscopy. Some operative characteristics can be drawn from the measurement of energy spectrum.

5.1 Energy resolution

In the operation of a radiation detector in pulse mode, the pulse amplitude distribution is an essential property of the detector output that is routinely used to analyse information about the incident radiation or the performance of the detector itself. The pulse amplitude information is most commonly described by the differential pulse height distribution, as depicted by the hypothetical distribution in Figure 5.1.

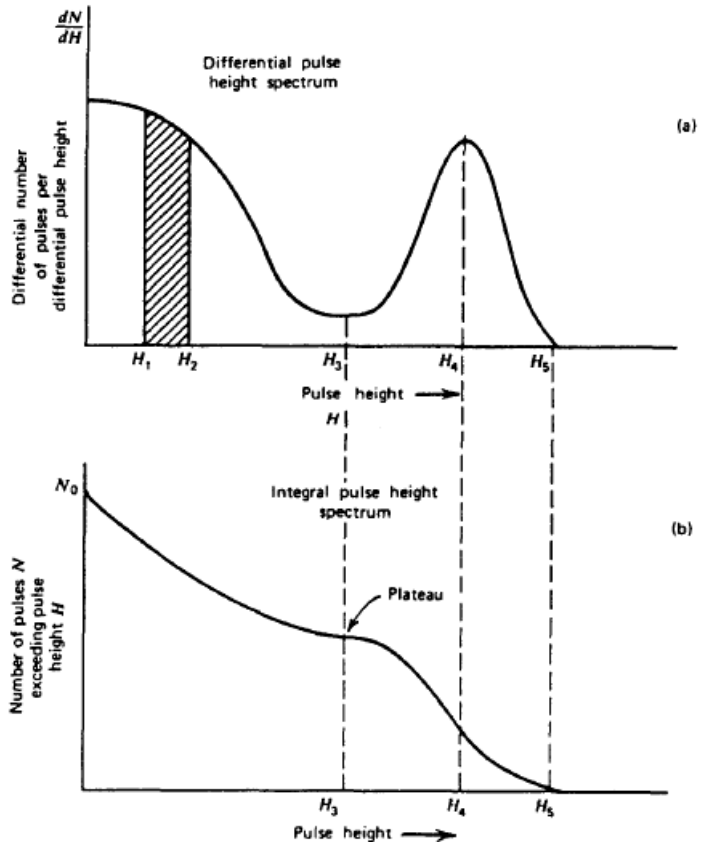

Figure 5.1: Differential and integral pulse height spectra for a hypothetical source of pulses [8].

The abscissa H denotes a linear pulse amplitude scale and the ordinate is defined as the differential number dN of pulses observed with an amplitude within the differential amplitude increment dH divided by the increment, or dN/dH. H has units of pulse amplitude (in volts) and dN/dH has units of inverse amplitude (volts^{-1}). The number of pulses with amplitude between two given values H_1 and H_2 can be obtained by

$$N_{1\to 2} = \int_{H_1}^{H_2} \frac{dN}{dH} dH \tag{5.1}$$

whereas the total number of pulses N_0 represented by the distribution can be determined by

$$N_0 = \int_0^{\infty} \frac{dN}{dH} dH \tag{5.2}$$

In fact, the differential and integral distributions convey exactly the same information and can be derived from each other [8].

Energy resolution R_e is the measure of the detector's sensitivity of response to monoenergetic source of radiation, which is defined referring to Figure 5.2, as the full width at half maximum (FWHM) divided by the channel number of the peak centroid H_0 [8]. The lower magnitude of R_e, the more accurately the detector may distinguish adjacent energy peaks.

$$R_e = \frac{FWHM}{H_0} \tag{5.3}$$

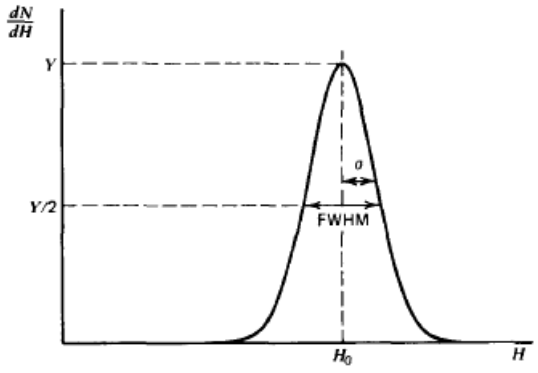

Figure 5.2: Definition of energy resolution of a detector in terms of FWHM [8].

In this context, the pulse amplitude distribution is reasonably assumed to have a Gaussian shape, where N is typically a large number.

5.2 Timing

As discussed in the previous chapters, both the scintillator and the SiPM are characterized by some timing properties in their responses to successive events. As a result, these timing components together contribute to an overall timing property of the scintillation detector, which is a pivotal parameter of the detector performance. Generally, the faster rise time and decay time are displayed, the more sensitive and accurate response a scintillation detector has. In addition, the timing properties of different scintillation materials may differ significantly depending on the type of radiation. Such materials can be used in combination for pulse determination applications. For example, a thin layer of ZnS(Ag) screen affixed on the front side of the plastic scintillator may provide exceedingly high intrinsic detection efficiency of α particles, while its sensitivity for β particles and γ rays is very low. This effect may ultimately facilitate techniques for distinguishing between different radiation types, i.e. pulse shape discrimination (PSD).

5.3 Half-value thickness

The half-value thickness, or half-value layer (HVL) $X_{1/2}$ for γ radiation is the thickness of the absorber material required to diminish an incident γ radiation to half of its initial intensity.

$$I(X_{1/2}) = \frac{1}{2} I_0 = I_0 e^{-\mu X_{1/2}} \tag{5.4}$$

The attenuation of incident radiation is described by Eq. (5.4), which yields

$$X_{1/2} = \frac{\ln 2}{\mu} \tag{5.5}$$

with μ being the linear attenuation coefficient of the absorber [46]. As discussed in Section 3.4, the mass attenuation coefficient μ_m is frequently used in practice for convenience instead of μ, thus, the half-value mass thickness $X_{m1/2}$ is more conveniently used and $X_{m1/2}$ is expressed by Eq. (5.6), accordingly.

$$X_{m1/2} = \frac{\ln 2}{\mu_m} \tag{5.6}$$

This concept is only for γ radiation as α and β radiations will be completely absorbed within the detector. In the recoil-β tagging experiment with MARA, the primary requirement is that, the scintillator must be thick enough, such that the β particles having energies up to 10 MeV after passing through the DSSD is fully stopped within the scintillator, where the remaining energy of the β particle is measured for identification.

Since the value of total attenuation coefficient is dependent on the material and photon energy, the half-value thickness is determined according to the energy of the γ rays of interests. Regarding the PVT-based scintillator, the values of mass attenuation coefficient μ/ρ and energy absorption coefficient μ_{en}/ρ of vinyl toluene-type plastic scintillator for a typical set of photon energies were adapted from [47] and presented in Appendix C.

5.4 Pulse shape discrimination

A historical development for simultaneous measurement and discrimination of α, β, and γ radiations was the phoswich detector designed by Usuda et al. In phoswich the α particles penetrate and interact only with thin (10 mg/cm^2) ZnS(Ag) scintillator, while the β particles and γ rays proceed to interact with a thicker plastic scintillator, where the β particles and low-energy γ rays are measured. In this measurement only the high-energy γ rays with higher penetrating power carry on to interact with the BGO scintillator. This phoswich detector was tested for discrimination of different types of radiation using

various sources. The sources used were ^{244}Cm for α particles, ^{90}Sr (^{90}Y) for β particles, ^{241}Am for both low-energy γ rays and α particles, and ^{137}Cs and ^{60}Co for β and γ counting. It was reported by Usuda et al. that ZnS(Ag) is favourably insensitive to β and γ radiation with relatively slow signal among popular scintillators [48]. The low-Z plastic scintillator has the highest sensitivity to β particles, with relatively fast signal among the scintillators and a relatively high energy resolution. The BGO scintillator with high Z and density showed a moderate timing characteristic and a high sensitivity to γ rays [48].

An alternative to ZnS(Ag) for detection of α-particles with similar slow timing property is the ZnS(Cu). However, the scintillation light emitted by ZnS(Ag) has a wavelength (blue) corresponding to the optimal PDE of the SiPM, while that emitted by ZnS(Cu) is green, which corresponds to a PDE ~ 50% relative to that of ZnS(Ag) [2].

The ZnS(Ag) is commercially available either in the form of white fluorescent powder or in thin flat plates. The powder can be mixed with a low-viscosity, optically transparent binder in a specific ratio to form a mixture, which can then be deposited uniformly on the desired surface of the scintillator. However, due to its opacity to its own luminescence, the thickness of this scintillator must be thin enough (typically < 1 mm) to produce detectable light in the cases of α particles and other heavy ions.

5.5 Detection efficiency

There are a number of factors that may influence the detection efficiency, such as the scintillation efficiency, stopping power of the detector, radiation energy to light conversion efficiency of the scintillator, the quantum efficiency, and band gap of the photosensor material, etc, as discussed in Section 4.1. However, in practice the overall detection efficiency can be generally represented by geometrical efficiency, Absolute efficiency, and Intrinsic efficiency [8].

- ***Geometrical efficiency***

For simplicity, only the case relevant to this project is discussed here, in which the radiation emitted over a spherical surface of 4π steradians by a point source is subtended by a rectangular face of the scintillator. For a rectangular surface with length a and width b at distance d from a point source facing the center of the rectangle, the solid angle Ω can be calculated by

$$\Omega = 4\cos^{-1}\sqrt{\frac{1+\alpha^2+\beta^2}{(1+\alpha^2)(1+\beta^2)}} \tag{5.7}$$

where $\alpha \equiv a/(2d)$ and $\beta \equiv b/(2d)$ [49]. And then, the geometrical efficiency ϵ_g in such 4π geometry is defined by Eq. (5.8) [50].

$$\epsilon_g = \frac{\Omega}{4\pi} \cdot 100\% \tag{5.8}$$

- ***Absolute efficiency and Intrinsic efficiency***

Determination of the absolute efficiency ϵ_{abs} and intrinsic efficiency ϵ_{int} of a detector is explained in [8] and given by

$$\epsilon_{\text{abs}} = \frac{number\ of\ events\ registered}{number\ of\ emitted\ gamma\ quanta} \tag{5.9}$$

$$\epsilon_{\text{int}} = \frac{number\ of\ events\ registered}{number\ of\ emitted\ quanta\ incident\ on\ detector} \tag{5.10}$$

6. Designs and Measurements

6.1 Designs and Preparations

The raw EJ-248 plastic cylinder was machined into the predefined geometries and polished. As shown in Figure 6.1, three scintillators were prepared with the geometries specified in Table 6.1. The detailed drawings are available in Appendix D.

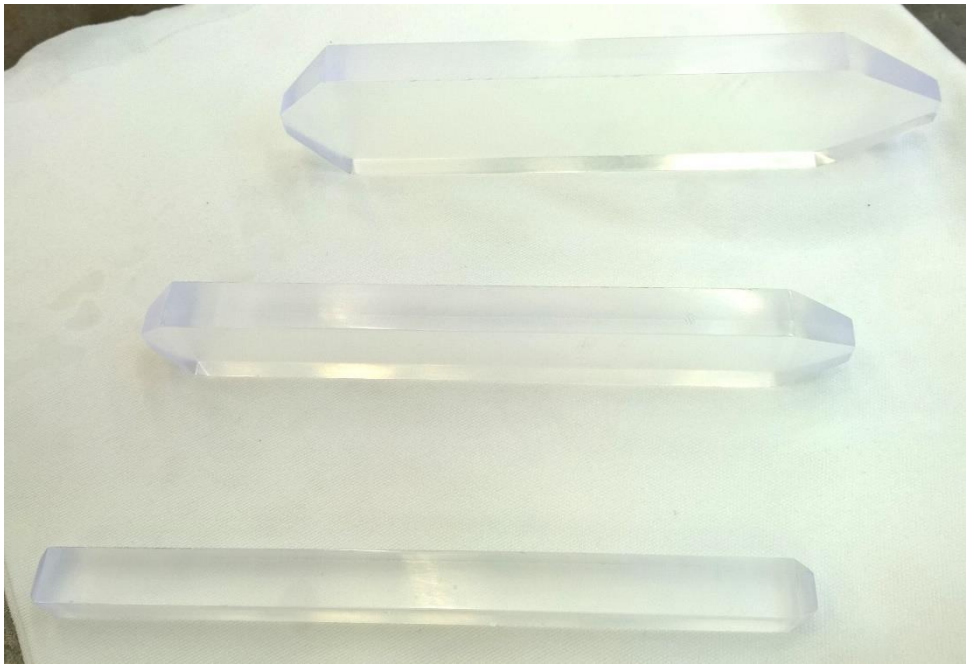

Figure 6.1: Three scintillators machined and polished from EJ-248 plastic cylinder.

Table 6.1: Geometrical specifications of the scintillators.

	Scintillator 1	Scintillator 2	Scintillator 3
Total length (mm)	128	128	128
Width (mm)	10	10	10
Frontal area (mm^2)	122.5 × 10	109 × 10	95.2 × 10
Light guide A	Acceptance angle 45°	Acceptance angle 45°	Acceptance angle 45°
	Transmission window (mm^2): 6 × 6		
Light guide B	Acceptance angle 60°	Acceptance angle 60°	Acceptance angle 60°
	Transmission window (mm^2): 6 × 6		

Since the use of optical cement at this stage was not applicable, coupling of the scintillators and the SiPMs was achieved with the aids of my designs of the assembling apparatuses and by using the optical grease which has a refractive index of ~ 1.5.

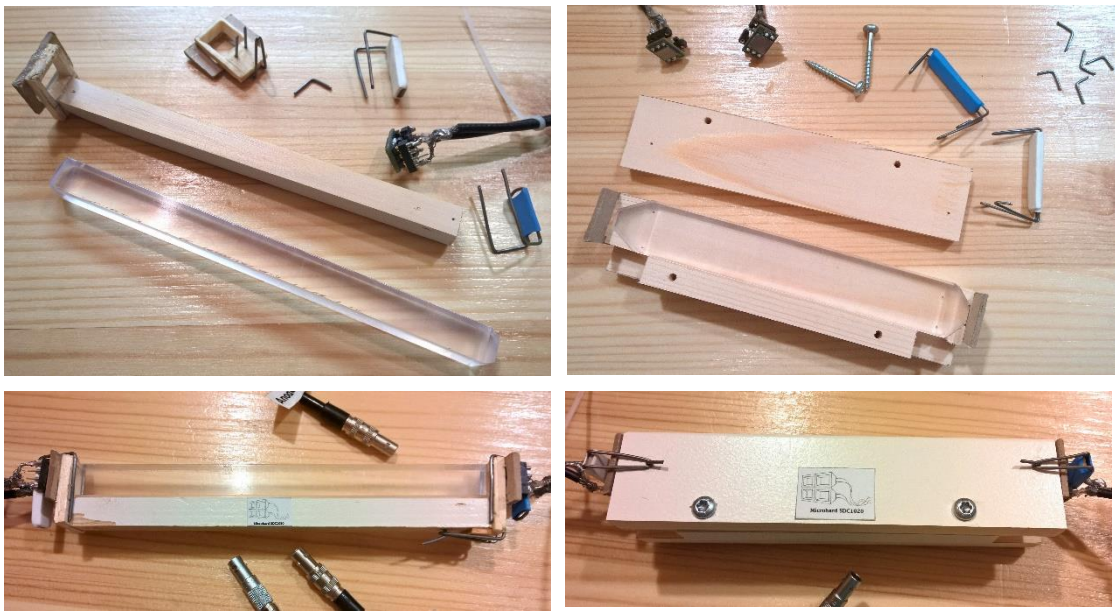

Figure 6.2: Design of the assembling apparatuses: Scintillator Detector Coupler for Scintillator 1 (left) and Scintillator 2 (right).

As illustrated in Figure 6.2, Scintillator 1 was held by the coupler from the ends, then the SiPMs were fitted into the 6 × 6 mm^2 wells and mounted on the ends of the scintillator by the clips and safety pins. Three sides of Scintillator 1 were left unshielded for receiving and passing the incident radiation. Scintillator 2 and similarly 3, were fitted into the compartments and held by the screw-mounted lads. Then the SiPMs were fitted into similar wells and coupled to the scintillators by the clips and safety pins. In each structure ~ 0.5 mm space was reserved around the scintillators for the reflective foils to be installed later. All these structures were designed with hard wood which would facilitate the required rearrangements during the measurements. The idea was that the 6 × 6 mm^2 photosensor was precisely matched with the light guide by secured coupling in order to prevent any possible slippage or detachment during the measurements which may lead to poor reliability or potential invalidity of the measured results. On the other hand, the thin glass covering the photosensor

was fragile and subject to fragmentation. Therefore, the structures formed by the clips and safety pins were designed with 0.75 mm steel wire with just enough tenacity and the buffer strips made of rubber tube, such that possible excessive force exerted on the photosensor would be absorbed by the structure.

A vacuum chamber was built as light tight and appropriately levelled for the measurements. As illustrated in Figure 6.3, the EDWARDS - nXDS10i scroll pump was connected to the chamber with a feedthrough to create a vacuum better than 10 mbar in order to avoid energy loss of particles in collisions with the air molecules. The air pressure inside was monitored by the Bourdon tube vacuum gauge A venting valve was mounted on the chamber to balance the air pressure inside with the atmospheric pressure when the chamber needs to be opened after each measurement. In order to minimize possible disturbance caused to the measurements, the source holder was fixed onto a movable rod mounted with a feedthrough to allow for position adjustment of the radioactive sources. A view of the interior of the measurement chamber is shown in Figure 6.4. The radioactive sources were moved to various positions relative to the scintillators by the moveable source holder rod. The cathodes and anodes of the SiPMs were connected through a feedthrough to a power supply and signal readout devices, respectively.

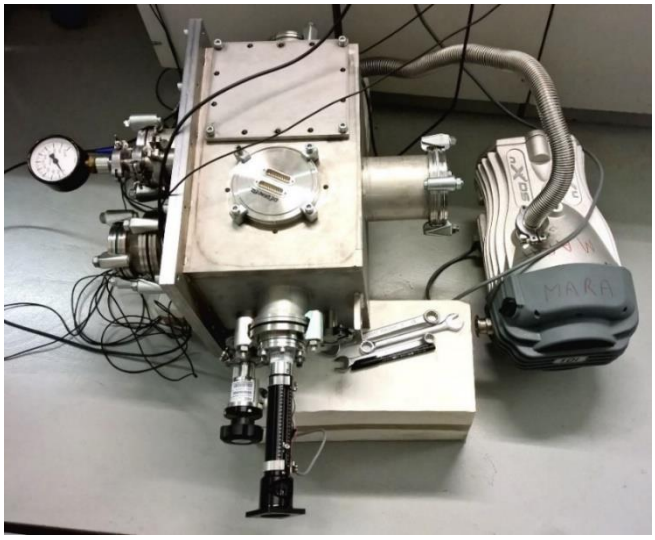

Figure 6.3: Light tight measurement chamber setup. Reverse biasing of the SiPM: cathode connected to the power supply and anode connected to the signal readout.

The Data acquisition system was composed of Nutaq digitizer with 100 MHz sampling rate, Midas data-acquisition software, and Grain online data-analysing programme. The voltage pulse obtained from the SiPMs was digitized into traces which are formed by arrays of integers with the array index representing the time bin and the corresponding height of the SiPM signal at that specific time. The signal was generated by applying an integration over the time domain [32 → 195] ns, with integration over the remainder of the pulse to determine the baseline. Then the energy information was extracted from the traces using the following algorithm, which was used to evaluate the area, i.e., the integral of the obtained signal with appropriate baseline subtraction:

$$\begin{cases} \text{Baseline} = \text{Sum of trace}[3 \rightarrow 30] + \text{trace}\,[196 \rightarrow 246] \\ \text{Signal} = \text{Sum of trace}[32 \rightarrow 195] \\ \text{Energy} = \dfrac{\text{Signal} - (196 - 32)\dfrac{\text{Baseline}}{(31 - 3) + (247 - 196)}}{196 - 32} \cdot 2 \end{cases} \tag{6.1}$$

The pulses generated by different types of detector differ in shape, for example, the plastic scintillator produces relatively faster pulses than the silicon detector. Depending on the pulse shape, these integration limits were set accordingly to generate the total energy of the signal which is covered under the integration area, such that the shape of the energy spectrum can be defined [5].

In the end of this preparative stage, a bias voltage of 29 V was applied across. In order to avoid possible heating up of the SiPMs caused by excessively high current conducted through the SiPMs, which may melt the scintillator material, an upper limit of the output current was set to be 5 mA. The whole system was tested with an α source to function as expected. An oscilloscope was employed as well to investigate the SiPM signal characteristics.

6.2 Detection performance with alpha particles

6.2.1 Experimental methods

- Measurement No. 1:

After the detector formed by Scintillator 1 and two SiPMs was set to a fixed position, the ^{241}Am source (JYFL-83) as an α emitter ($t_{1/2} = 432.2\text{y}$) was mounted on the source holder at 20 mm distance from the scintillator. An appropriate threshold was set to filter some noise out. The source was moved from one end of the scintillator to the other by adjusting the knob with 1 cm displacement each time. At each position the signals were measured for 5 minutes. The centroids of the energy spectra and FWHM values obtained from Gaussian fits were collected for both SiPMs located at each end of the scintillator bar.

- Measurement No. 2:

Next, a collimator with a circular aperture of 2.5 mm in diameter and 15 mm thickness was made of dry pinewood and mounted in front of the active area of the source, as shown in Figure 6.4. The same measurements as in Measurement No. 1 were repeated to test for the effect of collimation on the measured α-energy spectra.

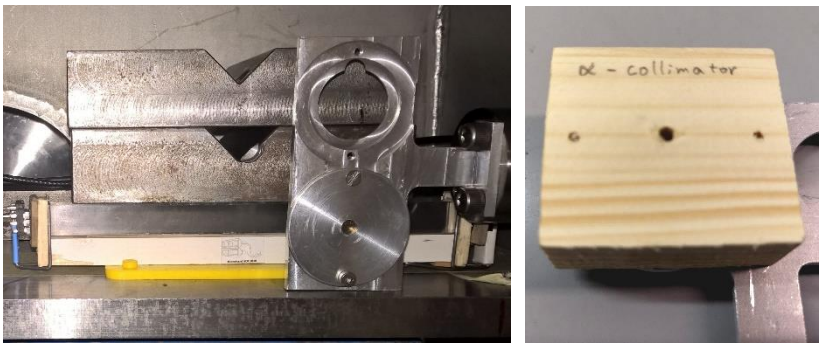

Figure 6.4: The detector and source setups inside the chamber (left), the collimator mounted in front of the α source (right).

- Measurement No. 3:

As shown in Figure 6.5, the Enhanced Specular Reflector (ESR) foil was cut into desired patterns with my design, by which the scintillators were enveloped in an optimized manner. With this optimized enveloping, the scintillation light inside the scintillators would always be reflected towards the SiPMs without being trapped or back-reflected by any deformity of the reflective surfaces. The ESR foil is a mirror-like, highly reflective film used for high efficiency optical enhancement. In this work, it was used to create a highly efficient specular reflector. A hole with a diameter of 3 mm was left at the center of the scintillator, by which an effective collimation of α particles was achieved. The energy spectrum was acquired for 10 minutes.

Figure 6.5: Enveloping of Scintillator 1 with paper and ESR foils.

- Measurement No. 4:

In order to test the performance of the detector in slow and fast signal discrimination, the frontal face of the ESR foil was replaced by the ZnS(Ag) film. The measurement was done at the center of Scintillator 1 with and without the collimator. The measurement without collimator was performed for 5 minutes, while that with collimated α particles was made for 10 minutes.

6.2.2 Alpha energy spectrum without reflector

The energy spectra of the 5.5 MeV uncollimated α particles measured without reflective foil showed Gaussian-like distributions, as illustrated in Figure 6.6.

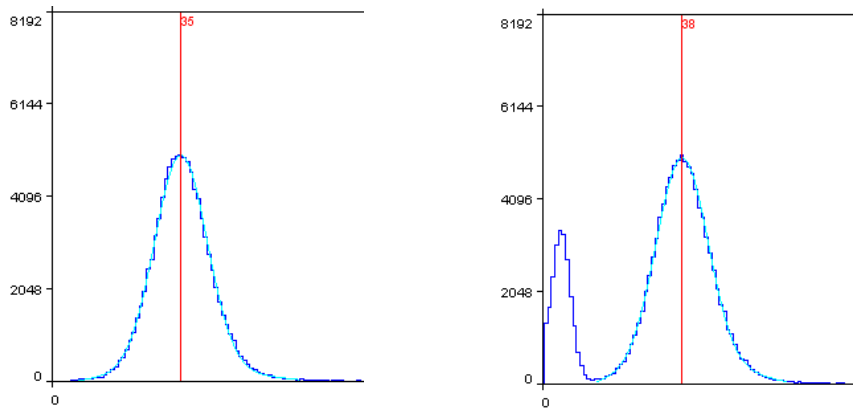

Figure 6.6: Alpha particle energy spectra measured without collimator: at the 45° end (left) and at the 60° end (right), without reflective foil and collimator.

The spectra shown in Figure 6.6 were produced with the α source placed at the center of the scintillator, so that both detectors were located at equal distances to the origin of the scintillation lights. It should be noted that the uncollimated α particles could be incident at any point on the scintillator. It can be seen from the comparison that, the energy peak measured at the 60° end corresponds to slightly higher energy than that measured at the 45° end, with an uncertainty roughly estimated to be 2 arb. units. This difference in the measured peak centroids shows that the light collection with the 60° light guide is about 10% better than the 45° end. The energy resolution in response to α particles was determined according to Eq. (5.3) to be ~45% consistently over the positions. It should also be noted that the low energy peak observed in Figure 6.6 (b) originated from the noise, which was mainly dark current. The different shapes of noise in the two spectra showed that every detector has distinct response in applications.

The peak centroids and FWHM measured at various source distances D from both detectors are presented in Table 6.2. As can be seen from the plots in Figure 6.7, the general trend has been clearly observed that, particles incident on the scintillator at longer distance from the detector result in less energetic signals, and hence smaller peak centroid. Such behaviour of the calibration curves has been observed that, Detector 1 (at 60° end) and Detector 2 (at 45° end) showed equal responses to the α source being moved farther from each detector, i.e. the peak centroid decreased with similar slopes since the scintillation that occurred at a longer distance from the detector

resulted in greater fractions of light escaping through the boundary surfaces. When the length of the scintillator is much larger than that of the light guide, in this measurement for instance, effects of the angle of the light guide on light collection tends to vanish.

Table 6.2: Peak centroid and FWHM of uncollimated ^{241}Am source measured with Scintillator 1 without reflective foil.

	Detector 1 (60° end)		Detector 2 (45° end)	
D (mm)	Centroid (channels)	FWHM (%)	Centroid (channels)	FWHM (%)
10	46.21	26.40	52.69	29.16
20	43.07	23.17	48.59	24.29
30	39.87	19.98	45.16	21.36
40	37.22	17.87	41.99	20.59
50	34.87	17.02	39.09	19.30
58	33.22	16.26	37.15	18.20
64	32.07	15.88	35.65	17.54
70	30.98	15.65	34.33	16.81

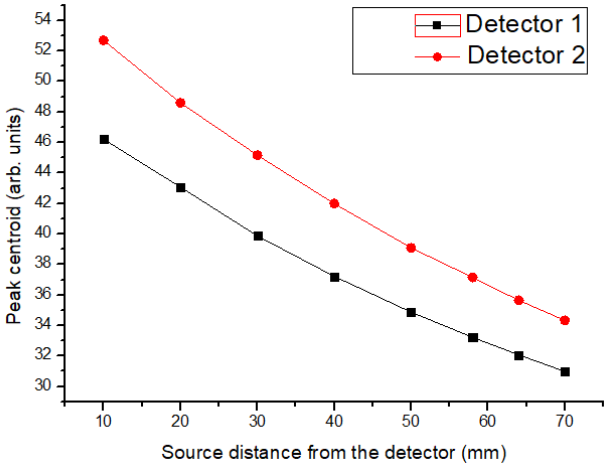

Figure 6.7: Peak centroids measured with the uncollimated α particles at different source distances from Detector 1 at the 60° end and Detector 2 at the 45° end.

6.2.3 Effect of collimation on energy spectrum

Since the α particles were emitted in all directions over the 2 π geometry, only a small fraction of the emitted particles could travel through the collimator and impinge on the scintillator, resulting in a dramatic drop of the count rate, as presented in Figure 6.8. Due to the low count rate measured with the collimated

α particles, significant statistical fluctuations were observed with an energy resolution estimated to be $\sim 30 - 60\%$. It was also notable that, the distribution of α energy measured with collimator did not spread as widely as in the uncollimated case. The peak centroids and FWHM measured at various source distances from the detectors are presented in Table 6.2.

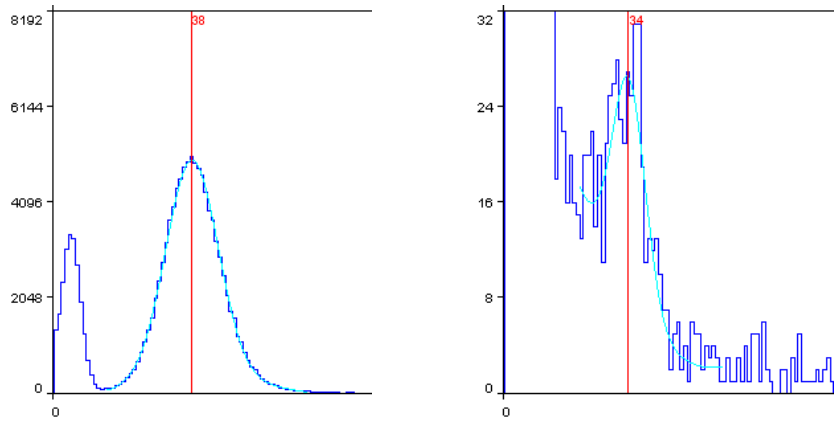

Figure 6.8: Effect of collimation on the measured spectrum: without collimator (left), with collimator (right).

Table 6.2: Peak centroid and FWHM of collimated ^{241}Am source measured with Scintillator 1 without reflective foil.

	Detector 1 (60° end)		Detector 2 (45° end)	
D (mm)	Centroid (channel)	FWHM (%)	Centroid (channel)	FWHM (%)
10	57.58	16.84	56.99	21.23
20	49.21	15.33	50.56	15.17
30	42.12	14.38	45.13	15.46
40	40.89	11.72	40.73	14.67
50	37.84	11.26	38.47	12.37
58	34.16	13.45	35.70	11.70
64	32.53	16.30	35.91	11.89
70	32.25	13.77	33.33	11.43

6.2.4 Effect of external reflector on light collection

With the reflective foil covering most area of the scintillator surface, the number of events detected was decreased. However, the measured spectrum still showed a rather smooth distribution. As illustrated in the comparison in Figure 6.10, with the reflective foil light collection was significantly enhanced by a

factor of ~ 3. The energy resolution was determined to be ~20%, which is about half of that obtained in the uncovered case due to the effect of collimation.

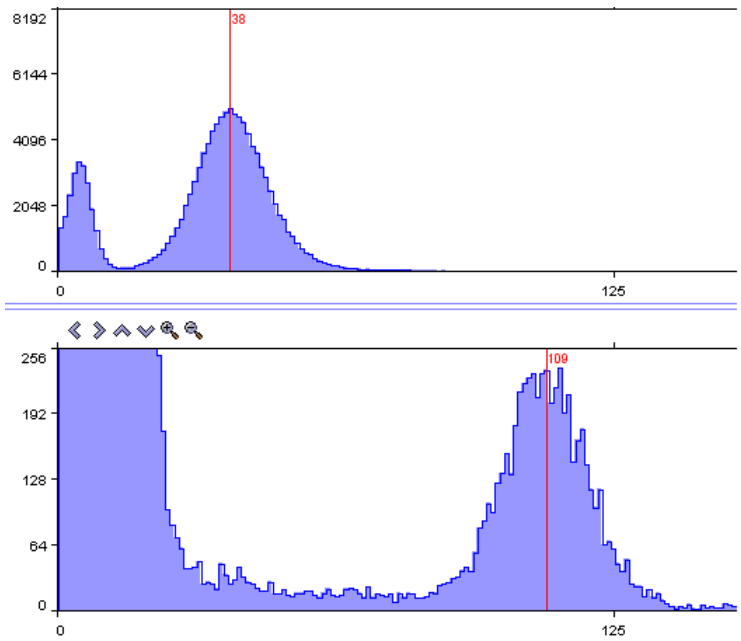

Figure 6.10: A comparison of light collection with and without reflective foil: α particle energy spectrum measured at the center of Scintillator 1 without reflective foil (top) and with reflective foil (bottom).

6.2.5 Slow and fast signal discrimination

The fast and slow signals were generated by integrations of the trace over time domains [32 → 82] and [82 → 132], respectively, as illustrated in Figure 6.11.

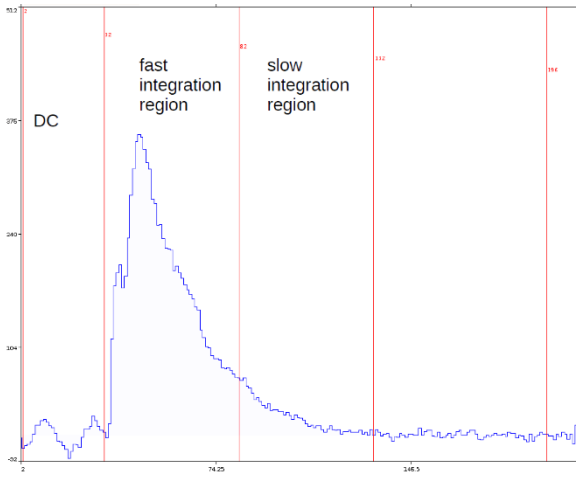

Figure 6.11: Integration methods of a trace for fast and slow signal generations.

When the α particles were stopped by the ZnS(Ag) film, whereas the penetrating electrons and gammas were detected by the plastic scintillator, the slow scintillation property of the ZnS(Ag) facilitated discrimination of the slow and fast signals. These signals were compared to those produced by the ^{207}Bi-induced conversion electrons and gammas. As illustrated in the 2D histograms in Figure 6.12, without any sources used, the measurement of background gammas yielded fast signals, without the ZnS(Ag) film, only fast signals were generated by the plastic scintillator with alphas, electrons, and gammas. With the ZnS(Ag) film, the signals produced by electrons, gammas, and alphas emitted in the decay of ^{241}Am were clearly distinguished as fast and slow signals.

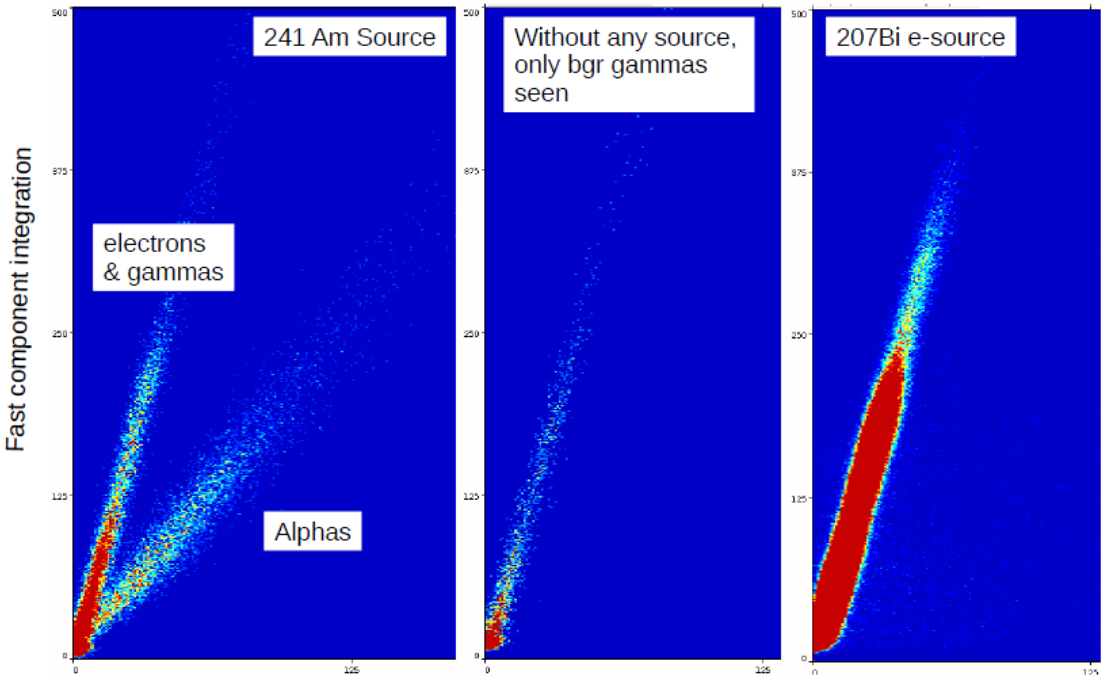

Figure 6.12: Fast and slow signal discrimination with ZnS(Ag). Slow and fast signals were clearly separated by using the ZnS(Ag) film (left), fast signals measured from background gammas, and fast signals produced by alphas, electrons, and gammas without the ZnS(Ag) film [51].

The pulse shapes of fast and slow signals were also distinguished from the normalized traces, as shown in Figure 6.13.

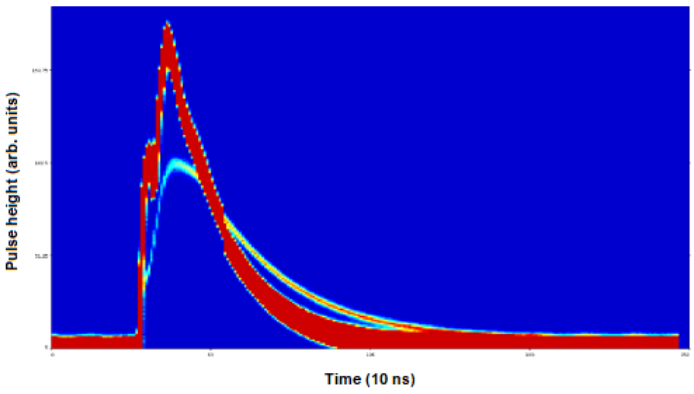

Figure 6.13: Normalized fast and slow traces. The fast pulse (red) rises and decays faster with a relatively shorter tail than the slow pulse (green) [51].

6.2.6 Timing property

The timing performance in fast and slow signal discrimination tested with ^{241}Am was evaluated by the rise time and different portions of the decay components corresponding to 10%, 50%, 90%, and 100% of the maximum signal amplitude. An estimation of the timing property for detections of electrons and gammas and alphas was obtained with aids of Figure 6.13, as presented in Table 6.2. The slow components of the signals (Slow signal$_\alpha$) were produced by the slow scintillation of ZnS(Ag). The timing of the plastic scintillator in pulse generation for α detection without the ZnS(Ag) film was estimated with an oscilloscope, as shown in Figure 6.14. Based on these analyses, a comparison between the timing properties in fast and slow signal generations of this detector setup can be visualized.

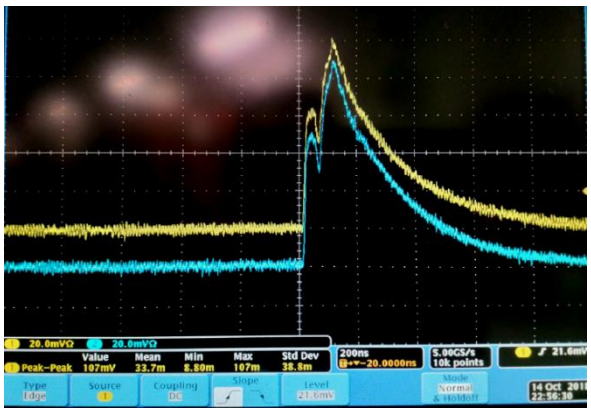

Figure 6.14: Signals in α detection obtained with Detector 1 (yellow) and Detector 2 (blue) and displayed by an oscilloscope.

Table 6.2: Timing properties of the detector for fast and slow signals.

Time (ns)	Fast signal$_{e\,\&\,\gamma}$	Slow signal$_{\alpha}$	Fast signal$_{\alpha}$
τ_{rise}	116.7	140	110
$\tau_{10\%\text{ decay}}$	46.7	163.3	40
$\tau_{50\%\text{ decay}}$	163.3	338.3	180
$\tau_{90\%\text{ decay}}$	466.7	583.3	560
$\tau_{100\%\text{ decay}}$	700	1283.3	800

6.3 Detection of gamma emission

The ^{137}Cs source (JYFL – 31) with $t_{1/2} = 30.17\ y$ and ^{60}Co (JYFL-80) with $t_{1/2} = 5.27\ y$ were used as the γ sources to examine the γ efficiency of the detector at 20 mm from the scintillator. The measured spectra are presented in Figure 6.15. As can be seen from the measured γ spectra, the energy resolution of the scintillator was not competent to separate the 1173 keV and 1333 keV γ rays in the cascade emitted by ^{60}Co. In this case, the average of the two individual Compton edges was taken into account for energy calibration. Moreover, the energy peak and Compton edge can be sharply defined by an ideal detector with infinitely good resolution, however, with the scintillator used in this measurement, blunt Compton edges with certain inclination were obtained along with the energy spectra, and this consequently prompted the difficulty in extracting a numerical estimate for the energy resolution. As discussed in Section 3.4.3, the Compton edge corresponds to the maximum photon energy transferred to the electron in Compton scattering, where the incident γ photon is backscattered. It should be noted that no γ-ray photopeak was observed in the measured spectrum, which shows that the γ ray interacted with the scintillator mainly through Compton scattering without full energy deposition. The Compton edges in the ^{137}Cs, ^{60}Co, and ^{207}Bi energy spectra were determined using Eq. (3.40) and tabulated in Table 6.4. Energy calibration with ^{137}Cs, ^{60}Co is presented in Figure 6.16.

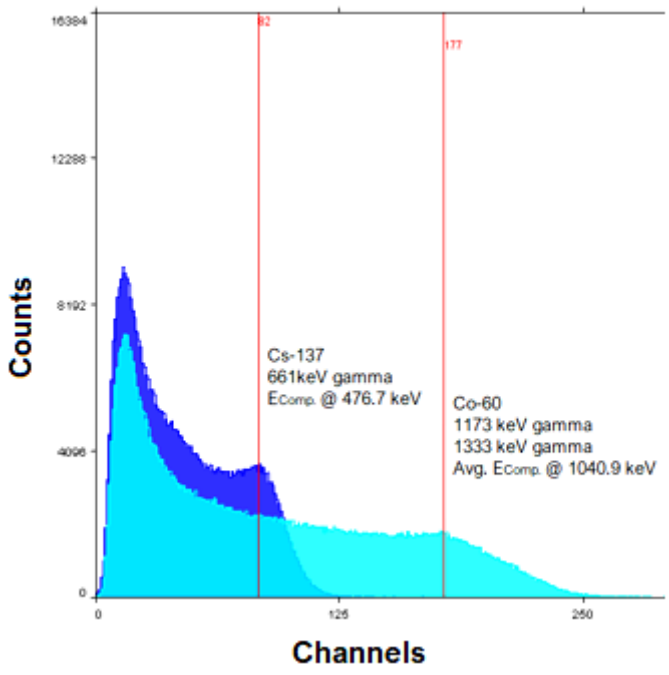

Figure 6.15: Measured energy spectra of ^{137}Cs and ^{60}Co γ emissions.

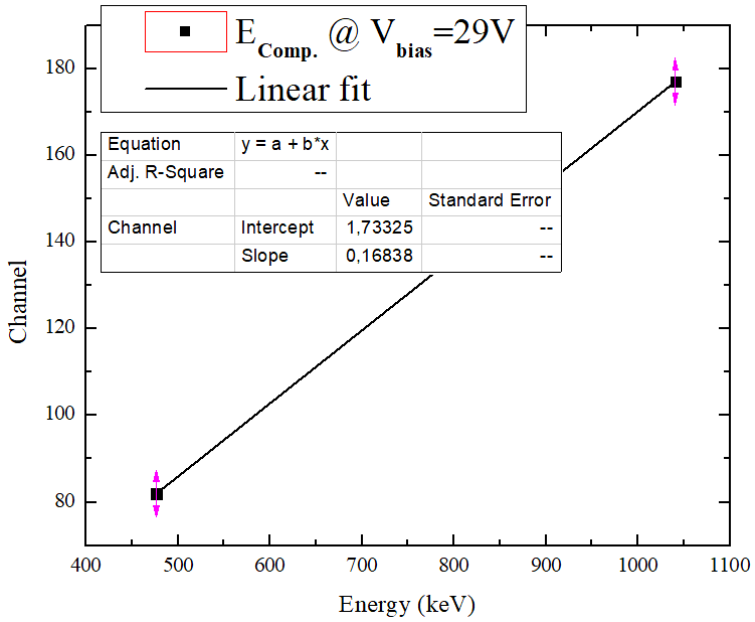

Figure 6.16: Energy calibration based on the data points corresponding to the Compton edges calculated for ^{137}Cs and ^{60}Co.

The half-value thicknesses corresponding to these γ energies were calculated by using Eq. (5.5) and referring to Table C – 1 in Appendix C, as listed in Table 6.3.

Table 6.3: Calculated half-value thicknesses for γ energies involved.

Source	E_γ (keV)	μ/ρ (cm^2/g)	HVL (cm)
^{137}Cs	661.7	$8.732 \cdot 10^{-2}$	7.8
^{60}Co	1173.2	$6.16 \cdot 10^{-2}$	11.0
	1332.5	$5.611 \cdot 10^{-2}$	12.1
^{207}Bi	569.7	$8.732 \cdot 10^{-2}$	7.8
	1063.7	$6.89 \cdot 10^{-2}$	9.8
$\rho_{scint} = 1.023\ g/cm^3$			

For plastic scintillator with low Z and density, the attenuation of γ rays is considerably low. Only a small fraction of the incident γ rays interact with the scintillator and a small portion of the photon energy is absorbed, while the majority of the γ rays are scattered off of the scintillator and a part of these rays does not undergo interaction at all. As presented in Table 6.3, the calculated values of HVL for these γ energies were quite large. In the future detector setup with the plastic scintillator, the minimum thickness of the plastic scintillator that would be sufficient to stop a 10 MeV β particle was calculated to be 51 mm, according to Eq. 3.27. In practice, there are many computer tools available for determination of electron ranges in matter, such as LISE ++ and SRIM, etc [52]. The attenuation of γ rays with typical energy range caused by this thickness is very low. A comparison of the HVL between the plastic scintillator and Ge detector can be extracted from Figure 6.17. For 1 keV photons, the HVL of the plastic scintillator is about 20 times larger than the HVL of a Ge detector. In the case of 1 MeV photons, the HVL of the plastic scintillator is about 4 times larger than that of a Ge detector.

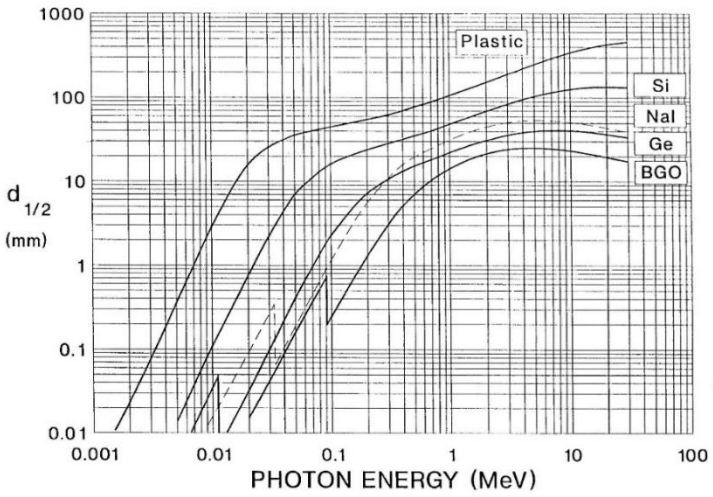

Figure 6.17: Half-thicknesses for photon attenuation in most common solid X-ray and γ-ray detector materials [53].

^{207}Bi (JYFL - 91) with $t_{1/2} \sim 31.55y$ was placed at 20 mm from the center point of the scintillator as the conversion electron source to test the response of the detector. Scintillator 1 was tested in a 5 min measurement with collimated electrons using the same collimator as mentioned previously, with the reflective foil. Justification of the electron range in the collimator and in the scintillator is presented in Appendix E. In this measurement, the conversion electrons were able to penetrate the reflective foil with negligible energy straggling caused by the foil [9]. The energy spectrum of ^{207}Bi transitions measured with the reflective foil is presented in Figure 6.18.

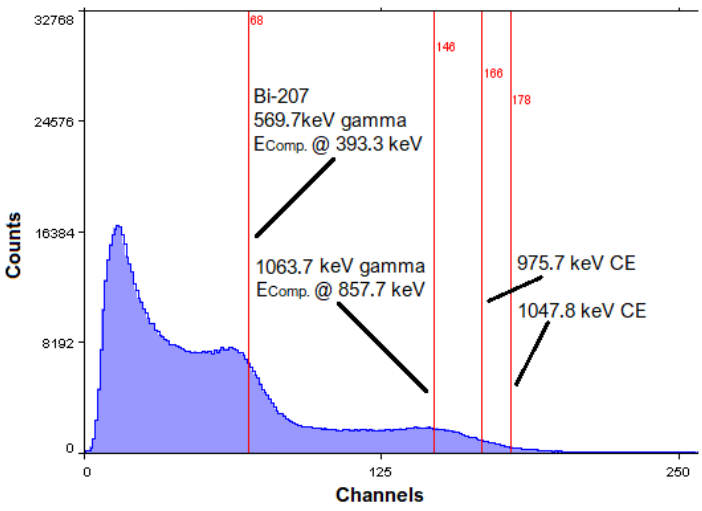

Figure 6.18: : ^{207}Bi decay spectrum measured with Scintillator 1 with reflective foil.

The spectrum measured with reflective foil was also compared to that obtained without the reflective foil, as presented in Figure 6.19. In the case without the reflective foil, the two Compton edges were roughly identified corresponding to Channel number 25 and 63, respectively. Without the reflective foil, due to the less effective light collection resulting from more light escaping from the detector, the measured spectrum showed that a larger number of less energetic signals were collected.

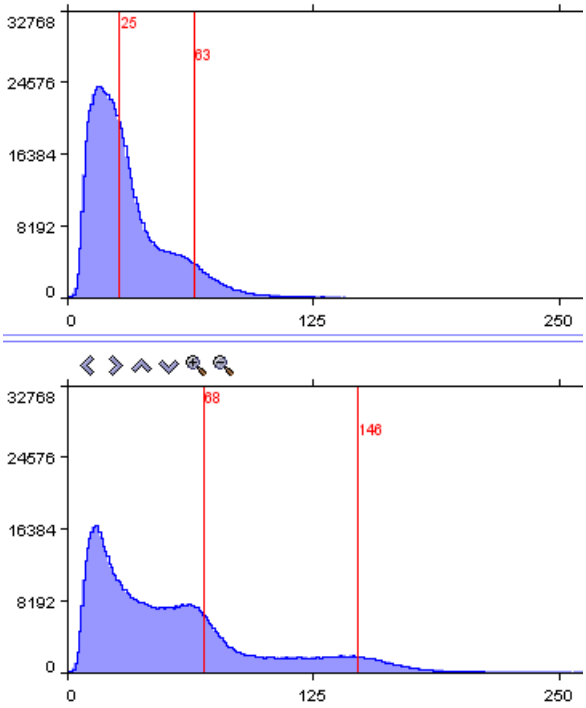

Figure 6.19: ^{207}Bi decay spectrum measured with Scintillator 1: without reflective foil (top) and with the foil (bottom).

The ^{207}Bi nuclei decay primarily through electron capture to the excited states of ^{207}Pb. The resulting excited states of ^{207}Pb subsequently decay via γ emission of 569.7 keV (97.9%) and 1063.7 keV (88.8%) and internal conversion to the ground state, emitting conversion electrons of 975.7 keV (8.36%) and 1047.8 keV (2.1%) [54]. The Compton edge channel numbers created by the γ photons emitted in the ^{137}Cs and ^{207}Bi decays also can be identified according to the calibration presented in Figure 6.16. It has to be noted that, due to the considerably low intensity of the IC decay modes, the discrete energies of the conversion electrons could not be identified in this measurement.

Table 6.4: Calculated values of Compton edge of backscattered γ photons.

Source	Intensity (%)	E_γ (keV)	$E_{\text{Comp.}}$ (keV)	Channel
^{137}Cs	85.1	661.7	476.7	82
^{60}Co	99.90%	1173.2	Avg. 1040.9	177
	99.98%	1332.5		
^{207}Bi	97.7%	569.7	393.3	68
	74.5%	1063.7	857.7	146

Scintillator 3 (10 mm × 30 mm) covered with the reflective foil was tested for comparison. The 10 mm × 128 mm surface was irradiated by the ^{207}Bi source for 5 min. As can be seen from the measured spectra in Figure 6.20, on the same duration of measurement, Scintillator 3 with larger thickness and volume, produced more signals than Scintillator 1 under identical conditions, the ratio of registered events was ~3.2. Compton edges of the 569.7 keV and 1063.7 keV γ photons observed with Scintillator 3 corresponded to slightly higher channels as well, as expected. With a scintillator of larger thickness and volume, the γ rays tend to be more likely to interact through the scintillator with greater energy deposition.

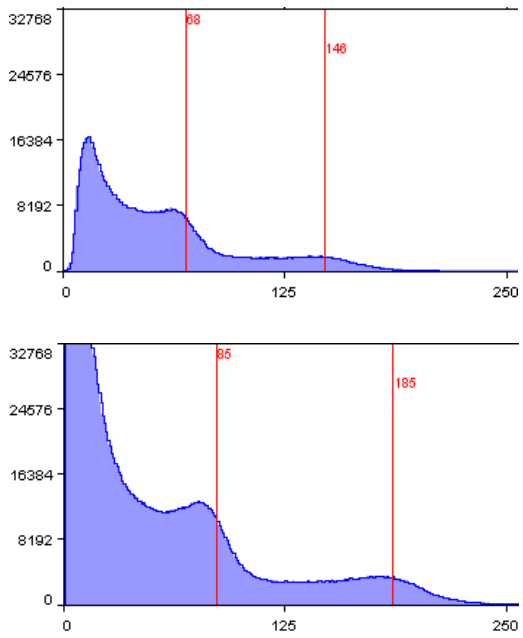

Figure 6.20: ^{207}Bi spectra measured by Scintillator 1 (top) and 3 (bottom).

6.4 Simulation with cosmic muons

In order to test for the tagging properties for β particles, radiation of the cosmic muons was used in this simulation. Since the average muon energy at the sea level is still of the order of a few GeV, it is energetic enough to penetrate the scintillators, depositing a small fraction of the energy to the scintillators. Scintillator 1 was coupled to the 128 mm × 20 mm face of Scintillator 2 and placed with Scintillator 1 facing upwards, so that the muons were supposed to penetrate two 10 mm thick scintillators. Several lead chunks were placed around the scintillators to shield the detectors from the background γ rays. Cosmic muons arrive at the Earth with a considerably low flux, ~ 1 muon/cm^2/min, thus, each measurement was held for hours. Scintillator 1 was then attached to the 128 mm × 10 mm face of Scintillator 2, in this way the muons would penetrate the 10 mm thick scintillator and then the 20 mm region, as shown in Figure 6.21. The idea was that, the light yield inside the scintillator depends on the particle range. A range of 20 mm travelled by the muons through Scintillator 2 would lead to a light yield twice as great as in a range of 10 mm. In order to simulate the β tagging with correlation techniques, the data acquisition was modified, such that only the coincidence signals detected by Scintillator 1 and 2 simultaneously were recorded as true events. The energy spectra created by the muons penetrating Scintillator 2 to the depths of 10 mm and 20 mm are presented and compared in Figure 6.22.

Figure 6.21: Detector setup for the measurement with muons.

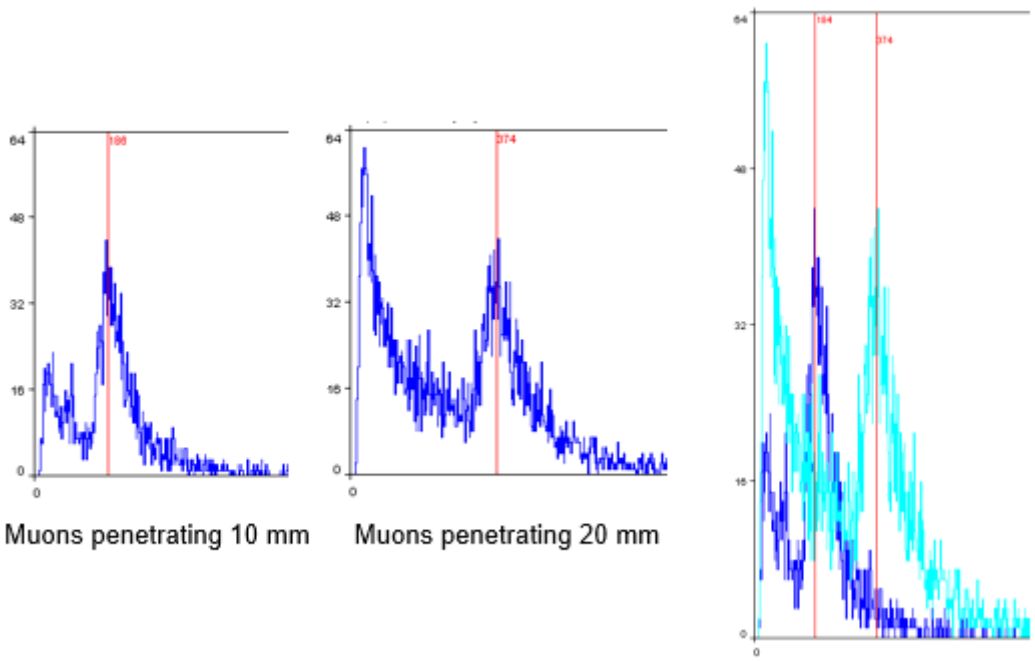

Figure 6.22: Energy deposition of muon at ranges of 10 mm and 20 mm.

6.5 Detection efficiency

- ***Geometrical efficiency***

Scintillator 2 and 3 were only tested with highly penetrating γ rays and muons and the geometrical efficiency of Scintillator 1 counted only the case without reflective foil and collimator. For all detectors, the effective surface of the scintillator can be regarded as 128 mm × 10 mm, and all measurements were operated at 20 mm from the scintillator. Therefore, according to Eq. (5.7), $\alpha = 128/(2 \times 20) = 3.2$, $\beta = 10/(2 \times 20) = 0.25$, the solid angle can be calculated by

$$\Omega = 4\cos^{-1}\sqrt{\frac{1+\alpha^2+\beta^2}{(1+\alpha^2)(1+\beta^2)}}$$
$$= 4\cos^{-1}\sqrt{\frac{1+3.2^2+0.25^2}{(1+3.2^2)(1+0.25^2)}} = 53.54° \approx 0.952 \text{ rad}$$

And then, according to Eq. (5.8), the geometrical efficiency is determined to be

$$\varepsilon_{\text{geo}} = \frac{\Omega}{4\pi} = 7.6\%$$

- ***Absolute and intrinsic efficiency***

Calculations of the activities of all sources used in the measurements and their decay schemes are available in Appendix F. The measurement with ^{207}Bi was used in determinations of the absolute and intrinsic efficiencies of the detector with reflective foil. The activity of the ^{207}Bi source was 320.451 kBq on the date of measurement. The background count rate was measured to be 5.08 counts/s, which yields 5486 events recorded from the background during the 5 min measurement. 850672 events were registered in total by the detector in 300 s, subtraction of the background gives 849148 events resulting from the ^{207}Bi decay. And then, with the determined geometrical efficiency of 7.6%, the absolute and intrinsic efficiencies were determined to be $\epsilon_{\text{abs}} = 0.88\ \%$ and $\epsilon_{\text{int}} = 11.6\ \%$, according to Eq. (5.9) and (5.10).

7. SiPM angular response and light guide geometry

This independent study of the relative PDE dependence on angular response of the SiPM (i.e. the pulse amplitude relative to normal incidence) and light guide geometry originated from my proposed hypothesis that the relative photon detection efficiency of a SiPM-based detector has a determining dependence on the angle of incidence of the scintillation light. The scintillators employed in the measurements were machined and polished with such a precision that left the surfaces of the light guides a notable non-uniformity of degree of smoothness causing diffusions of the incident light. In addition, the optical grease applied between the scintillator and the SiPM was collecting dust particles from the air during the measurements, this caused a fluctuation of its optical transparency and light transmission efficiency. Moreover, the coupling was also degraded by the evaporation of the grease in vacuum. All these unquantifiable issues resulted in the difficulty of extracting a realistic comparison of the light collection between the 45° and 60 ° light guide geometries. Thus, a systematic attempt at obtaining experimental evidence and geometrical optical analysis was thereby performed, in view of demonstrating the mechanism by which signal detection efficiency is influenced by the light guide geometry.

For such detector setup that consists of a scintillator and a photodetector, when other physical factors are fixed, the light collection and detection performance is influenced by two determining factors:

$$\begin{cases} \text{Angular distribution of the scintillation light output} \\ \text{Angular response of the photodetector} \end{cases}$$

7.1 Demonstration of the SiPM angular response

Since the energy, orientation, and frequency of occurrence of the scintillation light which is produced by interaction of ionizing radiation with the scintillator material is uncontrollable, a simple experimental apparatus was designed for simulation of the scintillation light emission by periodical generation of optical

quanta with constant energy. As illustrated in Figure 7.1 and 7.2, the angler's glow stick was used as a constant light source. When the different chemical substances inside the stick are mixed well under external extrusion, the stick becomes activated and constantly emits luminescent light with a decay time ~ 6 hours. Therefore, the irradiance can be reasonably assumed to be constant during a measurement duration of ~ 30 min.

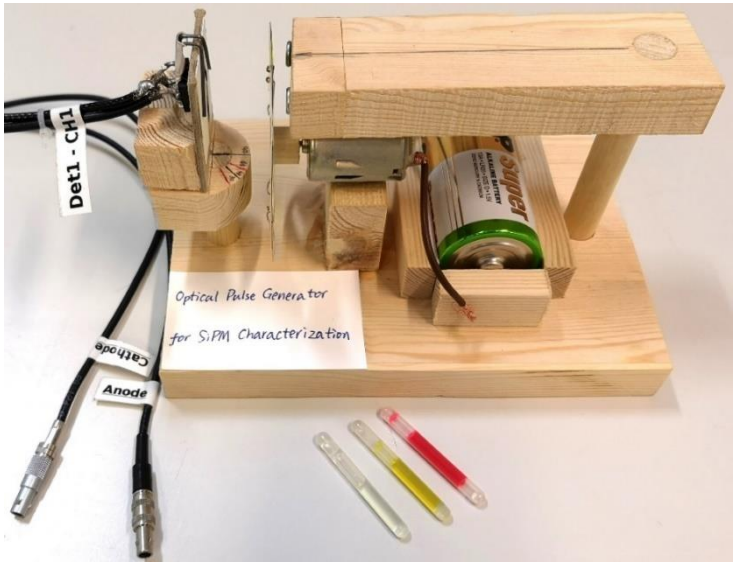

Figure 7.1: Design of the Optical Pulse Generator.

When the activated glow stick is fitted into the compartment and secured by the 2.5 mm × 15 mm collimator, the light is directed towards the 6 mm × 6 mm photosensor. The light source and the plane of photosensor are aligned, such that the light beam is always oriented towards the center of the SiPM photosensor, regardless of the angle of incidence. When such constant light beam is periodically swept across by the rotating panel (RP), on which degree of transparency varies from sector to sector, optical pulses are generated with certain rise time and decay time. As can be seen from Figure 7.2 (b), the rotating panel is composed of four open windows (transparent region), on each side of the transparent region is a region of translucent plastic film, providing reference to the pulse amplitude, and four opaque regions creating the base level of the pulses. One rotation cycle (2π) of the panel produces four identical optical pulses with equal periods. The rotating panel is driven by a motor with

an angular frequency $\sim 150 - 200$ rad/s. As a result, the flashing light is generated at a frequency $\sim 90 - 130$ Hz and directed to the center of the SiPM photosensor. By rotating the SiPM platform and setting the angle of incidence and analysing the pulse shape obtained at 0°, 30°, 45°, and 60°, the angular response of the SiPM can be obtained.

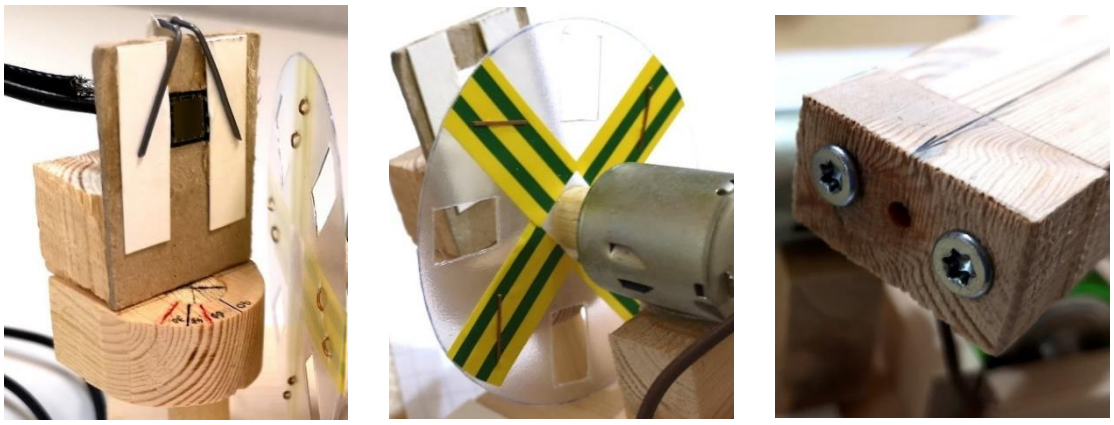

(a) (b) (c)

Figure 7.2: Components of the Optical Pulse Generator: (a). Angle adjustment of the photosensor, (b). Rotating panel composed of transparent, translucent, and opaque regions, driven by the motor, (c). 3 mm collimator producing parallel light output.

In this experiment the blue light (~ 420 nm) was used in accordance with the wavelength of the scintillation light, as presented in Figure 7.3.

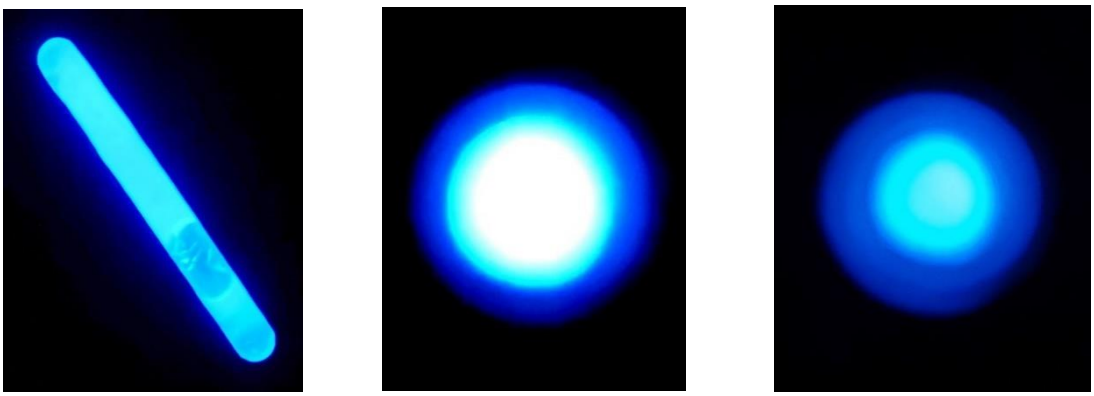

(a) (b) (c)

Figure 7.3: Light source for optical pulse generation: (a). Activated glow stick emitting wavelength ~ 420 nm, (b). light intensity corresponding to the pulse amplitude, (c). light intensity reduced by the translucent film.

The pulse shape was generated by the oscilloscope in such a form as presented in Figure 7.4. The measured pulse shapes and amplitudes are presented in Figure 7.5.

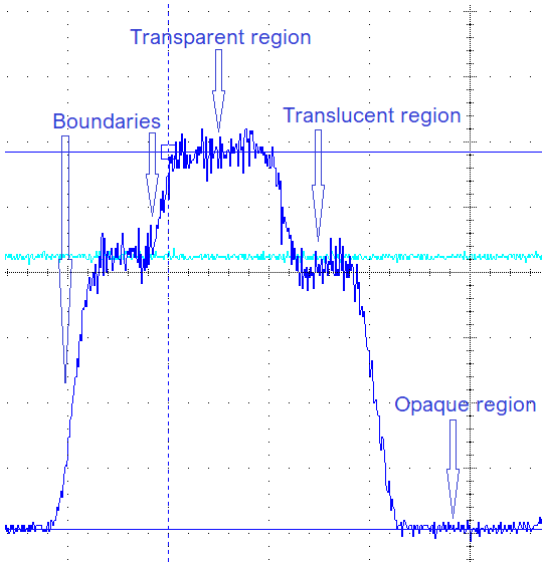

Figure 7.4: Pulse shape formation corresponding to different regions of the RP.

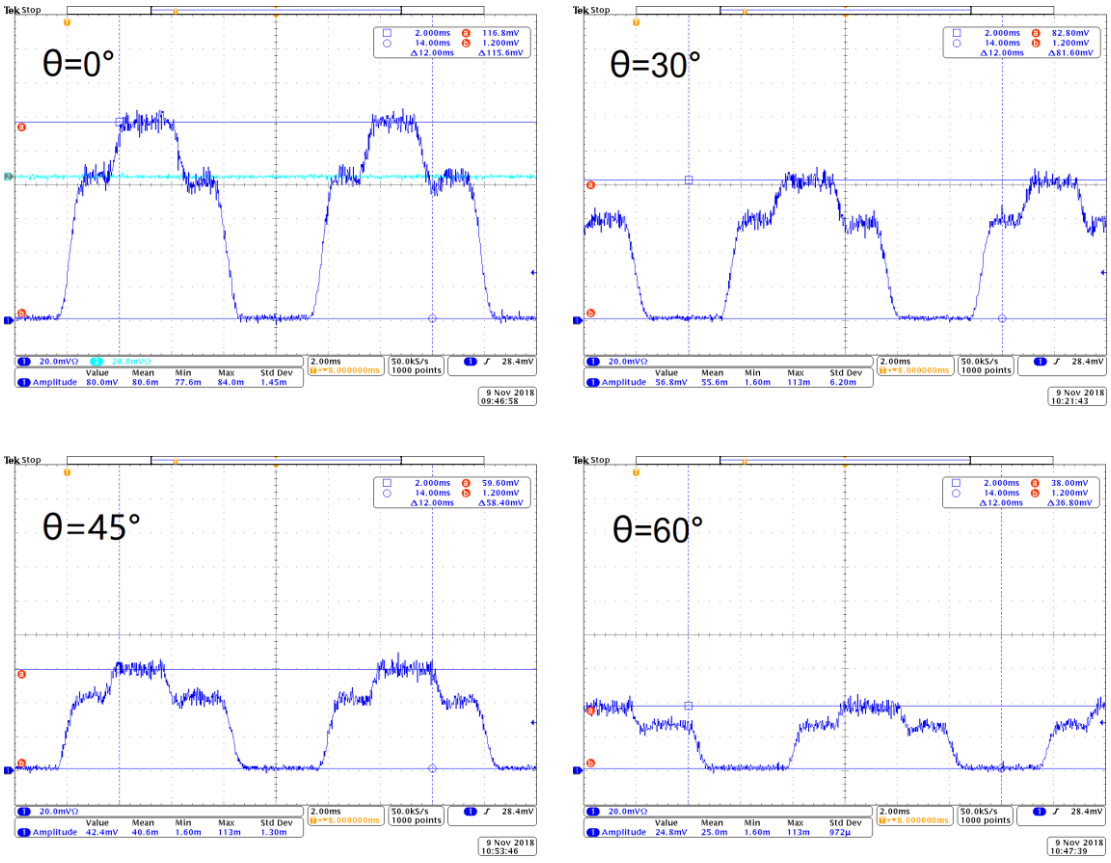

Figure 7.5: Pulse shapes measured at angle of incidence of 0°, 30°, 45°, and 60°.

As depicted in Figure 7.5, the obtained relative PDE was represented by pulse amplitudes measured at different angles of incidence. The measurement data are presented in Table 7.1, from which the angular response of the SiPM was plotted in Figure 7.6.

Table 7.1: Characterization data of the SiPM angular response.

Light beam: $\lambda = 420$ nm, collimated Bias voltage: $V_{bia} = 29$ V			
Incidence angle (°)	Frequency (kHz)	Amplitude (mV)	Relative PDE (%)
0	0.10	115.6	100
30	0.11	81.6	70.6
45	0.10	58.4	50.5
60	0.11	36.8	31.8

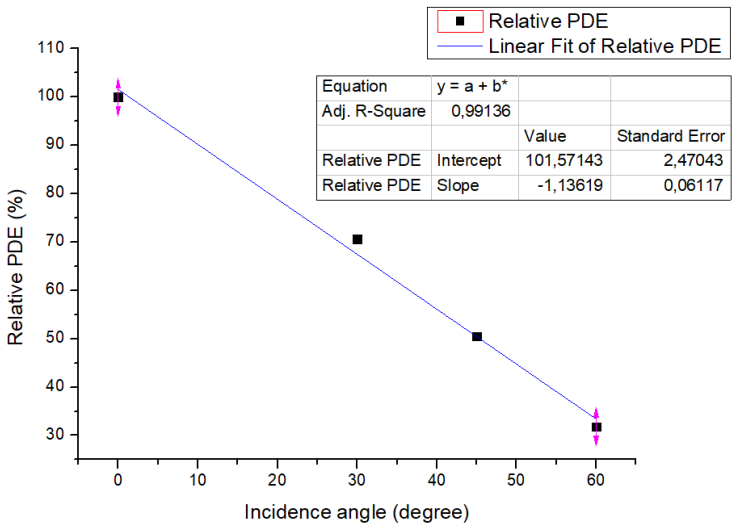

Figure 7.6: Angular response curve of the SiPM based on the characterization data.

The measured relative PDE demonstrated a linear dependence on the angle of incidence. Under the assumption that a constant irradiance is incident on the photosensor, photoelectrons produced within the same time differ in amount depending on the angle of incidence. This phenomenon can be explained by

Fresnel's law that describes the reflection and transmission of electromagnetic radiation when incident on an interface between different optical media. The behaviour of a light ray incident at angle θ_i on the interface between two materials which have different refractive indices n_1 and n_2 is illustrated in Figure 7.7 with assumption that $n_1 > n_2$. Part of the photons are reflected back within the first medium at angle $\theta_r = \theta_i$, whereas the remaining part of the photons is transmitted into the second medium at angle θ_t by refraction [55].

Light is polarized in two ways, for each type of polarization the reflectance is defined accordingly:

- p-polarized (parallel polarized) light
- s-polarized (perpendicular polarized) light

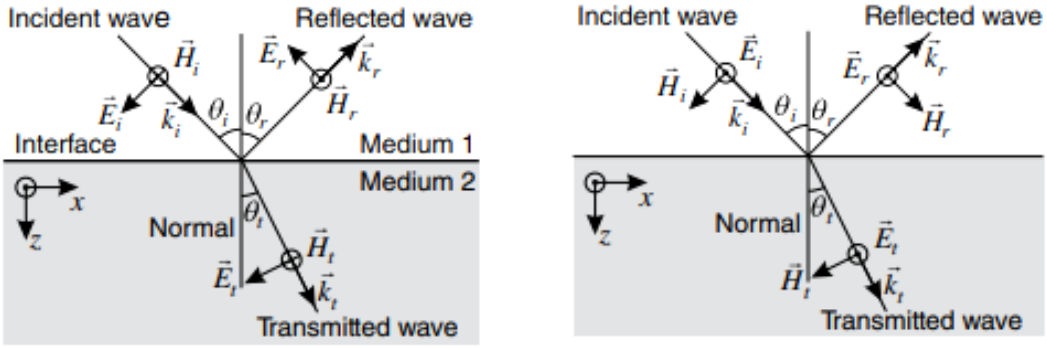

Figure 7.7: Field vectors of the incident, transmitted, and reflected waves in case of p-polarization (left) and s-polarization (right) [55].

Based on the Snell's law,

$$\frac{\sin\theta_i}{\sin\theta_t} = \frac{n_2}{n_1} \tag{7.1}$$

The reflectance R_s and R_p for the two types of polarization are defined by Fresnel's equations as

$$R_s = \left|\frac{n_1 \cos\theta_i - n_2 \cos\theta_t}{n_1 \cos\theta_i + n_2 \cos\theta_t}\right|^2 = \left|\frac{n_1 \cos\theta_i - n_2\sqrt{1-\left(\frac{n_1}{n_2}\sin\theta_i\right)^2}}{n_1 \cos\theta_i + n_2\sqrt{1-\left(\frac{n_1}{n_2}\sin\theta_i\right)^2}}\right|^2 \tag{7.2}$$

$$R_p = \left|\frac{n_1 \cos\theta_t - n_2 \cos\theta_i}{n_1 \cos\theta_t + n_2 \cos\theta_i}\right|^2 = \left|\frac{n_1\sqrt{1-\left(\frac{n_1}{n_2}\sin\theta_i\right)^2} - n_2 \cos\theta_i}{n_1\sqrt{1-\left(\frac{n_1}{n_2}\sin\theta_i\right)^2} + n_2 \cos\theta_i}\right|^2 \tag{7.3}$$

For unpolarized light, which carries equal amount of power in the *s* and *p* polarizations, the effective reflectance is given by

$$R_{\text{eff}} = \frac{R_s + R_p}{2} \tag{7.4}$$

In the special case of normal incidence, where $\theta_i = \theta_t = 0$, and distinction between s and p polarization is no longer valid. The reflectance simplifies to

$$R = \left|\frac{n_1 - n_2}{n_1 + n_2}\right|^2 \tag{7.5}$$

The reflectance refers to the portion of the incident power being reflected [55]. And then, the transmittance T that describes the portion of the incident power being transmitted to the second medium is obtained by

$$T = 1 - R \tag{7.6}$$

For monochromatic light with a particular wavelength, the energy of each photon is constant. A higher transmittance will lead to a greater number of photons transmitted, and hence produces more photoelectrons during each avalanche. Therefore, a constant irradiance incident on the photosensor at different angles will result in different relative PDE of the SiPM, accordingly. The Fresnel's equations have been developed on the basis of the simplified case of the three light rays at the interface of two different media which assumed the dielectric to have a semi-infinite thickness and by requiring the light to have

electric and magnetic fields continuous at the interface. However, in the case of a multilayered optical stack where polarization effect of light plays a role, the reflections and refractions between these layers could be rather complicated. A SiPM-based detector typically includes the scintillator, optical couplant, cover window of the photosensor (typically epoxy or glass), and the silicon substrate, with finite thickness in each layer. The light leaving the exit of the light guide is usually unpolarized, with equal composition of s- and p-polarized light. Considering the first optical layer, the light reflections for the s- and p-polarized components are different, as predicted by Eq. (7.2) and (7.3). This results in an effectively polarized light for the subsequent layers [56].

Due to the diverging property of the ordinary light used in this simulation and diffractions at the exit hole of the collimator, the light beam had dramatic divergence after travelling through the 25 mm distance until its incidence on the photosensor. Part of the stray light component arrived outside the sensor window resulting in a decrease in the pulse amplitude, and hence a large uncertainty in the measured pulse amplitudes. This effect became more significant with increasing angle of incidence and was not quantifiable with this simple setup. An ideal simulation in this experiment would be achieved by minimizing the beam divergence along its propagation, such that in each measurement the photosensor would receive equal number of photons, regardless of the angle of incidence. This can be achieved by employing a LED source to produce the light beam with a Gaussian beam profile, which has negligible divergences along its propagation and allows quantifying the stray light component projected outside the sensor area for correction [56].

Another issue affecting the measured result is the air coupling. This simulation with the light transmitted through air coupling to the photosensor could not yield a realistic result as in the case where light is transmitted from the scintillator through glue coupling to the SiPM. A more reliable characterization of the SiPM angular response was carried out by M. V. Nemallapudi et. al. using the measurement setup illustrated in Figure 7.8.

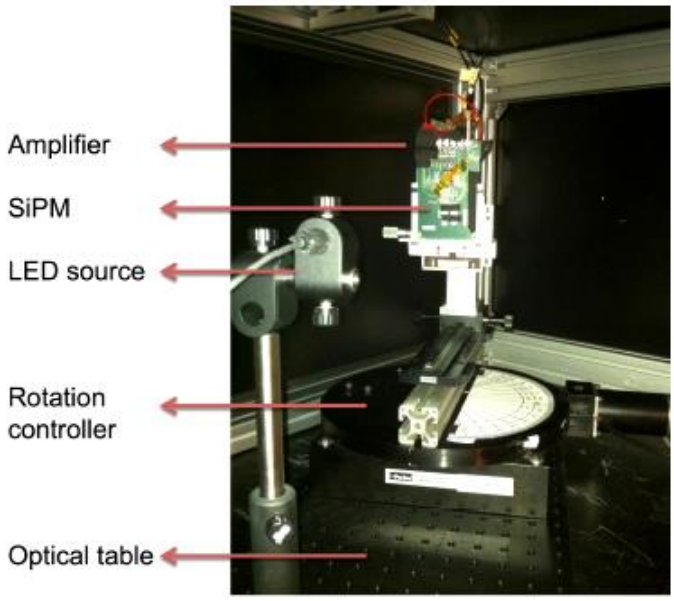

Figure 7.8: The measurement setup for SiPM angular response characterization performed by Nemallapudi et. al.. The SiPM was illuminated by the LED source at different angles with the aids of the Rotation controller. The readout was obtained through an amplifier [56].

In their study, four different SiPMs were illustrated at different angles. After the measured data were modelled with the required corrections using certain algorithm, the following characterization curves were obtained:

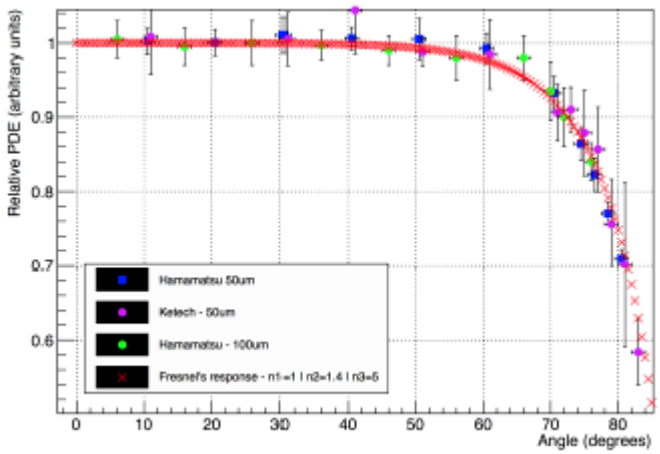

Figure 7.9: Characterization of SiPM angular response obtained with four different SiPMs using a LED source, reported by by Nemallapudi et. al. [56].

An investigation of the influences caused by air coupling and glue coupling on the angular response of the SiPM was also reported by Nemallapudi et. al., as

depicted in Figure 7.10. For smaller angles of incidence (< 45°), both response curves showed nearly constant relative PDE ~ 100%. The response curve obtained for air coupling became more sensitive to the angle of incidence compared to glue coupling at larger angles of incidence (> 45°).

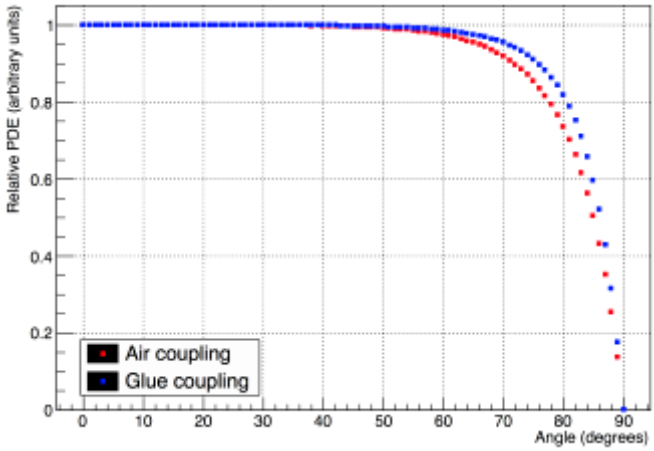

Figure 7.10: Angular response of a SiPM with air and glue coupling obtained using a LED source, reported by Nemallapudi et. al. [56].

A more comprehensive characterization of three different SiPMs to different wavelengths was reported by A N. Otte et. al.. As illustrated by the schematic of the setup in Figure 7.11, the intensity and wavelength of light emitted by the LED source was controlled by a monochromator. A filter was used to quantify the stray light component that could affect the measurements. A polarizer was employed following the filter to investigate the light polarization effect on the angular responses.

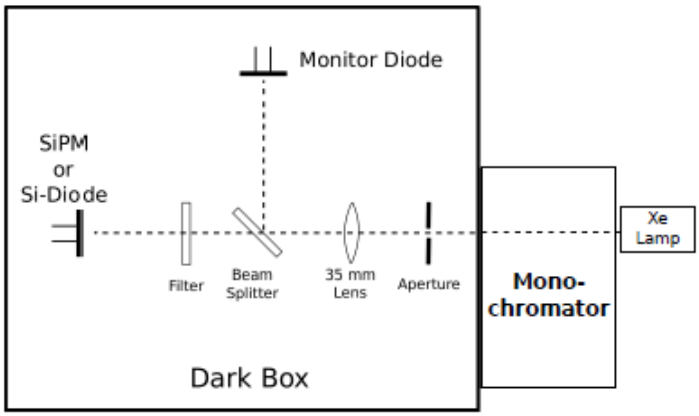

Figure 7.11: Measurement setup used by Otte et. al. in SiPM characterization [57].

The angular responses of the SensL J-series 30035 SiPM to the s- and p-polarized light were reported as shown in Figure 7.12. It can be seen that with the s-polarized light with a wavelength of 420 nm, the response becomes more sensitive as the angle of incidence increases. The response curve obtained with p-polarized light shows irregular behaviour with varying angle of incidence.

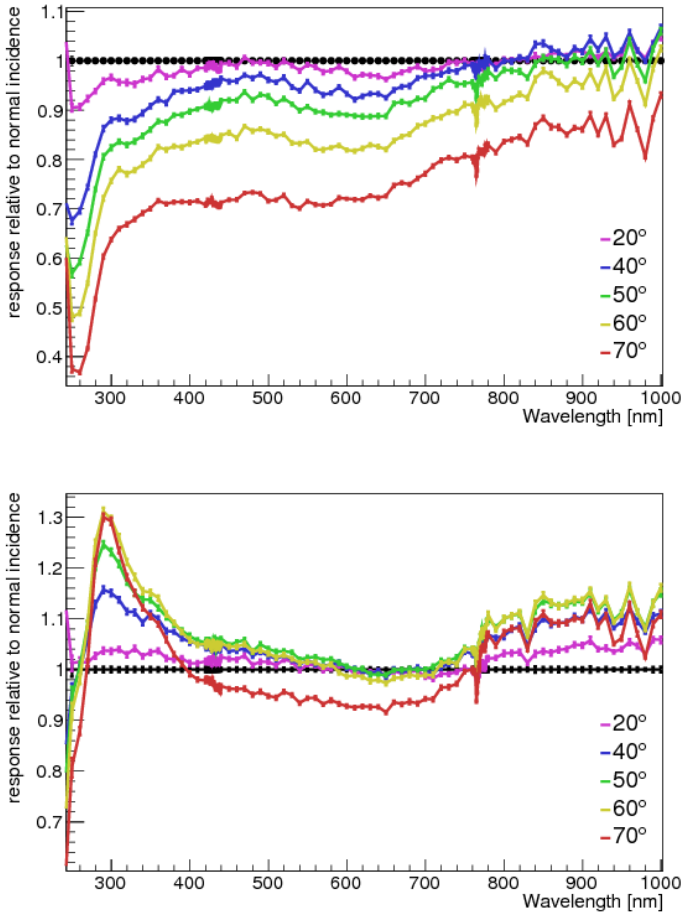

Figure 7.12: Angular response of the SensL J-series 30035 SiPM to s-polarized light (top) and to p-polaruized light (bottom), reported by Otte et. al. [57].

7.2 Light guide geometry and scintillation light output

Based on the results obtained in Section 7.1, the geometry of the light guide is a determining factor of the overall PDE of the detector since the angular distribution of the light output that results in the angular response of the SiPM is governed by reflections within the light guide. A number of researches have been conducted aiming at exploring the geometry of light guides that optimizes the photon transmission efficiency. One of the most commonly used methods

is done with the aids of various ray design and tracing computer tools which allow for simulations and modelling of the propagation of light inside the light guide. For instance, the influence of thickness of the rectangular frustum-shaped light guide on photon transmission efficiency were investigated by HM. Park et. al. and reported in their publication. In their study, a software called LightTools Code utilizing Monte Carlo simulation of geometric ray tracing was used for analysis of the light propagation inside the light guides. The light guides with a reception area of $10\text{mm} \times 10\text{mm}$ and an exit window of $3\text{mm} \times 3\text{mm}$ were tested for different thicknesses between $1 - 10$ mm with 1 mm increments, as depicted in Figure 7.13 [58]. The results of this simulation was expressed in terms of the irradiance received by the exit window. The maximum photon transmission efficiency was obtained with the 4 mm light guide which has an acceptance angle of 49°, as depicted in Figure 7.14.

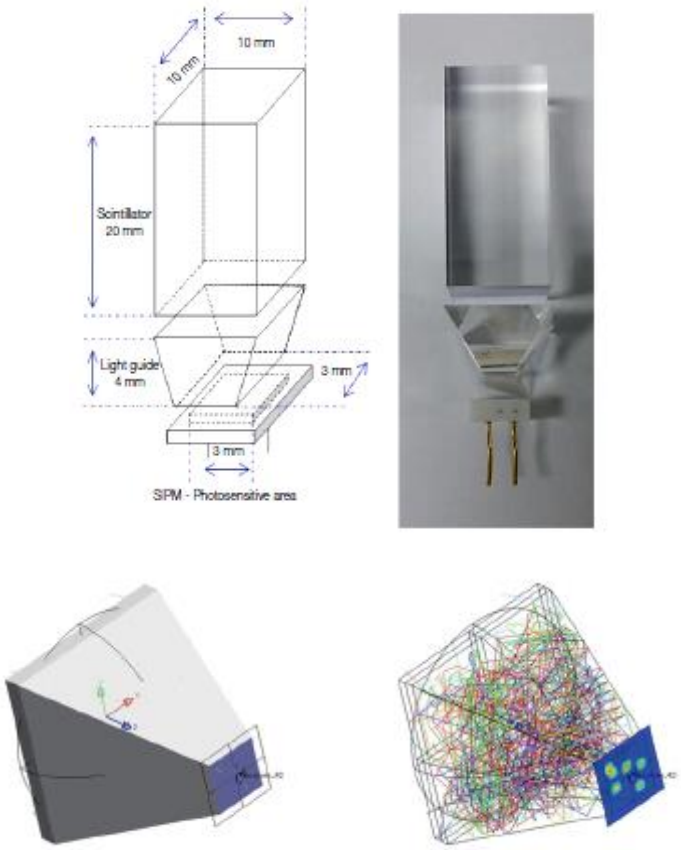

Figure 7.13: Geometric schematic and the picture of the scintillation detector tested by HM. Park et. al. (top) and modelling of the light guide design obtained using LightTools (bottom) [58].

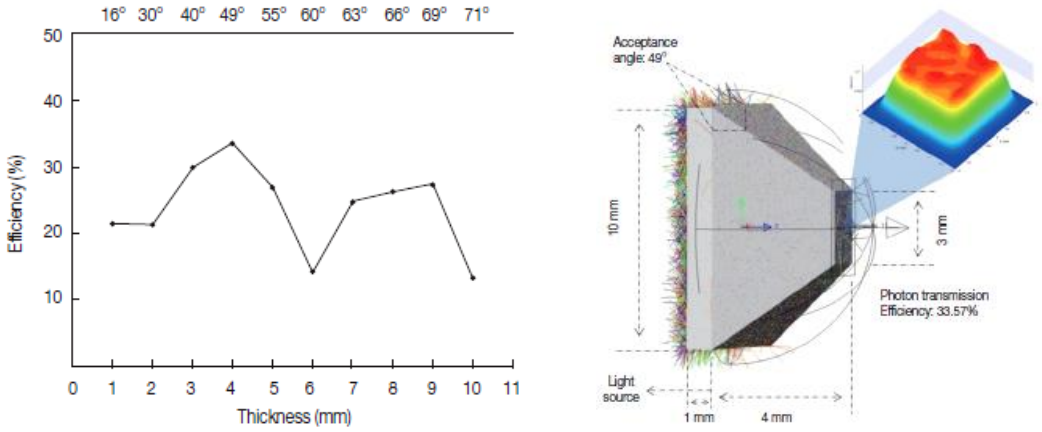

Figure 7.14: Simulation results obtained by HM. Park et. al.. Photon transmission efficiency for different acceptance angles (left) and the light guide transmitting the maximum irradiance at the exit window (right) [58].

The above-mentioned results were obtained with the Hamamatsu S12572-100C SiPM [58]. However, each model of SiPM has distinct angular response to incident light. In this thesis work, a more general method of evaluating the photon detection efficiency was explored based on geometric optical analysis of the propagation of light within the light guide. For simplicity of discussion, a simplified case is taken as an example, in which parallel light being transmitted to the light guide is assumed, in view of demonstrating how the PDE of a scintillation detector is influenced by the light guide geometry. The parallel light can be achieved by using a collimator similar as the parallel hole collimator of gamma cameras used in nuclear medical sciences [59] or the fiber collimator widely used in optical network designs [60]. As depicted in Figure 7.15, the randomly spreading light can be collimated into parallel light rays for higher performance of optical networks.

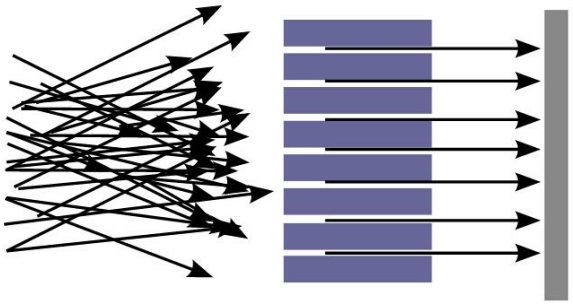

Figure 7.15: Randomly spreading light collimated by a fiber collimator [60].

The analysis was simplified to 2D regime. As illustrated in the schematics in Figure 7.16, the analysis was made with a light guide having thickness *t* which matches the size of the photosensor. The incident light rays are uniformly distributed over the entrance plane.

Figure 7.16: Schematic view of the scintillator with thickness matched to the photosensor size: 3D view of the geometry (left), 2D view of the parallel light entering the light guide (right).

The incoming light rays have different trajectories after entering the light guide, resulting in discrete contributions to the total light output depending on the angle of incidence on the exit window and the associated proportion of the total incoming light. As illustrated in the Figure 7.17, for an arbitrary 2D frustum-shaped light guide, schematics of the reflections shows different transmission channels of the incoming light and the corresponding cross section of each channel. By analysing the influences of varying geometric parameters on the contribution of each channel to the total output and summing up the individual contributions, the angular distribution of the light output can be extracted.

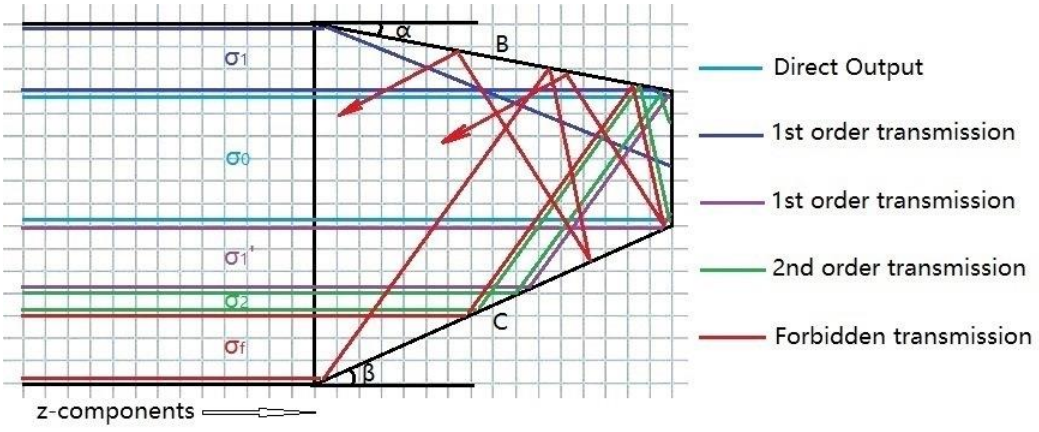

Figure 7.17: Different transmission channels and corresponding cross sections.

In Figure 7.17, the "0-order" reflection, i.e. direct output, 1st order transmission, i.e. output after one reflection, and 2nd order transmission, i.e. output after two reflections were demonstrated. Each channel has a bandwidth σ_i. Higher order reflections may occur when the light guide is excessively long, resulting in a requirement of large space inside the measurement chamber accordingly, or when the exit window is very small, producing poor light output. Likelihood of either case is very low in practice. Therefore, this model was developed based on the analysis up to the 3rd order transmission.

- Direct output

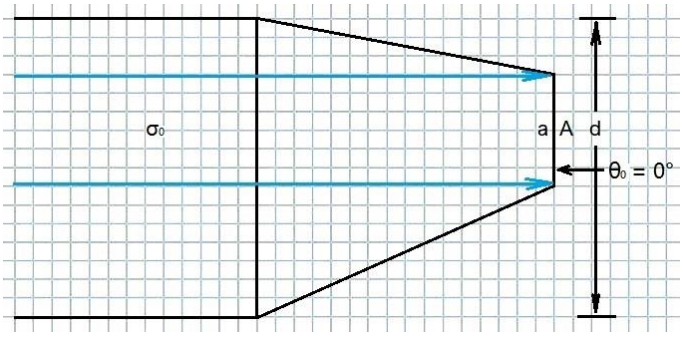

Figure 7.18: Schematics of direct output.

It is illustrated in Figure 7.18 that, as a result of direct output, the incidence angle on Plane A is $\theta_0 = 0°$, with a cross section $\sigma_0 = a \cdot t$ and a branching ratio $br_0 = a/d \cdot 100\%$, for t being the thickness of the light guide.

- 1st order transmission

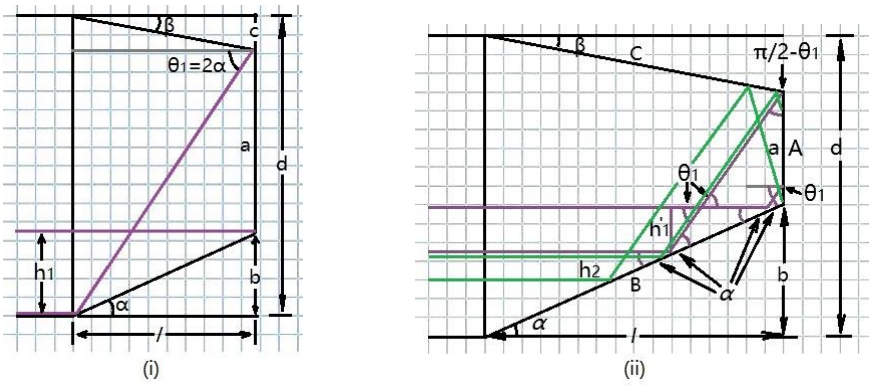

Figure 7.19: Schematic demonstration of the 1st order transmission: (i). 1st order band with 2nd band absent, (ii). Co-existence of 1st and 2nd order channels.

With the schematics in Figure 7.19, it can be derived using trigonometric rules that, for such kind of light guide geometry that has length l, entrance width d, and an exit with width a which is elevated by a height b, the contribution of a 1st order transmission channel at a surface tilted by an angle α to the light output has the following characteristics:

Output angle:

$$\theta_1 = 2\alpha = 2 \cdot \tan^{-1}\left(\frac{b}{l}\right) \tag{7.7}$$

It must be noted that, either reflecting surface which is tilted by an angle α will not carry any significance to the light output if $\pi/4 \leq \alpha \leq \pi/2$, as the incoming light component incident on this surface will be reflected back into the scintillator. Therefore, the angle of incidence on the exit window is more precisely defined by

$$\theta_1(\alpha): \begin{cases} = 2\alpha = 2\tan^{-1}\left(\frac{b}{l}\right), & \text{for } 0 < \alpha < \frac{\pi}{4} \\ \geq \frac{\pi}{2} \text{ (Forbidden)}, & \text{for } \frac{\pi}{4} \leq \alpha \leq \frac{\pi}{2} \end{cases} \tag{7.8}$$

Cross section of the 1st order transmission mode:

$$h_1 \cdot t = \begin{cases} b \cdot t, & \text{if } B_1(\alpha): \frac{l}{a} \leq \frac{1+\cos 2\alpha}{\tan 2\alpha} \\ \sin\theta_1 \cdot \frac{a \cdot t}{\tan\theta_1} = a \cdot t \cdot \cos 2\alpha, & \text{if } B_1(\alpha): \frac{l}{a} > \frac{1+\cos 2\alpha}{\tan 2\alpha} \end{cases} \tag{7.9}$$

where B_1 is the boundary condition which determines whether the band is lifted by subsequent higher order bands or not. Branching ratio of a 1st order transmission mode:

$$br_1 = \frac{h_1}{d} \cdot 100\% \tag{7.10}$$

It must be noted that, either surface *B* or *C* tilted by an angle less than $\pi/4$ will produce 1st order transmission. Therefore, the 1st order transmission may also have another branch:

$$\theta_1': \begin{cases} = 2\beta = 2\tan^{-1}\left(\frac{c}{l}\right), & \text{for } 0 < \beta < \frac{\pi}{4} \\ \geq \frac{\pi}{2} \text{ (Forbidden)}, & \text{for } \frac{\pi}{4} \leq \beta \leq \frac{\pi}{2} \end{cases} \tag{7.11}$$

and

$$br_1' = \frac{h_1'}{d} \cdot 100\% \tag{7.12}$$

- 2nd order transmission

In the case of 2nd order transmission, both reflecting surfaces tilted by angles α and β are involved. It can be proven that, after the incoming light is reflected in turn by the two surfaces, the direction of the output is the same as if it had undergone a single reflection by a surface tilted by an angle $\omega = \alpha + \beta$, as illustrated in Figure 7.20. Therefore, the 2nd order transmission occurs only if $\alpha + \beta < \pi/4$. This can be referred to as the superposition rule of reflections.

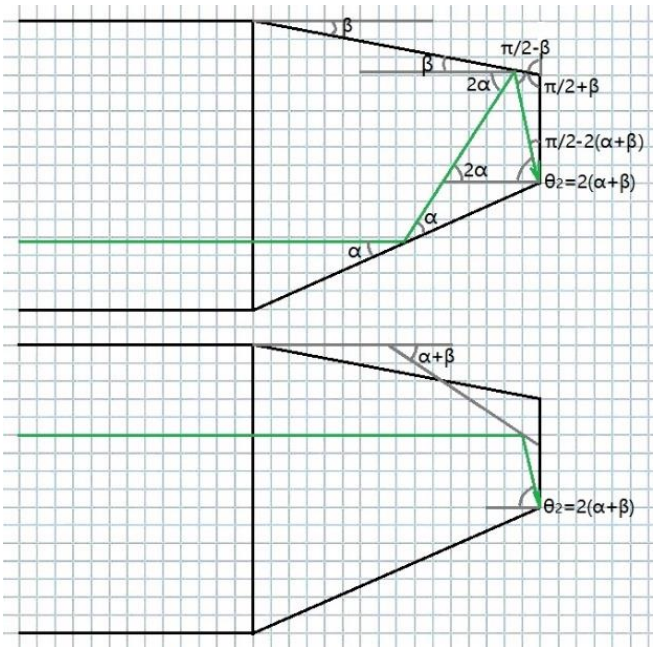

Figure 7.20: Schematics of the superposition rule of multiple reflections.

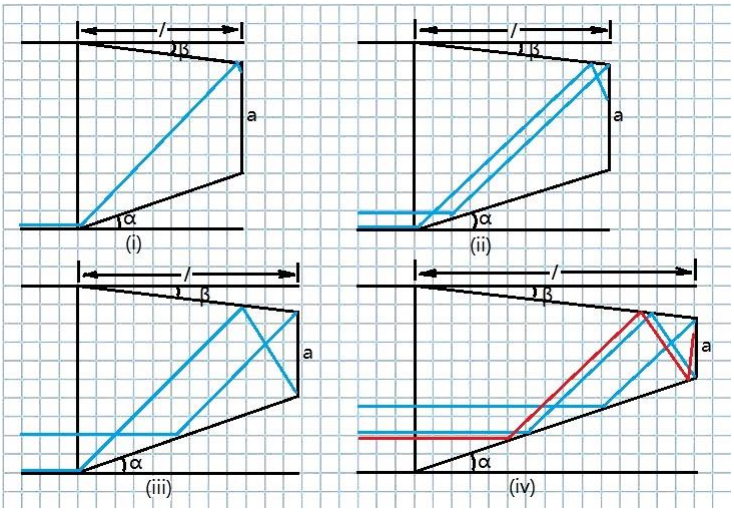

Figure 7.21: Behaviour dependence of the 2nd order channel on l/a ratio. (i): 2nd order channel occurs when B_1 is fulfilled. (ii): The bandwidth being created as l/a increases. (iii): The bandwidth of a 2nd order channel reaches the maximum when B_2 is fulfilled and the bandwidth starts to decrease. (iv): The 2nd order band is lifted up by subsequent higher order channel as l/a continues to increase.

The behaviour of the 2nd order transmission channel is more complicated. As depicted in Figure 7.21, 2nd order transmission occurs when the first boundary condition is fulfilled:

$$B_1(\alpha): \frac{l}{a} > \frac{1+\cos 2\alpha}{\tan 2\alpha} \tag{7.13}$$

or correspondingly,

$$B_1(\beta): \frac{l}{a} > \frac{1+\cos 2\beta}{\tan 2\beta} \tag{7.14}$$

As the l/a ratio increases, the bandwidth approaches the maximum, and tends to saturate on the output plane. The bandwidth starts to decrease and the band tends to be "lifted up" when the second boundary condition is fulfilled:

$$B_2(\alpha): \frac{l}{a} \geq \frac{1+\cos 2\alpha}{\tan 2\alpha} + \frac{b/a - \cos 2\alpha}{\tan \alpha} \tag{7.15}$$

or correspondingly,

$$B_2(\beta): \frac{l}{a} \geq \frac{1+\cos 2\beta}{\tan 2\beta} + \frac{c/a - \cos 2\beta}{\tan \beta} \tag{7.16}$$

In this case, as l/a continues to increase, the region of the incoming light below the lifted band would start to switch to a new band creating a 3rd order channel if $2\alpha + \beta < \pi/4$ or $2\beta + \alpha < \pi/4$. On the other hand, if the sum of the angles is no less than $\pi/4$, the lifted band would not be reflected onto the output window, as illustrated by the forbidden channel in Figure 7.17. It can be seen from Figure 7.21 (iv), when higher order transmission begins to dominate, the shape of the light guide is no longer practical.

The characteristics of light output contributed by 2nd order transmissions were derived as the follows:

Output angle:

$$\theta_2 : \begin{cases} = 2(\alpha + \beta), & \text{for } 0 < \alpha + \beta < \dfrac{\pi}{4} \\ \text{Forbidden}, & \text{for } \dfrac{\pi}{4} \leq \alpha + \beta \leq \pi \end{cases} \tag{7.17}$$

Cross section of the 2nd order transmission channel is given by:

$$h_2 \cdot t = \begin{cases} (b - a \cdot \cos 2\alpha) \cdot t, & \text{for } \dfrac{1 + \cos 2\alpha}{\tan 2\alpha} \leq \dfrac{l}{a} \leq \dfrac{1 + \cos 2\alpha}{\tan 2\alpha} + \dfrac{b/a - \cos 2\alpha}{\tan \alpha} \\ a \cdot t \cdot \cot[2(\alpha + \beta)] \sin 2\alpha, & \text{for } \dfrac{l}{a} > \dfrac{1 + \cos 2\alpha}{\tan 2\alpha} + \dfrac{b/a - \cos 2\alpha}{\tan \alpha} \end{cases}$$

(7.18)

and correspondingly,

$$h'_2 \cdot t = \begin{cases} (c - a \cdot \cos 2\beta) \cdot t, & \text{for } \dfrac{1 + \cos 2\beta}{\tan 2\beta} \leq \dfrac{l}{a} \leq \dfrac{1 + \cos 2\beta}{\tan 2\beta} + \dfrac{c/a - \cos 2\beta}{\tan \beta} \\ a \cdot t \cdot \cot[2(\alpha + \beta)] \sin 2\beta, & \text{for } \dfrac{l}{a} > \dfrac{1 + \cos 2\beta}{\tan 2\beta} + \dfrac{c/a - \cos 2\beta}{\tan \beta} \end{cases}$$

(7.19)

Branching ratio of the 2nd order transmission mode can be determined by:

$$br_2 = \begin{cases} \dfrac{(b - a \cdot \cos 2\alpha)}{d} \cdot 100\%, \text{for } \dfrac{1+\cos 2\alpha}{\tan 2\alpha} \leq \dfrac{l}{a} \leq \dfrac{1+\cos 2\alpha}{\tan 2\alpha} + \dfrac{b/a - \cos 2\alpha}{\tan \alpha} \\ \dfrac{a}{d} \cdot \cot(2\alpha + 2\beta) \sin 2\alpha \cdot 100\%, \quad \text{for } \dfrac{l}{a} > \dfrac{1+\cos 2\alpha}{\tan 2\alpha} + \dfrac{b/a - \cos 2\alpha}{\tan \alpha} \end{cases}$$

(7.20)

$$br_2' = \begin{cases} \dfrac{(c - a \cdot \cos 2\beta)}{d} \cdot 100\%, \text{for } \dfrac{1+\cos 2\beta}{\tan 2\beta} \leq \dfrac{l}{a} \leq \dfrac{1+\cos 2\beta}{\tan 2\beta} + \dfrac{c/a - \cos 2\beta}{\tan \beta} \\ \dfrac{a}{d} \cdot \cot(2\alpha + 2\beta) \sin 2\beta \cdot 100\%, \quad \text{for } \dfrac{l}{a} > \dfrac{1+\cos 2\beta}{\tan 2\beta} + \dfrac{c/a - \cos 2\beta}{\tan \beta} \end{cases}$$

(7.21)

The effect of higher order transmissions to the light output is insignificant as the output angles resulting from such channels are so large that count only a negligible contribution to the light generating a pulse, according to the angular response of the SiPM. In order that convenience of using this mathematical model can be maximized, complexity of involving higher order channels was avoided by evaluating the branching ratio of the 3rd order channels an approximation, rather than a detailed analysis. The 3rd order transmissions occur only if the following conditions are fulfilled:

$$2\alpha + \beta < \frac{\pi}{4} \text{ and } \frac{l}{a} \geq \frac{1+\cos 2\alpha}{\tan 2\alpha} + \frac{b/a - \cos 2\alpha}{\tan \alpha} \text{ simultaneously} \quad (7.22)$$

or correspondingly,

$$2\beta + \alpha < \frac{\pi}{4} \text{ and } \frac{l}{a} \geq \frac{1+\cos 2\beta}{\tan 2\beta} + \frac{c/a - \cos 2\beta}{\tan \beta} \text{ simultaneously} \quad (7.23)$$

As depicted in Figure 7.21 (iii) and (iv), right after a 2nd order channel saturates on the output plane as the second boundary condition B_2 is satisfied by the l/a ratio, the 3rd order channel starts to occur and tends to lift the 2rd order channel up. The bandwidth of the 3rd order channel can be approximated as the maximum 2nd bandwidth multiplied by the degree to which the l/a ratio

satisfies B_2 (i.e. $l/a - \frac{1+\cos 2\alpha}{\tan 2\alpha} + \frac{b/a-\cos 2\alpha}{\tan \alpha}$), since the larger the difference, the wider 3rd order band would be created:

$$h_3(\alpha) = a \cdot \cot[2(\alpha+\beta)] \sin 2\alpha \cdot \frac{\frac{l}{a} - \frac{1+\cos 2\alpha}{\tan 2\alpha} + \frac{b/a-\cos 2\alpha}{\tan \alpha}}{\frac{1+\cos 2\alpha}{\tan 2\alpha} + \frac{b/a-\cos 2\alpha}{\tan \alpha}} \cdot 100\% \tag{7.24}$$

$$h_3(\beta) = a \cdot \cot[2(\alpha+\beta)] \sin 2\beta \cdot \frac{\frac{l}{a} - \frac{1+\cos 2\beta}{\tan 2\beta} + \frac{c/a-\cos 2\beta}{\tan \beta}}{\frac{1+\cos 2\beta}{\tan 2\beta} + \frac{c/a-\cos 2\beta}{\tan \beta}} \cdot 100\% \tag{7.25}$$

The resulting output angle contributed by a 3rd order transmission is

$$\theta_3(\alpha) = 2(2\alpha+\beta) \tag{7.26}$$

and correspondingly,

$$\theta_3(\beta) = 2(2\beta+\alpha) \tag{7.27}$$

These expressions also indicate the path of the band being reflected between the two reflecting surfaces. For example, referring to the drawing in Figure 7.17, Eq. (7.26) corresponds to the 3rd order band being reflected twice by Surface *B* (tilted by α) and once by Surface *C* (tilted by β) before reaching the output plane.

7.3 Evaluation and optimization of relative PDE

With the angular response of a photodetector examined showing the relative PDE $\eta_{\text{rel.}}(\theta_i)$ as a function of angle of incidence, the obtained characterization curve facilitates evaluating and comparing the relative PDE of different

detector configurations by setting $\eta_{\text{rel.}}(0°)$ to be a standard value, e.g. 100%. With the geometrical parameters of the light guide as discussed specified, based on the above analysis, the relative PDE can be determined by

$$\eta_{\text{rel.}} = \sum_{i=0}^{3} \eta_i\,(\theta_i) \cdot br_i \cdot \delta_i \tag{7.28}$$

where $\eta_i(\theta_i)$ is the discrete relative PDE corresponding to the output angle of a particular channel, which can be obtained from the response curve measured for the photodetector. br_i is the corresponding branching ratio of this channel, and δ_i is an identifying factor that identifies the authenticity of the i^{th} term and regulates the form of the model depending on the l/a ratio. For example, if the boundary condition $B_2(\alpha)$ is not fulfilled with a reflecting surface tilted by the angle α, 2nd order transmission of a band which is first reflected by this surface is forbidden. Then the 2nd order term related to this surface will be cancelled by δ_2 in the calculation. The bandwidth and thereby the branching ratio are determined with different formulae depending on the l/a ratio. The correct approach is selected by δ_i, accordingly. And then, the calculation of the relative PDE can be summarized into a general form given by Eq. (7.29):

$$\begin{aligned}\eta_{\text{rel.}} = \frac{a}{d}\Big[&\eta(0°) + b\eta(2\alpha)\delta_1^{\alpha} + c\eta(2\beta)\delta_1^{\beta} \\ &+ \cot(2\alpha+2\beta)\eta(2\alpha+2\beta)\cdot\left(\sin 2\alpha\cdot\delta_2^{\alpha} + \sin 2\beta\cdot\delta_2^{\beta}\right) \\ &+ \cot\left[2(\alpha+\beta)\right]\sin 2\alpha\,\eta(4\alpha+2\beta)\frac{\frac{l}{a} - \frac{1+\cos 2\alpha}{\tan 2\alpha} + \frac{b/a-\cos 2\alpha}{\tan\alpha}}{\frac{1+\cos 2\alpha}{\tan 2\alpha} + \frac{b/a-\cos 2\alpha}{\tan\alpha}}\delta_3^{\alpha} \\ &+ \cot\left[2(\alpha+\beta)\right]\sin 2\beta\,\eta(4\beta+2\alpha)\frac{\frac{l}{a} - \frac{1+\cos 2\beta}{\tan 2\beta} + \frac{c/a-\cos 2\beta}{\tan\beta}}{\frac{1+\cos 2\beta}{\tan 2\beta} + \frac{c/a-\cos 2\beta}{\tan\beta}}\delta_3^{\beta}\Big]\cdot 100\%\end{aligned} \tag{7.29}$$

where the identifying factors are defined as

$$\delta_1^{\alpha} = \begin{cases} \frac{1}{a}, & \text{if } 0 < \alpha < \frac{\pi}{4} \text{ and } \frac{l}{a} \leq \frac{1+\cos 2\alpha}{\tan 2\alpha} \\ \frac{\cos 2\alpha}{b}, & \text{if } 0 < \alpha < \frac{\pi}{4} \text{ and } \frac{l}{a} > \frac{1+\cos 2\alpha}{\tan 2\alpha} \\ 0, & \text{Otherwise} \end{cases} \tag{7.30}$$

$$\delta_1^{\beta} = \begin{cases} \frac{1}{a}, & \text{if } 0 < \beta < \frac{\pi}{4} \text{ and } \frac{l}{a} \leq \frac{1+\cos 2\beta}{\tan 2\beta} \\ \frac{\cos 2\beta}{c}, & \text{if } 0 < \beta < \frac{\pi}{4} \text{ and } \frac{l}{a} > \frac{1+\cos 2\beta}{\tan 2\beta} \\ 0, & \text{Otherwise} \end{cases} \tag{7.31}$$

$$\delta_2^{\alpha} = \begin{cases} \frac{\frac{b}{a} - \cos 2\alpha}{\cot(2\alpha + 2\beta)\sin 2\alpha}, & \text{if } \frac{1+\cos 2\alpha}{\tan 2\alpha} \leq \frac{l}{a} \leq \frac{1+\cos 2\alpha}{\tan 2\alpha} + \frac{\frac{b}{a} - \cos 2\alpha}{\tan \alpha} \\ 1, & \text{if } \frac{l}{a} > \frac{1+\cos 2\alpha}{\tan 2\alpha} + \frac{\frac{b}{a} - \cos 2\alpha}{\tan \alpha} \\ 0, & \text{if } \alpha + \beta > \frac{\pi}{4} \end{cases} \tag{7.32}$$

$$\delta_2^{\beta} = \begin{cases} \frac{\frac{c}{a} - \cos 2\beta}{\cot(2\alpha + 2\beta)\sin 2\beta}, & \text{if } \frac{1+\cos 2\beta}{\tan 2\beta} \leq \frac{l}{a} \leq \frac{1+\cos 2\beta}{\tan 2\beta} + \frac{\frac{c}{a} - \cos 2\beta}{\tan \beta} \\ 1, & \text{if } \frac{l}{a} > \frac{1+\cos 2\beta}{\tan 2\beta} + \frac{\frac{c}{a} - \cos 2\beta}{\tan \beta} \\ 0, & \text{if } \alpha + \beta > \frac{\pi}{4} \end{cases} \tag{7.33}$$

$$\delta_3^{\alpha} = \begin{cases} 1, & \text{if } 0 < 2\alpha + \beta < \frac{\pi}{4} \text{ and } \frac{l}{a} > \frac{1+\cos 2\alpha}{\tan 2\alpha} + \frac{\frac{b}{a} - \cos 2\alpha}{\tan \alpha} \\ 0, & \text{Otherwise} \end{cases} \tag{7.34}$$

$$\delta_3^{\beta} = \begin{cases} 1, & \text{if } 0 < 2\beta + \alpha < \frac{\pi}{4} \text{ and } \frac{l}{a} > \frac{1+\cos 2\beta}{\tan 2\beta} + \frac{\frac{c}{a} - \cos 2\beta}{\tan \beta} \\ 0, & \text{Otherwise} \end{cases} \tag{7.35}$$

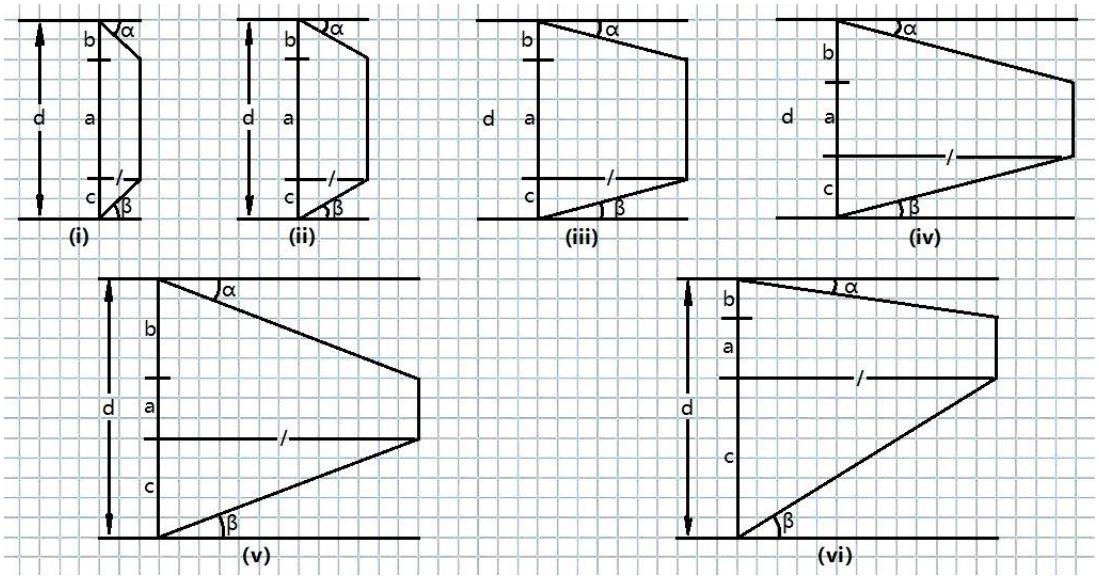

Figure 7.18: Tested light guide geometries for comparison.

Six contrasting light guide geometries were examined for comparisons of the corresponding relative photon detection efficiency, as depicted in Figure 7.18. The geometrical parameters of each tested geometry and the relative PDE $\eta_{\text{rel.}}$ predicted by this formalism are presented in Table 7.2. The SiPM angular response curve obtained in my measurement was used as an example and the calculations with Geometry (v) is presented as the follows to demonstrate the usage of this mathematical formalism:

The direct output has an angle of 0°. Both α and β are less than $\pi/4$, there are two 1st order channels. The resultant output angles are $\theta_1(\alpha) = \theta_1(\beta) = 30°$ according to Eq. (7.8) and (7.11).

The first boundary conditions $B_1(\alpha)$ and $B_1(\beta)$ are fulfilled (denoted by ">" in Table 7.2) according to Eq. (7.13) and (7.14), whereas the second boundary conditions were not (denoted by "<") according to Eq. (7.15) and (7.16), which yields:

$$\frac{1+\cos 2\alpha}{\tan 2\alpha} < \frac{l}{a} < \frac{1+\cos 2\alpha}{\tan 2\alpha} + \frac{b/a - \cos 2\alpha}{\tan \alpha}$$

and

$$\frac{1+\cos 2\beta}{\tan 2\beta} < \frac{l}{a} < \frac{1+\cos 2\beta}{\tan 2\beta} + \frac{c/a - \cos 2\beta}{\tan \beta}$$

This means that there are two 2nd order transmission channels contributing to an output angle of 60° according to Eq. (7.17). According to Eq. (7.30) – (7.33), the identifying factors for these channels would take the forms:

$$\begin{cases} \delta_1^{\alpha} = \dfrac{\cos 2\alpha}{b} \\ \delta_1^{\beta} = \dfrac{\cos 2\beta}{c} \end{cases}$$

and

$$\begin{cases} \delta_2^{\alpha} = \dfrac{\dfrac{b}{a} - \cos 2\alpha}{\cot(2\alpha + 2\beta)\sin 2\alpha} \\ \delta_2^{\beta} = \dfrac{\dfrac{c}{a} - \cos 2\beta}{\cot(2\alpha + 2\beta)\sin 2\beta} \end{cases}$$

These identifying factors can be calculated using the geometric parameters listed in Table 7.2. Since both $2\alpha + \beta$ and $2\beta + \alpha$ are no less than $\pi/4$, 3rd order transmission is forbidden and $\delta_3^{\alpha} = \delta_3^{\beta} = 0$ according to Eq. (7.34) and (7.35).

The response of the SiPM corresponding to each output angle can be obtained using the angular response curve. And then, substituting the response values and calculated identifying factors into Eq. (7.29) yields the overall relative PDE which can be obtained with this geometry.

Table 7.2: Geometrical parameters and calculated $\eta_{\text{rel.}}$.

Parameter	Geometry					
	i	ii	iii	iv	v	vi
a (mm)	6	6	6	6	6	6
b (mm)	2	2	2	5.23	7	4
c (mm)	2	2	2	5.23	7	10
d (mm)	10	10	10	16.46	20	20
l (mm)	2	3.46	7.46	19.52	26.1	26.1
α (°)	45	30	15	15	15	9
β (°)	45	30	15	15	15	21
$\theta_1(\alpha)$ (°)	Forbidden	60	30	30	30	18
$\theta_1(\beta)$ (°)	Forbidden	60	30	30	30	42
$B_1(\alpha)$	$-$	$<$	$<$	$>$	$>$	$>$
$B_1(\beta)$	$-$	$<$	$<$	$>$	$>$	$>$
$B_2(\alpha)$	$-$	$-$	$-$	$>$	$<$	$>$
$B_2(\beta)$	$-$	$-$	$-$	$>$	$<$	$-$
$\theta_2(\alpha)$ (°)	Forbidden	Forbidden	Forbidden	60	60	60
$\theta_2(\beta)$ (°)	Forbidden	Forbidden	Forbidden	60	60	60
$\theta_3(\alpha)$ (°)	Forbidden	Forbidden	Forbidden	Forbidden	Forbidden	78
$\theta_3(\beta)$ (°)	Forbidden	Forbidden	Forbidden	Forbidden	Forbidden	Forbidden
$\delta_1(\alpha)$	0	$\frac{1}{a}$	$\frac{1}{a}$	$\frac{\cos 2\alpha}{b}$	$\frac{\cos 2\alpha}{b}$	$\frac{1}{a}$
$\delta_1(\beta)$	0	$\frac{1}{a}$	$\frac{1}{a}$	$\frac{\cos 2\beta}{c}$	$\frac{\cos 2\beta}{c}$	$\frac{\cos 2\beta}{c}$
$\delta_2(\alpha)$	0	0	0	1	$\frac{\frac{b}{a}-\cos 2\alpha}{\cot(2\alpha+2\beta)\sin 2\alpha}$	1
$\delta_2(\beta)$	0	0	0	1	$\frac{\frac{c}{a}-\cos 2\beta}{\cot(2\alpha+2\beta)\sin 2\beta}$	1
$\delta_3(\alpha)$	0	0	0	0	0	1
$\delta_3(\beta)$	0	0	0	0	0	0
$\eta_{\text{rel.}}$ (%)	60.9	74.3	87.9	89.2	71.6	62.5
Values of $\eta(\theta)$ normalized by: $\eta(0°) = 100\%$						
SiPM angular response: $\eta(\theta) = (-1.13619\theta + 101.57143)\%$						

As presented in Table 7.2, the relative PDE $\eta_{\text{rel.}}$ calculated using this formalism could predict a qualitative comparison between different geometries of light guides:

- With the same entrance and exit areas, a light guide with reflective surfaces tilted by a smaller angle has more effective light collection (i vs. ii vs. iii).
- If the reflective surfaces are tilted by a small angle, the light collection is not significantly altered by varying area of the entrance gate and l/a ratio (iii vs. iv).
- Since the resultant incidence angle contributed by transmissions of different orders differ significantly, the greater the l/a ratio satisfies B_1 and B_2 when each boundary condition is fulfilled, the less efficient light collection would be obtained. This means that the more significantly higher order channels dominate, the more the photon detection efficiency is reduced.
- The contribution of higher order channels to the relative PDE is insignificant due to the angular response of the photodetector to small angles of incidence. For Geometry (vi), where 3rd order transmission was present, the contribution of the 3rd order transmission amounted to 0.023%.

A practical fact is that, due to space utility issues, the light guide sometimes needs to be designed in an asymmetric geometry. The arbitrary geometry (vi) in Figure 7.18 was evaluated as an example. Moreover, geometrically, there is another special case called the off-axis geometry, where the two tilted surfaces of the light guide have projections on the axis of the scintillator with lengths differing from each other. This geometry is not practically beneficial and was excluded in this analysis.

This mathematical model for estimating the relative photon detection efficiency of scintillator-based detectors which have 2D rectangular frustum-shaped light guides was developed for use in certain conditions. The refractive index must be uniform between the lightguide and the scintillator, so that refractions

would not occur when light enters the light guide. The light guide needs to be covered by specular reflectors at all reflecting surfaces providing total internal reflections and the light propagation would not be violated by diffusions.

In the case of uniform parallel light rays being transmitted to a 2D rectangular frustum-shaped light guide, a high accuracy in determination of the relative PDE can be achieved using this method. For example, in large-sized scintillator, an aluminium grid with fine and dense parallel holes can be employed as a collimator at the entrance of the light guide, where uniformity of flux density is achievable and loss of intensity due to collimation can be neglected.

8. Conclusions and Outlook

A radiation detector was designed with plastic scintillator coupled to the SiPM. The properties of the detector were studied. The detector showed a fairly sensitive response to α, electron, and γ radiations.

The energy resolution of the detector in response to the 5.5 MeV α particles from the ^{241}Am source was $\sim 45\%$ without external reflective foil. With the reflective foil light collection was enhanced by a factor of ~ 3. Due to the collimation effect of the hole on the foil, the energy resolution was determined to be $\sim 20\%$ which was about half of that obtained without external reflector. A significant decrease in counting rate and a dramatic statistical fluctuation were observed with the effects of collimation.

The pulse shape discrimination property of the detector was studied with the slow scintillation material ZnS(Ag). The slow and fast signals produced respectively by alphas and gammas were clearly distinguishable with this detector, as expected. The timing properties in slow and fast signal generations were compared that, the rise time of the fast signal produced by electrons and gammas was measured by the plastic scintillator to be 116.7 ns, whereas the rise time of the slow signal produced by alphas was measured with the ZnS(Ag) to be 140 ns. The time for 100% decay of the maximum pulse amplitude of the fast signal was 700 ns, while the slow signal took 1283.3 ns for 100% decay of its maximum pulse amplitude. A comparison of the timing properties between the plastic scintillator and ZnS material in response to α particles was obtained as well that, the rise time of 110 ns and the 100% decay time of 800 ns were measured with the plastic scintillator. When planning a thin layer of ZnS(Ag) on the plastic scintillator for α particle and other heavy ion detection, one must take into account the opacity of this polycrystalline layer to its own luminescence. Commonly, thicknesses greater than 25 mg/cm^2 will become inefficient [61].

The γ detection performance was studied with the ^{137}Cs and ^{60}Co source. The Compton edges of the 661.7 keV γ rays from ^{137}Cs and the $(1173 - 1332)$ keV γ ray burst from ^{60}Co were calculated to be 476.7 keV and 1040.9 keV, by which an energy calibration was achieved with the measured spectra. The effect of increasing scintillator thickness on γ detection was studied by using a thicker scintillator, which showed a greater counting rate and light yield resulting from the higher interaction probability of the larger volume. However, due to the different photon detection efficiencies resulting from the geometrical difference of the light guides, the light yield was slightly enhanced by the larger volume. In addition, it was also implied by the slight difference in the light yield and counting rate in different volumes that, most γ rays could have penetrated through the 10 mm thick scintillators without interaction at all.

Study of the detector response to fast electrons was done with a ^{207}Bi source. The Compton edges at 393.3 keV and 857.7 keV were well defined in good agreement with the obtained energy calibration. The relatively low emission rate of the ~ 1 MeV conversion electrons brought a difficulty to identifying the electron peaks from the spectrum. Nevertheless, the scintillator detector will be used in an array configuration in correlation techniques with the DSSD, rather than operated as an isolated detector in the future β tagging experiments [5]. In order to get the β particles having up to 10 MeV of energy completely stopped within the scintillator, the scintillator array was planned to consist of eight frontal pieces of 128×6×10 mm^3 scintillator in X-direction which would face the reaction products and thirteen pieces of 48×24×10 mm^3 scintillators behind, in Y-direction. This detector configuration will be used to replace the planar Ge-detector and work in correlation techniques with the position sensitive DSSD for recoil-β tagging. The DSSD has 192 strips in X-axis and 72 strips in Y-axis, with a width of 0.67 mm in each strip. Attributing to the matrix of 13824 pixels with a pixel size ~ 0.45 mm^2, the DSSD is highly position sensitive. Since γ rays will leave nearly zero energy on the DSSD at this thickness, when a fusion recoil is implanted in a pixel on the DSSD, its β decay

can be identified by the DSSD. The emitted β particle will leave part of its energy in the pixel, therefore, the scintillator array mounted behind the DSSD will be assigned to detect the rest of the energy of the β particles. When an energetic β particle interacts with both layers of the scintillator bars in X and Y axis, demanding a coincidence between the X and Y scintillator bars would allow defining the interaction position of the β particle in addition to its full energy measurement. Then the β tagging can be achieved by means of the prompt coincidence between the DSSD and the scintillator.

A similar correlation technique was studied by a simulation with cosmic muons. Coincidences between the two scintillators were identified by requiring the data acquisition system to collect the events registered simultaneously by the two detectors. The relation between the penetration depth and the energy released by the muons was studied as a simulation of β particle detection.

The geometrical efficiency of the individual 10 mm × 128 mm scintillator bar was calculated to be $\varepsilon_{\mathrm{geo}} = 7.6\%$. The absolute and intrinsic efficiencies were determined to be $\epsilon_{\mathrm{abs}} = 0.88\,\%$ and $\epsilon_{\mathrm{int}} = 11.6\,\%$, respectively. When the scintillator bars are combined in the future detector array, the corresponding efficiencies will be multiplied.

In the identification of the conversion electrons using ^{207}Bi source, the energy peaks of the ~ 1 MeV electrons were not distinguishable from the gammas due to the relatively low intensity of the IC decay modes compared to γ emission. In this situation, the conversion electrons can be identified indirectly. After the energy spectrum produced by γ photons and conversion electrons is measured, another measurement can be performed using an aluminium electron screener, so that the spectrum produced purely by gammas can be measured. And then, by applying certain spectrum subtraction algorithm with the two measured spectra and some correction for the γ-ray attenuation caused by the electron screener, the energy spectrum resulting from the conversion electrons can be obtained [52].

For any size of photosensor, the hosting circuit board is nearly always larger than the photosensor in all dimensions. When designing an array of scintillator bars which are planned to be coupled gaplessly with each other, the orientation of the SiPMs must be taken into account, such that the SiPM devices can be fitted in an array as well. The SensL MICROFC-SMTPA-60035 SiPM has a circuit board of 14 mm × 9 mm. Therefore, the scintillators must be fabricated with a width greater than 9 mm to be organized into an array.

Last but not least, the main aim of this work was to determine the optimal light guide geometry by which the photon detection efficiency in radiation detection of the detector would be optimized. Due to the practical issues discussed in Chapter 7, a difficulty arose in extracting a realistic result from the measured data. Nevertheless, a method for evaluation and optimization of the photon detection efficiency associated with light guide geometry was explored and demonstrated based on the geometrical optical analysis. This formalism was developed under the assumption that the incoming light was parallel and uniformly distributed over the scintillator volume. In practice, the light entering the light guide is randomly distributed, therefore, this formalism can be used to obtain a qualitative comparison between different geometries of light guide. By evaluating and comparing the six contrasting geometries as an example using this method, rather reasonable conclusions were extracted. However, in the parallel light applications, an accurate numerical evaluation of the relative PDE of a detector can be obtained using this formalism. In the future researches of scintillation detector, it would be interesting to perform a more accurate characterization of the SiPM angular response using a better measurement setup and extract the angular distribution of the light guide output with a higher accuracy by computer simulations.

Appendix A: Physical parameters of EJ-24x scintillators

Table A-1: Physical parameters of EJ-24x scintillators adapted from [22].

PROPERTIES	EJ-244	EJ-248	EJ-244M	EJ-248M
Light Output (% Anthracene)	56	60	56	60
Scintillation Efficiency (photons/1 MeV e^-)	8,600	9,200	8,600	9,200
Wavelength of Maximum Emission (nm)	434	425	434	425
Light Attenuation Length (cm)	270	250	270	250
Rise Time (ns)	1.0	0.9	1.0	0.9
Decay Time (ns)	3.3	2.1	3.3	2.1
Pulse Width, FWHM (ns)	4.2	2.5	4.2	2.5
H Atoms per cm³ ($\times 10^{22}$)	5.18	5.18	5.18	5.18
C Atoms per cm³ ($\times 10^{22}$)	4.69	4.69	4.69	4.69
Electrons per cm³ ($\times 10^{23}$)	3.34	3.34	3.34	3.34
Density (g/cm³)	1.023	1.023	1.023	1.023
Polymer Base	Polyvinyltoluene			
Refractive Index	1.58			
Softening Point	99°C			
Vapor Pressure	Vacuum-compatible			
Coefficient of Linear Expansion	7.8×10^{-5} below 70°C			
Temperature Range	-20°C to 90°C*			
Light Output (L.O.) vs. Temperature	At 60°C, L.O. = 95% of that at 20°C At 90°C, L.O. = 87% of that at 20°C No change from -60°C to 20°C			

Appendix B: Technical details of the SMTPA-60035 SiPM

Table B-1: Technical specifications of the SMTPA-60035 SiPM, edited from [39].

Dimensions	Sensor size: 6 mm		Microcell size: 35 μ	
Parameter (at 21°C)		Min.	Typ.	Max.
V_{br} (V)		24.2		24.7
Recommended V_o (V)		1.0		5.0
Spectral range (nm)		300		950
Peak wavelength (nm)		420		
PDE at λ_p (%)	V_{br} + 2.5 V	31		
	V_{br} + 5.0 V	41		
Gain	V_{br} + 2.5 V	3×10^6		
Rise time (ns) Fast Output		1.0		
Signal Pulse Width (ns) Fast Output (FWHM)		3.2		
Microcell recharge τ (ns)		95		
Capacitance (pF) Anode - Cathode	V_{br} + 2.5 V	3400		
Capacitance (pF) Fast terminal - Cathode		48		
T-dependence of V_{br} (mV/°C)		21.5		
T-dependence of Gain (%/°C)		-0.8		
Dark Current (nA)	V_{br} + 2.5 V		618	1750
Dark Count Rate (kHz)			1200	3400
Crosstalk (%)		7		
Afterpulsing (%)		0.2		

Appendix C: Gamma mass attenuation coefficients of PVT

Table C-1: Mass attenuation coefficient & energy absorption coefficient of vinyl toluene – type plastics for a typical set of γ photon energy [47].

Energy (MeV)	μ/ρ (cm^2/g)	μ_{en}/ρ (cm^2/g)
1.00000E-03	2.024E+03	2.022E+03
1.50000E-03	6.409E+02	6.397E+02
2.00000E-03	2.770E+02	2.760E+02
3.00000E-03	8.270E+01	8.203E+01
4.00000E-03	3.461E+01	3.407E+01
5.00000E-03	1.753E+01	1.707E+01
6.00000E-03	1.005E+01	9.650E+00
8.00000E-03	4.220E+00	3.883E+00
1.00000E-02	2.204E+00	1.903E+00
1.50000E-02	7.705E-01	5.158E-01
2.00000E-02	4.358E-01	2.059E-01
3.00000E-02	2.647E-01	6.210E-02
4.00000E-02	2.194E-01	3.256E-02
5.00000E-02	1.997E-01	2.424E-02
6.00000E-02	1.881E-01	2.180E-02
8.00000E-02	1.736E-01	2.172E-02
1.00000E-01	1.635E-01	2.310E-02
1.50000E-01	1.458E-01	2.650E-02
2.00000E-01	1.331E-01	2.876E-02
3.00000E-01	1.155E-01	3.110E-02
4.00000E-01	1.034E-01	3.197E-02
5.00000E-01	9.443E-02	3.218E-02
6.00000E-01	8.732E-02	3.204E-02
8.00000E-01	7.668E-02	3.128E-02
1.00000E+00	6.894E-02	3.027E-02
1.25000E+00	6.166E-02	2.894E-02
1.50000E+00	5.611E-02	2.766E-02
2.00000E+00	4.810E-02	2.542E-02
3.00000E+00	3.848E-02	2.214E-02
4.00000E+00	3.282E-02	1.992E-02
5.00000E+00	2.907E-02	1.835E-02
6.00000E+00	2.641E-02	1.718E-02
8.00000E+00	2.290E-02	1.558E-02
1.00000E+01	2.069E-02	1.455E-02
1.50000E+01	1.770E-02	1.309E-02
2.00000E+01	1.624E-02	1.236E-02

Appendix D: Schematics of the scintillator geometry

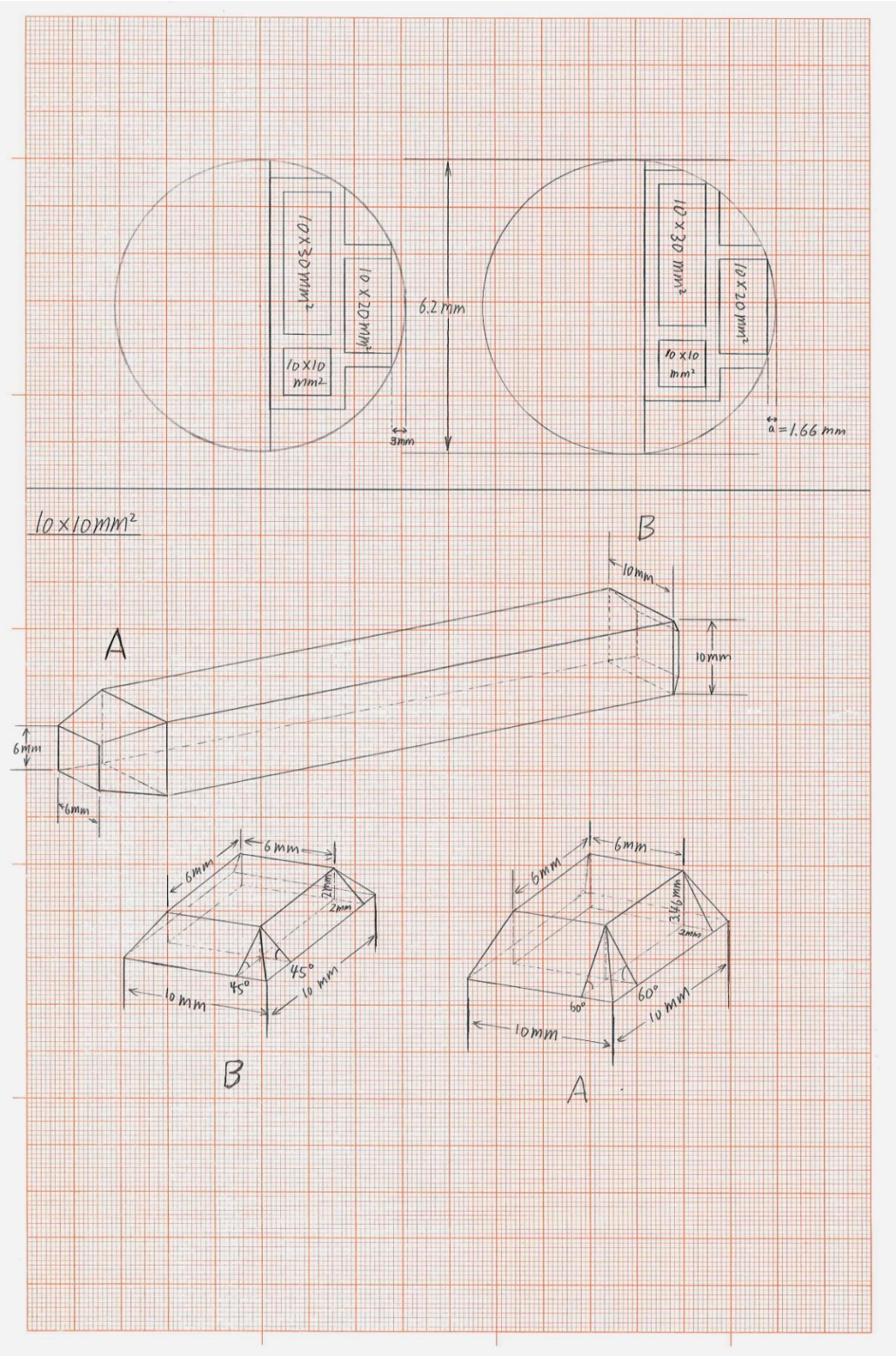

Figure D-1: Segmentation of the original plastic and the geometry of Scintillator 1.

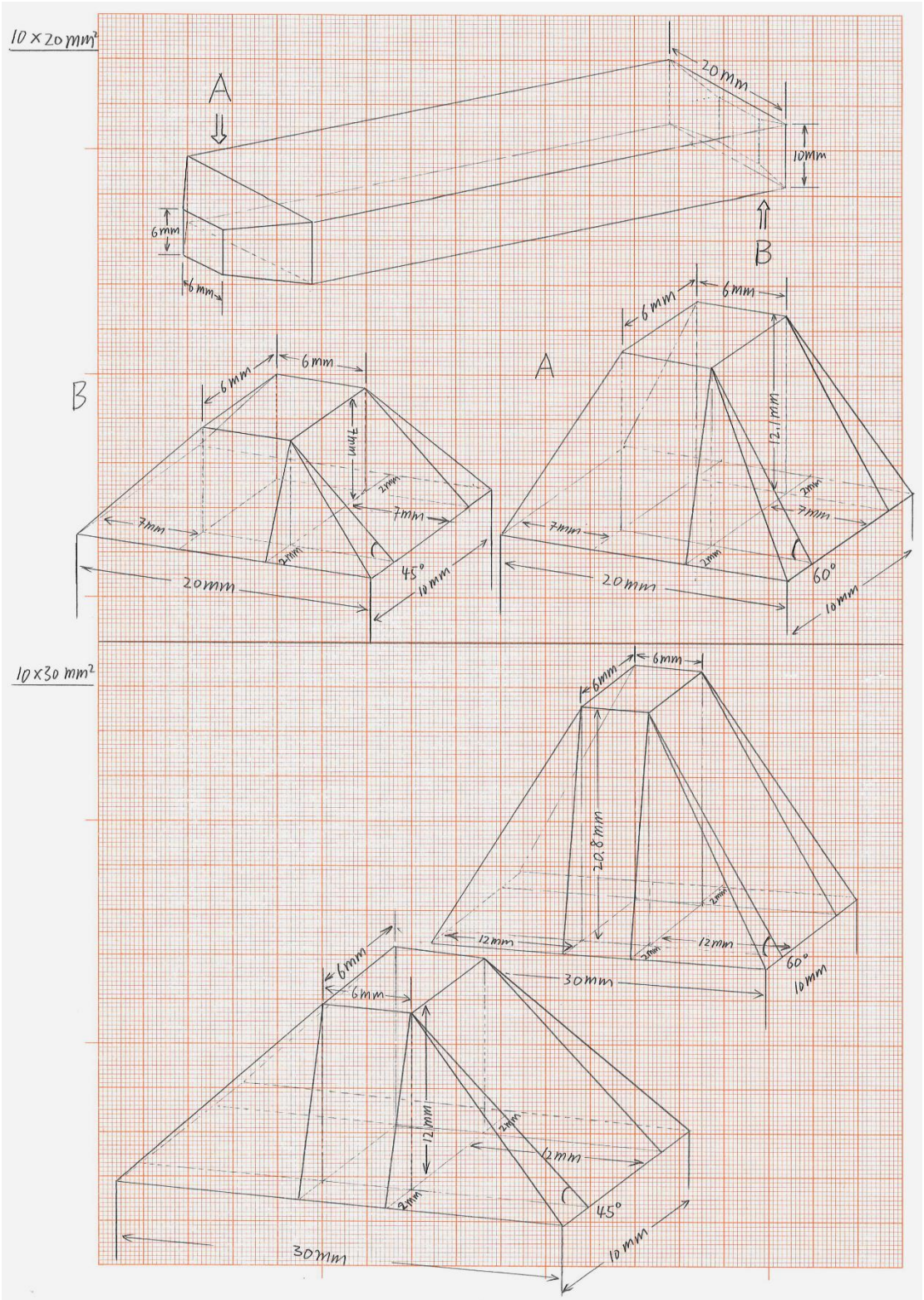

Figure D-2: The geometrical schematics of Scintillator 2 and 3.

Appendix E: Justification of the electron ranges

The energies of the conversion electrons related to the decay of ^{207}Bi are ~1 MeV, mainly 975.65 keV (8.36%) and 1047.8 keV (2.11%) [54]. The maximum range of these electrons can be determined by using Eq. (3.26):

$$R_{\max}\ [\mathrm{g/cm^2}] = \begin{cases} 0.412E_{\beta}^{1.265-0.0954\ln(E_{\beta})}, & for\ 0.01 \le E_{\beta} \le 2.5\mathrm{MeV} \\ 0.530E_{\beta} - 0.106, & for\ E_{\beta} > 2.5\mathrm{MeV} \end{cases}$$

$$\Longrightarrow R_{\mathrm{max@1MeV}} \approx 0.412\ \mathrm{g/cm^2}$$

The collimator was made of the pinewood of a density ~0.47 g/cm^3 [62], which gave an estimate of the electron maximum range through the collimator with the calculated $R_{\max}$, $R \approx 0.88$ cm. The collimator was 15 mm thick with 34 × 38 mm^2 cross-sectional area, so that only the electrons emitted through the 15 mm tunnel were incident at the selected points on the scintillator with full energy.

Density of the scintillator was 1.023 g/cm^3, which yields $R \approx 0.403$ cm in the scintillator. This is consistent with the electron range predicted by Figure 3.9. Therefore, the 1 MeV conversion electrons were stopped in the 10 mm × 10 mm scintillator with the full energy deposited.

Appendix F: Activities and decay schemes for the sources

The activities were calculated according to Eq. (2.4) and all decay schemes were adapted from [21].

^{137}Cs

Reference point:	382.9 kBq	on 01.01.1970
At the measurement:	320.5 kBq	on 10.10.2018

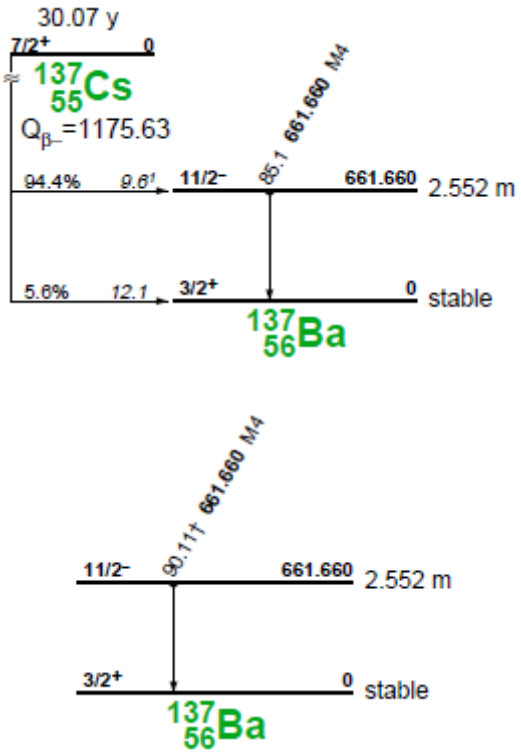

Figure F-1: Decay scheme of ^{137}Cs nuclei.

^{60}Co

Reference point:	401 kBq	on 01.04.2003
At the measurement:	52.239 kBq	on 10.10.2018

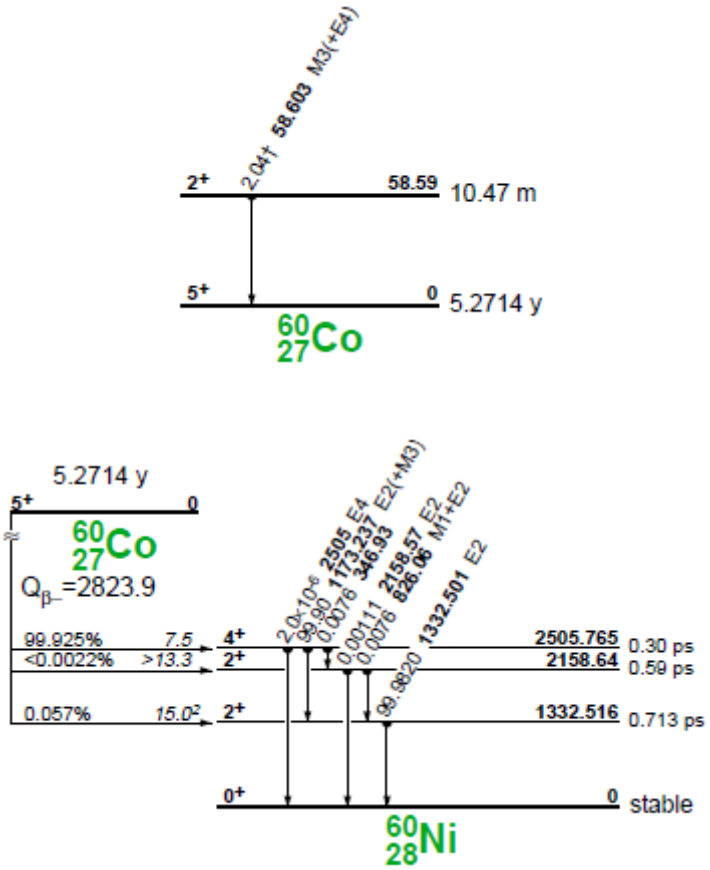

Figure F-2: Decay scheme of ^{60}Co nuclei.

^{207}Bi

Reference point: 397 kBq on 15.12.2008

At the measurement: 320.451 kBq on 21.09.2018

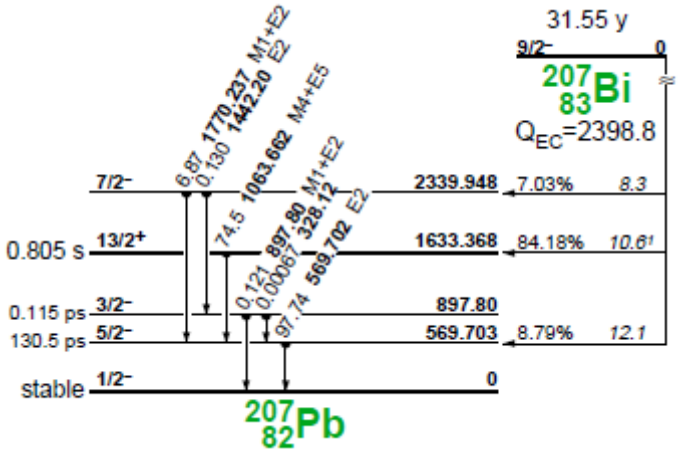

Figure F-3: Decay scheme of ^{207}Bi nuclei.

^{241}Am

Reference point: 5 kBq on 01.03.2003

At the measurement: 4.877 kBq on 21.09.2018

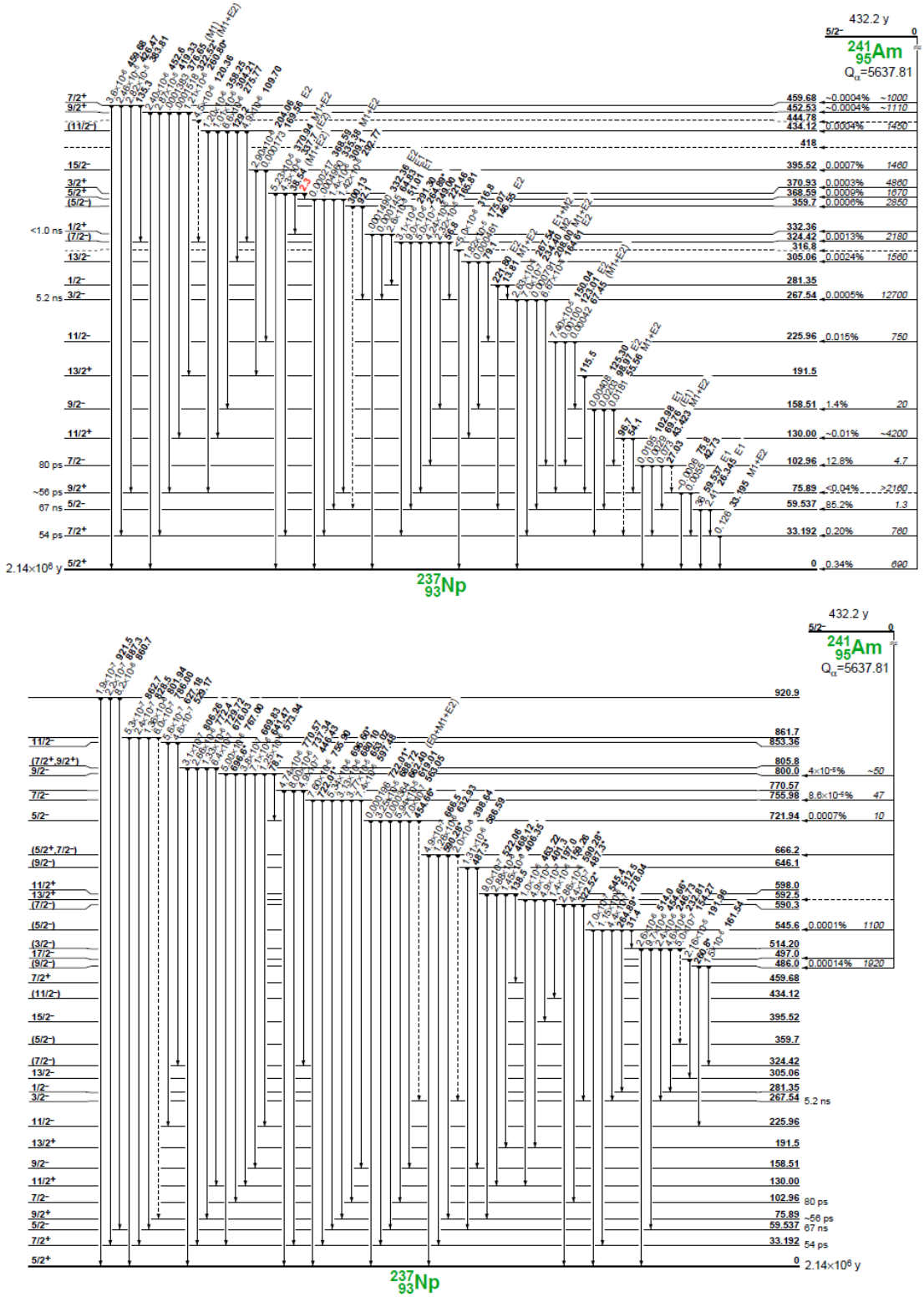

Figure F-4: Decay scheme of ^{241}Am nuclei.

Bibliography

[1] W.R. Leo. *Techniques for Nuclear and Particle Physics Experiments: A How-to Approach.* Springer. ISBN 978-3-642-57920-2 (1987).

[2] Pocket Size Spinthariscope: https://www.instructables.com/id/Pocket-Size-Spinthariscope/ (2019).

[3] Panu Ruotsalainen. *Development of the recoil-beta tagging method and recoil-beta tagging studies of ^{66}As and ^{66}Se*. PhD Dissertation. ISBN:978-951-39-5417-8 (2013).

[4] Juha Uusitalo et al. Mass Analysis Recoil Apparatus, MARA. Acta Physica Polonica B, 50 (3), 319-327. DOI:10.5506/APhysPolB.50.319 (2019).

[5] Juha Uusitalo. Private conversation (2019).

[6] SensL. *How to Evaluate and Compare Silicon Photomultiplier Sensors* (2015).

[7] G. Kawata et al. *Probability Distribution of After Pulsing in Passive-Quenched Single-Photon Avalanche Diodes*. IEEE Xplore Digital Library, DOI: 10.1109/TNS.2017.2717463 (2017).

[8] Glenn F. Knoll. *Radiation Detection and Measurement*. John Wilsey & Sons. ISBN: 0-471-07338-5 (2000).

[9] National Cancer Institute. *Electromagnetic Fields and Cancer*: https://www.cancer.gov/about-cancer/causes-prevention/risk/radiation/electromagnetic-fields-fact-sheet (2019).

[10] R A. Serway et al. *Physics for Scientists and Engineers, Volume 5, Chapters 40-46.* Cengage Learning. ISBN: 1133954006 (2013).

[11] G. Woodside et al. Environmental, Safety, and Health Engineering. John Wilsey & Sons. ISBN: 978-0-471-10932-7 (1997).

[12] Kenneth S. Krane. *Introductory Nuclear Physics*. John Wilsey & Sons. ISBN 0-471 -80553-X (1987).

[13] Kenneth E. Bower et al. Polymers, Phosphors, and Voltaics for Radioisotope Microbatteries. CRC Press. ISBN: 1420041398 (2002).

[14] Paul. A. Tipler et al. *Modern Physics*. W. H. Freeman and Company. ISBN-13: 978-0-7167-7550-8 (2008).

[15] J. S. Lilley. *Nuclear Physics Principles and Applications*. John Wiley & Sons. ISBN: 0 471 97936 8 (2001).

[16] Wikipedia. *Beta decay*: https://en.wikipedia.org/wiki/Beta_decay (2019).

[17] A. K. Mallik. *Stability of Nuclei*. The Himalayan Physics, Vol. II. ISSN: 2542-2545 (2011).

[18] W. Loveland et al. *Modern Nuclear Chemistry*. John Wiley & Sons. ISBN: 9781119328483 (2006).

[19] R. Zanin et al. *Gamma rays detected from Cygnus X-1 with likely jet origin*. Astronomy and Astrophysics Vol. 596. DOI: 10.1051/0004-6361/201628917 (2016).

[20] Sanna Stolze. Spectroscopy and lifetime measurements of $^{166,168}Os$. PhD Dissertation. ISBN: 978-951-39-7208-0 (2017).

[21] Richard B. Firestone. *Table of Isotopes*. Wiley-VCH. ISBN: 0471356336 (1999).

[22] Eljen Technology. *High Temperature Plastic Scintillator*: https://eljentechnology.com/images/products/data_sheets/EJ-244_EJ-248_EJ-244M_EJ-248M.pdf (2016).

[23] F.D. Brooks. *Development of organic scintillators*. Nuclear Instruments and Methods Vol. 162. ISSN: 0029554X (1979).

[24] Kelly D. Rakes. *Evaluating The Response of Polyvinyl toluene Scintillators Used in Portal Detectors*. Biblioscholar. ISBN: 9781288410200 (2012).

[25] L. Verstraete et al. *The visible and ultraviolet absorption of large polycyclic aromatic hydrocarbons*. Astronomy and Astrophysics 266, 513-519 (1992).

[26] J. B. Birks. *The Theory and Practice of Scintillation Counting.* Pergamon Press, ISBN: 9781483156064 (1964).

[27] S. Jarutikorn et al. *Environmentally Friendly Ag+ Detection of "Turn-on" Fluorescent Sensor with a Mega-Stokes Shift and Its Application in Biological Systems.* Oriental Journal of Chemistry. ISSN: 0970-020 X (2019).

[28] Claus Grupen et al. *Particle Detectors.* Cambridge University Press. ISBN: 978-0-511-38866-8 (2008).

[29] L. Torrisi. *Plastic scintillator investigations for relative dosimetry in proton-therapy*. Nuclear Instruments and Methods in Physical Research. DOI: 10.1016/S0168-583X(00)00237-8 (2000).

[30] Christian Joram. *Particle Identification Techniques in High Energy Physics*. EIROforum School on Instrumentation (2011).

[31] R. C. Murty. Effective Atomic Numbers of Heterogeneous Materials. Nature, Vol. 207. DOI: 10.1038/207398a0 (1965).

[32] Particle Data Group. *The Review of Particle Physics*. DOI: 10.1088/1674-1137/40/10/100001 (2016).

[33] Keith E. Holbert. *Charged particle ionization and range*: http://holbert.faculty.asu.edu/eee460/IonizationRange.pdf (2012).

[34] Eljen Technology. *Response of Plastic Scintillators to Atomic Particles*: https://eljentechnology.com/images/technical_library/Response_Curves.pdf (2016).

[35] P. Ganesan et al. *Measurement of Electron Mass using Compton Scattering*. Technical Report. DOI: 10.13140/RG.2.1.2781.9280. (2015).

[36] M. Yamawaki et al. *Study of Reflection and Connection Materials Used for Transmitting and Condensing Scintillation Light by Means of Optical Fiber*. Japanese Journal of Applied Physics. Vol. 47. DOI: 10.1143/JJAP.47.1104 (2008).

[37] SensL. *An Introduction to the Silicon Photomultiplier* (2011).

[38] PhysicsOpenLab. *Silicon Photomultiplier (SiPM)*: http://physicsopenlab.org/2016/02/16/silicon-photomultiplier-sipm/ (2019).

[39] SensL. *C-Series SiPM Sensors*: https://www.onsemi.cn/PowerSolutions/document/MICROC-SERIES-D.PDF (2014).

[40] UDT Sensors, Inc. *Silicon Photodiodes Physics and Technology*: https://www.univie.ac.at/photovoltaik/praktikum/ws2017/silicon_photodiodes.PDF (2017).

[41] Paul A. Tipler et al. *Physics for Scientists and Engineers*. W. H. Freeman. ISBN: 978-1429201247 (2007).

[42] Paul Joseph Barton. *Silicon Photomultiplier for Scintillation Detection Systems.* PhD Dissertation (2011).

[43] Mark Abbott Foster. *Silicon Photomultipliers in Radiation Sensing Applications*. PhD thesis (2010).

[44] H. Moser, *Silicon Photomultipliers, A New Device For Low Light Level Photon Detection*. AIP Conference Proceedings, Vol. 867 (2006).

[45] J. Rosado. *Characterization and modeling of crosstalk and afterpulsing in Hamamatsu silicon photomultipliers.* Journal of Instrumentation. DOI: 10.1088/1748-0221/10/10/P10031 (2015).

[46] James E. Parks. *Attenuation of Radiation*. University of Tennessee. http://www.phys.utk.edu/labs/modphys/AttenuationRadiation.pdf (2001).

[47] Thomas E. Johnson et al. *Health Physics and Radiological Health*. 4th Edition. Lippincott Williams & Wilkins. ISBN 978-1-60913-419-8 (2012).

[48] M. L'Annunziata. *Handbook of Radioactivity Analysis*. Academic Press. ISBN: 9780123848734 (2012).

[49] Richard J. Mathar. *Solid Angle of a Rectangular Plane. Max-Planck Institute of Astronomy*. Heidalberg, Germany (2019).

[50] David J. Dowsett et al. *The Physics of Diagnostic Imaging*. 2nd edition. Hodder Arnold. ISBN: 978 0 340 80891 7 (2006).

[51] Jan Sarén. Private communication (2019).

[52] Panu Ruotsalainen. Private communication (2019).

[53] J. Kantele. *Handbook of Nuclear Spectrometry.* Academic Press. ISBN: 0123964407 (1995).

[54] National Nuclear Data Center. NuDat 2.7: https://www.nndc.bnl.gov/nudat2/ (2019).

[55] Ronald G. Driggers. *Encyclopedia of Optical Engineering*. CRC Press. ISBN: 0824742516 (2003).

[56] M. V. Nemallapudi et. al. *SiPM Angular Response and Enhanced Light Extraction.* IEEE. DOI: 10.1109/NSSMIC.2013.6829586 (2014).

[57] A N. Otte et. al. *Characterization of Three High Efficiency and Blue Sensitive Silicon Photomultipliers*. Nuclear Instruments and Methods in Physics Research, Vol. 846. DOI: 10.1016/j.nima.2016.09.053 (2017).

[58] HM. Park et. al. *Evaluation of the Photon Transmission Efficiency of Light Guides Used in Scintillation Detectors Using LightTools Code*. Journal of Radiation Protection and Research. DOI: 10.14407/jrpr.2016.41.3.282 (2016).

[59] M. Mikeli et. al. *Collimator Study of a γ-Camera System using GATE*. IEEE. DOI: 10.1109/NSSMIC.2009.5401940 (2009).

[60] Fiber Optical Networking. *Getting to Know Fiber Collimator.* http://www.fiber-optical-networking.com/getting-know-fiber-collimator.html (2016).

[61] S. K. Lee et al. *Comparison of New Simple Methods in Fabricating ZnS(Ag) Scintillators for Detecting Alpha Particles*, Progress in NUCLEAR SCIENCE and TECHNOLOGY, Vol. 1. DOI:10.15669/pnst.1.194 (2011).

[62] Henrik Heräjärvi. *Variation of Basic Density and Brinell Hardness Within Mature Finnish Betula Pendula and B. Pubescens Stems.* Wood and Fiber Science, Vol.36 (2004).